Quantitative *In Vitro* Characterization of Membrane Permeability for Electroporated Mammalian Cells

Daniel C. Sweeney

Dissertation submitted to the Faculty of the
Virginia Polytechnic Institute and State University
in partial fulfillment of the requirements for the degree of

Doctor of Philosophy
in
Biomedical Engineering

Rafael V. Davalos, Chair
Daniela Cimini, Co-Chair
Scott Verbridge
Steven Poelzing
Ahmad Safaai-Jazi

March 14, 2018
Blacksburg, Virginia

Keywords: bioelectrics, electroporation, biotransport, quantitative microscopy, membrane permeability, pulsed electric fields

Quantitative *In Vitro* Characterization of Membrane Permeability for Electroporated Mammalian Cells

Daniel C. Sweeney

(ABSTRACT)

Electroporation-based treatments are motivated by the response of biological membranes to high-intensity pulsed electric fields. These fields rearrange the membrane structure to enhance the membrane's diffusive permeability, or the degree to which a membrane allows molecules to diffuse through it, is impacted by the structure, composition, and environment in which the cell resides. Tracer molecules have been developed that are unable to pass through intact cell membranes yet enter permeabilized cells. This dissertation investigates the hypothesis that the flow of such molecules may be used to quantify the effects of the electrical stimulus and environmental conditions leading to membrane electroporation. Specifically, a series of electrical pulses that alternates between positive and negative pulses permeabilizes cells more symmetrically than a longer pulse with the same total on-time. However, the magnitude of this symmetric entry decreases for the shorter alternating pulses. Furthermore, a method for quantitatively measuring the permeability of the cell membrane was proposed and validated. From data near the electroporation threshold, the response of cells varies widely in the manner in which cells become permeabilized. This method is applied to study the transient cell membrane permeability induced by electroporation and is used to demonstrate that the cell membrane remains permeable beyond 30 min following treatment. To analyze these experimental findings in the context of physical mechanisms, computational models of molecular uptake were developed to simulate electroporation. The results of these simulations indicate that the cell's local environment during electroporation facilitates the degree of molecular uptake. We use these models to predict how manipulating both the environment of cells during electroporation affects the induced membrane permeability. These experimental and computational results provide evidence that supports the hypothesis of this dissertation and provide a foundation for future investigation and simulation of membrane electroporation.

Quantitative *In Vitro* Characterization of Membrane Permeability for Electroporated Mammalian Cells

Daniel C. Sweeney

(GENERAL AUDIENCE ABSTRACT)

Electroporation is a biophysical process in which intense electric fields permeabilize bilayer membranes. The degree to which a membrane allows molecules to diffuse through it is called its diffusive permeability, and is impacted by the structure, composition, and environment in which the cell resides. This dissertation investigates the hypothesis that the flow of molecules into cells through their membranes may be used to quantitatively study the effects of the electrical stimulus and environmental conditions leading to membrane disruption. Here, I demonstrate that the cellular response to pulsed electric fields is affected by the waveform of the applied electrical stimulus. Specifically, a series of electrical pulses that alternates between positive and negative pulses permeabilizes cells more symmetrically than a longer pulse with the same total energized time. However, the total molecular uptake decreases for the shorter alternating pulses over the longer pulse. A method for quantitatively measuring the permeability of the cell membrane using a fluorescent tracer molecule is also developed and validated. This method is applied to show how cell membrane permeability changes following electroporation. To analyze these findings, computational models of molecular flow through the cell membrane are developed. These simulations indicate that the cell's surrounding environment during electroporation dramatically impacts the degree of molecular uptake. We use these models to predict how manipulating both the environment of cells during electroporation affects the induced membrane permeability. These experimental and computational results provide a foundation for future investigation and simulation of membrane electroporation.

To my family: Mom, Dad, Connor, Dennis, and Sam.

Thank you for you encouraging me to ask "why?".

Acknowledgments

I would like to thank my advisor, Dr. Rafael Davalos for supporting me and my work over the past five years; your patience with my frustrations and belief in empowering me to make my work my own serve as invaluable life lessons that helped me through my graduate career. I would also like to thank my co-advisor, Dr. Daniela Cimini for always being willing to share with me her insight into and microbiology. I am inspired by your enthusiasm for new ideas and insistence on effective communication, which serve as examples of what to strive for in my career and in life. I am grateful to Dr. Damijan Miklavčič for his mentorship and for the welcoming me as a visiting scholar in your group. You, Janja, Tadeja, Matej, Matej, Lea, Lea, Duša, Bor, and all the other members of the Laboratory of Biocyberntics made my time in Ljubljana second to none and provided me a strong foundation from which I'm building my career. I look forward continuing our professional collaborations and friendships. I especially like to thank John Caldwell for his mentorship and investing in my success both as a member of Team Glucose and as an engineer. Thank you for your advice on going graduate school at Virginia Tech and for helping me develop my passion for bioelectricity and abilities in hardware design.

To my labmates, colleagues, and friends that have made my time in Blacksburg not seem so long: Jack, Joel, Megan, Melissa, Chelsea, Rebekah, Sophie, Elisa, Temple, Suyashree, Nico, and many others. Your friendship and camaraderie have been invaluable to my work during the week and my sanity on the weekends—I can't thank you all enough. To Nick and Brennan for their constant encouragement to be my best and for teaching how non-conformity is an asset. I want to especially thank Dr. Samantha Erwin for empowering me to be ask lofty questions during our late nights at

coffee shops and for her unfailing support in my successes and failures. You're the best partner I could ask for and I can't wait to see where our future takes us as a family.

Finally, I would like to thank my family for their unfailing encouragement and support since before I can remember. Thanks to my parents, Tim and Lorena Sweeney; I know I said I didn't want to do anything electrical when I grew up, but here we are. Thanks also to Connor and Dennis for being ever-willing to remind me that enjoying life outside lab is both real and valuable. Thank you all for helping get to where I am today.

Contents

List of Tables

List of Figures

Chapter 1

Introduction

1.1 Electromagnetics in Biology and Medicine

Conventionally, four fundamental forces motivate the physical interactions of matter: gravitational forces, electromagnetic forces, and strong and weak nuclear forces. Of these, the electromagnetic forces that act on and between charged particles are particularly strong: similarly charged molecules repel each other while oppositely charged molecules are attracted. In biology, electromagnetic forces are ubiquitous and play vital roles in phenomena such as hydrogen bonding, oxidation-reduction reactions, the propagation of action potentials, pH-facilitated diffusion, cell division, and mitochondrial energy conversion. Relatively recently, advances in biomedical technology have made it possible to artificially control the distribution and flow of charge within biological matter. For example, magnetic resonance imaging (MRI) technology—also known as nuclear magnetic resonance (NMR)—utilizes a magnetic field to excite electrons in water molecules within a specimen to provide spatial contrast for imaging [1]. Magnetic fields have also been proposed as non-invasive ablation modalities because they induce an electric field within nearby material [2, 3, 4].

Electric fields have a longer biomedical pedigree than their magnetic counterparts as they are easier

and more intuitive to manipulate. Pacemakers—devices inserted into the body to regularize cardiac rhythms—apply an electric potential to excitable cells that initiates the electrical signaling cascade within the heart to facilitate proper contraction [5]. Other devices have been developed to stimulate regions of the brain with the goal of normalizing or mitigating seizures in epileptic patients [6, 7] and to assist in the restoration of neural function following injury [8]. Beyond the threshold for stimulation, electric fields can be applied at strengths and for durations that manipulate the physical structure of bilayer membranes. Laboratory and clinical techniques that utilize this phenomenon, collectively referred to as electroporation-based treatments and therapies, comprise a hotbed of industrial and academic research.

Much of cellular physiology is structured to exploit electromagnetic gradients for energy conversion, including thin, dielectric membranes that electrically isolate distributions of charge. For example, a mitochondrion contains the molecular machinery to generate the proton gradients responsible for much of the conversion of energy into a form a cell is able to use [9]. By establishing this chemical gradient, the mitochondrion simultaneously establishes an electric field across its membrane on the order of 1 to 10 MV/m [10, 11], which is similar in magnitude to the electric fields used to disrupt extracellular membranes (0.1 to 100 MV/m).

1.2 Applications of Electroporation Technology

From a biophysical perspective, electroporation is the process by which an intense electric field motivates conformational changes in the molecular structure of cell membranes. Normally-occurring nano-scale defects in the cell membrane expand into metastable structures that allow molecules to pass from one side to the other more readily [12, 13, 14, 15]. In this chapter, I provide an overview of the electroporation as a physical process, the implications of pore creation for diffusive transport of molecules across the cell membrane, a timeline of events in the electroporation process, and a discussion of post-electroporation events.

Electroporation technologies all rely on the application of pulse electric fields (PEFs) to drive the breakdown and rearrangement of the components of a cell's membrane. These technologies may be broadly classified as treatments that seek to destroy cells directly or treatments that are designed to maintain cellular viability but permeabilize the cell membrane. Irreversible electroporation (IRE) irreparably damages cells to induce maximal cell death for clinical ablation procedures. The later class of treatments includes treatments such as gene electrotransfer (GET) and electrochemotherapy (ECT) which rely on an applied electric field to render a cell membrane better able to uptake DNA or normally-excluded drug molecules. While the fundamental mechanisms driving electroporation technologies are similar, the each class of treatments is optimized for a specific use case.

Electroporation-mediated ablation induces cell death with minimal thermal damage and irrecoverably destabilizes the constituent cells within a tissue [16]. IRE has been used to treat tumors in the brain [17, 18, 19, 20], skin [21], liver [22, 23], kidney [24], and pancreas [25, 26]. IRE has shown clinical promise because it destroys the cells within the target tissue, while leaving the stromal components largely intact [27, 28]. IRE is being deployed in the clinical environment to treat previously untreatable tumors located near critical vasculature, such as the superior mesenteric artery in the pancreas [25, 29]. Recently, calcium ions have been used as adjuvants in cells electroporated *in vitro* [30, 31] and injected into tumors *in vivo* prior to treatment [32]. Tumors treated in this manner exhibit significantly enhanced cell death compared to conventional IRE alone [21]. The present hypothesis for the mechanism that drives this enhanced lethality is that cells treated in a calcium-rich buffer exhaust their ability to reestablish the calcium gradient across the cell membrane and eventually the cells die in a process termed *accidental necrosis* [33].

GET is a process facilitated by an electroporation-enhanced cell membrane permeability by which plasmids are introduced into cells. GET was one of the first applications of electroporation technology [34] and has since been used for therapeutic applications [35, 36, 37, 38, 39, 40] and for bench-top research [41]. GET is a common non-viral technique that greatly enhances the efficiency by which cells are transfected with a particular piece of genetic information [42, 43].

ECT also exploits electroporation-enhanced membrane permeability to deliver drugs locally to a tumor. One of the challenges in conventional chemotherapy is that the drugs used in these clinical procedures, such as bleomycin, are largely unable to cross cell membranes, yet entry into the cell is a requirement for their therapeutic efficacy. Electroporation technology allows such drugs to be injected into the tumor prior to treatment so that when the cells become permeabilized, the chemotherapeutics can efficiently enter the cells localized to the treatment region [44, 45, 46, 47]. Termed electrochemotherapy (ECT), this process has been successfully implemented in Europe at the time of writing and is popular because the systemic side-effects associated with chemotherapeutics are mitigated due to the localized treatment [48].

1.3 Physiological Mechanisms of Electroporation

The physiological responses of cells to the sudden onset of an enhanced membrane permeability state are complex and coupled through physical, chemical, and electrical means. Each individual cell has a unique membrane composition and morphology and therefore responds differently to applied electric fields. Though these complexities impose obstacles to directly quantifying the precise cellular response to different treatments, several trends are predictable following electroporation treatment.

Cell morphology, or the physical shape of a cell, can greatly impact the manner in which it is electroporated. Beyond the idealized spherical cell, it has been shown that prolate and oblate spheroidal cells exhibit a larger transmembrane potential at their anodic and cathodic poles if their major axes are oriented parallel with the electric field vector than for a spherical cell of the same volume [49, 50]. Furthermore, when positioned perpendicular with the electric field, these same cells experience a decreased transmembrane potential. Ultimately, a larger transmembrane potential indicates a greater propensity for electroporation, all else being equal. Additionally, realistic cell morphologies typically have protrusions from the main cell body, especially in three-dimensional culture [51, 52]. Depending on how these protrusions are oriented, the electric field

parameters required to cause electroporation may change [53].

The phospholipids constituting cell membranes are themselves comprised of a hydrophobic head groups with long hydrocarbon tails. These tails can be modified with functional groups that alter their shape and result in a change in the spacing between adjacent lipids. For example, acyl chains and methyl branched chains on lipids with ether and ester linkages affect the electric field threshold required to permeabilize the cell membrane [54]. The presence of cholesterol has been shown to increase the electroporation threshold from 325 mV/nm for 0% cholesterol to 750 mV/nm for 40% [55]. Depending on the molecular network and the applied electric field, groups of lipids may form and move together along the cell membrane. These rafts move together around the cell membrane and locally change the manner and degree to which the cell membrane responds to an electric field [56, 57].

When a cell becomes electroporated, the process of electroporation begins with the application of an electric field on the order of 0.1 to 1.0 MV/m [58, 59]. The electric field enhances the resting transmembrane potential (TMP) of the cell (-65 to -70 mV [60]) in a manner that depends on the cell radius [61, 62, 63, 64, 65]. The electric field at the aqueous-membrane interfaces orients the local water molecules into energetically stable long dipole chains within 1 to 10 ns [14, 66, 67, 68]. Once the TMP surpasses a threshold of 0.25 to 1.0 V, these water dipoles—or *water wires*—penetrate the cell membrane [14, 69]. This hydrophobic pore allows minimal molecular transport across the membrane, though the potential for a molecule to pass through its structure increases over the following 10 ns as additional water molecules aggregate around the original water wire [14, 68].

A hydrophilic water wire in the hydrophobic membrane interior is energetically unstable and, as more water molecules aggregate around the water wire, lipid head groups migrate into the pore structure to stabilize it [70, 71]. Hydrophilic pores are a metastable energetic state in the process of pore formation at which the steric hinderance and line tension of the pore balance the change in electrical energy and the surface tension [72, 73, 74]. It is through these hydrophilic pores,

initially created with a radius of 0.5 to 1.0 nm [72, 75], that the inner and outer membrane leaflets are continuous [76, 77, 78]. Molecular transport is significantly enhanced by the presence of pores [79, 80, 81] and the membrane begins to shunt ionic and electrical current, largely inhibiting further pore creation [13, 82].

Transport of chemical species across an electroporated cell membrane is governed by electro-diffusive forces. In addition to simple diffusion along a concentration gradient, charged molecules, such calcium ions or propidium ions (Pro), are motivated by Coulombic forces during the application of an electric field [80, 83, 84]. An intact membrane largely inhibits the flow of molecules, or tightly facilitates their passage through specific biochemical mechanisms. However, an electroporated membrane loses the capacity to inhibit molecular flux. A membrane's diffusive permeability is the quantity that describes its capacity of the membrane to allow molecules to pass through it. Membrane permeability is mathematically expressed as a multiplier for the typical diffusion coefficient of a molecule in aqueous medium. Though the cell membrane's diffusive permeability following electroporation has been qualitatively investigated *in vitro* [85, 86, 87, 88, 89, 90], quantitative measurements of the evolution of its permeability over time have not been estimated, though extensive qualitative data have been reported. For example, it was noticed that different molecular weight sugars would pass through the cell membrane differently following electroporation [91]. Additionally, estimates of the cellular uptake rates of fluorescent tracer molecules have been made using molecules such as Pro [65, 90, 92, 93, 94], YO-PRO-1 and its derivatives [90, 93, 95], ethidium homodimer [96, 97], 7-AAD [98], calcein [58, 97], and others [90, 99, 100]. Most of these molecules are used as viability markers for cells because they are excluded from intact membranes, but will enter a cell and become noticeably fluorescent when they pass through a damaged membrane and bind to intracellular structures. Upon entering the cell, many of these exclusion dyes have diffusion coefficients approximately 3-fold lower than they do in the extracellular buffer and readily diffuse throughout the intracellular space [101]. Caution should be exercised when interpreting the results of electroporation experiments involving these molecules, as their uptake does not assay cell death, but only membrane integrity to molecules with similar

physical properties to the molecular tracers used to make the measurements [90].

Pores are metastable structures according to molecular dynamics simulations of electroporation [14], indirect visualization of pore structures [102] and continuum-level modeling. Indirect evidence through fluorescent tracer molecule uptake measurements confirms that there exists a finite period of time following removal of the applied electric field in which membranes remain permeable, though they may eventually reseal [85, 90, 91, 102, 103, 104]. Molecular dynamics (MD) simulations of the atomistic interactions in pore formation estimate that pore resealing of hydrophilic pores occurs on the order of 1 to 20 seconds [14, 105] following treatment and begins with the dissociation of the headgroup-headgroup interactions in core of the membrane pores [14, 98]. The water wires bridging the cell membrane through hydrophilic pores are estimated to have a stable lifetime of 10 ns to $>$100 ms [106, 107] and the process of pore collapse, once begun, occurs on the order of 20 ns [108]. Large pores with diameters $>$1.5 nm are relatively rare in these simulations, suggesting that increased permeability observed between two electroporation treatments of different pulse durations and similar electric field strengths is due to an increase in pore number rather than pore radius. While MD simulations are useful for investigating the possible mechanisms underlying electroporation, they are largely considered to predict much faster pore formation and collapse rates than are observed experimentally or with continuum-level modeling. Further MD simulations are sufficiently computationally intensive that it is infeasible to perform simulations on timescales longer than a few microseconds [105].

In continuum-level models of electroporation, a cell membrane is typically considered a thin lossy dielectric with a finite characteristic thickness (approximately 5 nm) that is significantly smaller than the cell radius [109]. While much of the atomistic resolution is lost in continuum-level models, the fundamental perspective of the model shifts from a water dipole initiating pore formation to the heuristic perspective of a voltage threshold beyond which electroporation occurs [13, 82]. Once a pore is formed, it can fluctuate along a radial parameter space, depending on the induced TMP [13, 73, 74]. Continuum-level models estimate that pore resealing occurs on the order of seconds to minutes [82, 110, 111] following electroporation and, consequently, the induced permeability of

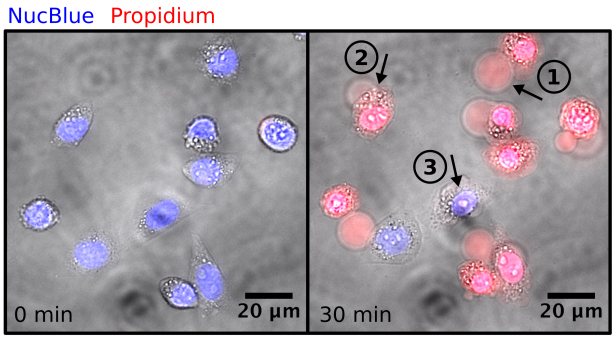

Figure 1.1: Dramatic in morphological changes occur in CHO-K1 cells following electroporation in a microdevice. Images of cells are shown prior to electroporation (0 min) and 30 min following treatment with a 320 kV/m electric field applied for 100 μs as a square pulse. Following electroporation, blebbing (1), swelling of the cell body (2), and nuclear condensation (3) occur.

the cell membrane persists on a similar timescale [80]. Such models are discussed in further detail in later chapters.

Attempts have been made to indirectly visualize of pore dynamics using high-resolution microscopy techniques. Rapid-freeze techniques have been used to preserve pores for microscopic examination [102, 112]. Experiments in erythrocyte ghosts show that that pores can exist for several seconds and all fluorescence would be lost in 1 to 2 min following treatment [113]. Further, with two fluorescent tracer molecules of different sizes, it was confirmed that initial large pores collapse into smaller stable pores following electroporation [90]. Pores can remain open for hundreds of seconds following treatment, and increase in number and size with increasing transmembrane potential [104]. The pore lifetime was demonstrated to not depend on the applied potential, suggesting that the bulk population of pores exhibits similar relaxation times, regardless of how it was generated.

Due to the osmotic gradient between the cellular interior and exterior, opening pores within the membrane is concomitant with cellular swelling due to an inrush of water molecules down the osmotic gradient (Fig. 1.1). If the osmotic pressure forces the cell membrane to expand beyond its capacity, the cell membrane will rupture in a process called osmolysis [114, 115]. Cells have been observed to increase in volume by $>$55% over their untreated volume in the minutes following electroporation, though these results appear to be at least partially inhibited by the addition of sucrose and polyethylene glycol (PEG) with molecular weights between 200 and 1000 g/mol [116]. In such buffers, cells have been observed to swell to a radius about 5% larger than their pre-

treatment radius [94].

Related to swelling, cellular blebbing is a phenomenon observed following electroporation that involves the irregular bulging of the cell membrane. One possible mechanism motivating post-electroporation bleb formation is the disruption of cortical actin structures by the influx of water following membrane damage [117], though additional investigation is required to elucidate the precise mechanisms driving this phenomenon. Blebs typically have a 20 s or longer delay between the removal of an applied electric field treatment and its onset at the anodic and cathodic membrane poles [118] (Fig. 1.1). The directional extension of such blebs showed that elongated pseudopod-like blebs extend exclusively in the anodic direction [119], but were increasingly inhibited by increasing the extracellular sucrose concentration. Bleb growth stabilizes following initial formation and is concomitant with a large membrane permeability increase 30 to 60 min following electroporation [120].

When a cell is electroporated, membrane components that are normally only present on one leaflet are able to travel to the other leaflet. For example, phosphatidylserine is exclusively found on the inner leaflet of the cell membrane, under normal physiological circumstances. However, when a pore forms, phosphatidylserine is able to diffuse across to the outer membrane leaflet on a continuous membrane surface through the pore interior [121, 122]. Interestingly, it has been shown that electroporated cells exhibit blebbing and phosphatidylserine externalization following electroporation treatments and, when co-cultured with mouse macrophages, become the target of macrophage phagocytosis at frequencies 10 to 15 times greater than the non-electroporated cells [123]. Other work has shown that intracellular calcium mobilization, phosphatidylserine externalization, and caspase activation can occur at electric field strength-duration thresholds lower than required to allow transport of larger reporter molecules [96, 121]. These results suggest that electroporated cells exhibit an apoptosis-like response that could be recognized as cell death by other cells.

Although the cellular membrane is considered the primary structure affected by PEFs, organelles on the cell interior do not appear to escape the effects of direct electroporation. In particular, sub-

cellular effects of electroporation (and the mechanistically-similar magnetoporation) have become a topic of interest for the application of computational models [64, 64, 109, 124, 125, 126]. Though little experimental evidence is currently available to corroborate these predictions directly, it is hypothesized that, as the frequency of the applied electrical pulses increases, the cell membrane conducts more of the high-frequency components of the applied field, which subsequently allows membrane-bound organelles to also be exposed these fields. Computational models consistently predict that a TMP can plausibly be developed on dielectric membranes inside the cell. Electrical pulses, tens of nanoseconds in length, have been shown to mobilize intracellular calcium and activate caspase signaling within a cell [96, 121, 123, 127], but as of yet, little direct evidence of intracellular electroporation is available.

The pathways by which electroporated cells die following treatment are complex and reports are conflicting. For example, there appears to be a region in the strength-duration parameter space where caspase-dependent cell death is induced. However, cell death has also been shown to be caspase-independent in other regions [127]. A combination of hypothermia and electroporation was shown to induce caspase 3/7 activation and resulted in $>$60% PARP cleavage following a 4.5 hour post-treatment incubation [128]. The introduction of calcium ions into the extracellular buffer has also been investigated as an effective means of inducing cell death [30, 31, 32, 120], but little evidence on the cell death model is yet available. Together, these data indicate that apoptotic pathways may contribute to cell death resulting from electroporation, though there is significant work to be done in this area.

In addition to pore formation, a cell may also deform in response to an applied electric field, When a polarizable body, such as a cell, is exposed to an electric field, it experiences an electric force that is spatially distributed proportional to the charge density. As the transmembrane potential builds across the cell membrane, ionic charge densities build on either side and create local Coulombic forces that mechanically deform the cell membrane [129]. Electrical deformation of an intact cell membrane has been studied from a computational perspective and data indicate that a cell elongates along the electric field vector in a manner that depends on the ratio of the internal and

external buffer conductivities [130, 131]. The greatest electrotension was observed at the extreme anodic and cathodic poles compared to a cell's equator; however, the cell was predicted to pass through a transition state prior to equilibration in which concavities are present in the membrane. However, in these numerical experiments, the effects of electroporation and the maximum in TMP possible before the onset of electroporation were ignored.

1.4 Motivating Hypothesis and Outline

Clinical treatments based on electroporation have generally been successful. While the specific mechanisms motivating these therapies are not yet well-understood, experimental observations indicate that a well-defined strength-duration threshold exists for applied electric fields beyond which electroporation occurs. Existing computational models of electroporation agree with and recapitulate the strength-duration threshold and molecular uptake, but have largely been left unvalidated due to a lack of quantitative data. These models predict the generation and expansion of membrane pores and the associated membrane transport by incorporating electrostatics, reaction-diffusion style schemes for pore formation, and drift-diffusion for molecular transport. Though complex, present computational models of cellular electroporation remain largely unvalidated, yet sufficiently too complex to be useful for designing practical electroporation protocols through consideration of the underlying biophysical mechanisms.

Attempting to bridge this computational-experimental gap, experimentalists have developed techniques involving fluorescence microscopy, flow cytometry, and impedance measurements to empirically elucidate the mechanisms underlying electroporation. Propidium ions, YO-PRO-1, trypan blue, calcein, and other tracer molecules have been used to observe the molecular flux into and accumulation inside of the cell. Understanding and characterizing the membrane permeability of cells following PEF treatment in meaningful ways requires the development of a robust connection between experimental and computational results. The work presented in this dissertation addresses this connection under by the hypothesis that *measurements of membrane permeability*

in PEF-treated cells using fluorescence microscopy can be used to validate computational models of electroporation-mediated mass transport. Towards this end, this dissertation describes methods for measuring membrane permeability *in vitro* using propidium ions. These data are used in two computational models of diffusive permeability in the cell membrane: to fit a dynamical system model and to validate a finite element model using spatiotemporal membrane permeability data. Together with experimental data, these models provide a heuristic platform to design and optimize PEF treatment schemes for IRE, GET, and ECT applications.

In this dissertation, I present experimental and computational results to characterize the electroporation-mediated diffusive permeability response in cells exposed to PEFs. Following a brief introduction into the physical mechanisms belying electroporation (Chapters 2) a method to quantitatively measure membrane permeability is developed (Chapters 3-4). These data are incorporated into computational models (Chapters 5-6) to provide a mechanistic basis for studying electroporation. Finally, a concluding chapter (Chapter 7) will summarize the results of this work and how the hypothesis is answered. Brief descriptions of each chapter are as follows.

Chapter 2 presents a review of the current understanding of the relevant biophysics governing single-cell electroporation that drives the success of tissue-level treatments. Electric fields are discussed within the context of cell biology and resultant phenomena are discussed, including electric field propagation in biological media, drift-diffusion, and pore formation.

Chapter 3 presents methods to quantitatively characterize cellular responses to electroporation, including an analysis of molecular flow into the cell following electroporation with clinically relevant treatment schemes. The spatial dependence of this molecular flow is shown to differ depending on the duration of and the delay between consecutive electrical pulses. These data indicate that cells exposed to high-frequency bipolar electrical pulses become permeabilized at a greater voltage threshold but do so more symmetrically between the anode-facing and cathode-facing poles of the cell membrane, than for cells exposed to trains of longer monopolar with equivalent energized times. Finally, a quantitative method for measuring net membrane permeability from a time series

microscope images is presented.

Chapter 4 characterizes cellular uptake responses to pulsed electric fields using an application of the method developed in Chapter 3. This method is extended to single-pulse treatments to examine more fundamental biophysical behaviors obfuscated by long pulse trains. The cellular response to electrical pulses with pulse duration of 1, 10, 100, and 1000 μs and strengths from 170 to 400 kV/m are presented. The normalized diffusive permeability is shown to reach 1.3×10^{-8} m/s in the minutes following treatment. The cellular response to these treatments varied in response time and uptake rate on the individual cell scale. These responses were defined and demonstrate that a subpopulation of cells exhibits a delayed permeabilization compared to the general population. Finally, these data indicate that this delayed permeabilization occurs in a transition region near the strength-duration threshold for electroporation, but ultimately disappears at much larger strengths and durations.

Chapter 5 proposes a computational scheme based on ordinary differential equations to model cellular electroporation. Rather than focusing on the transport across a differential portion of the cell membrane, a stage model is developed using a dynamical system to consider molecular transport across the cell membrane in aggregate. A stage model of this kind is much more readily validated using experimental measurements as it more closely corresponds to data commonly obtained from *in vitro* experiments. The model is shown to be asymptotically stable following the removal of the applied electric field and indicates that buffer composition plays a critical role in electroporation-mediated membrane porosity. It also predicts a limited impact of inter-pulse delay on membrane permeability and that the per-pulse permeability increase is proportional to the square root of the pulse number. These results demonstrate the model's flexibility and its capacity to readily incorporate new experimental data.

Chapter 6 describes an extension of present models of electroporation that is implemented to computationally study propidium uptake dynamics. This model of electroporation-mediated membrane permeability is implemented using a DG finite element method to solve a drift-diffusion system for

a small charged ion around an idealized cell. It is in good agreement with experimental and computational data immediately following the application of an electrical pulse and is easily modified for flexibility in future studies.

Chapter 7 concludes this work with a summary of our present conclusions and a discussion of potential extensions of the methods and results described herein. Several key areas for technological advancement of electroporation-mediated diffusive permeability are identified and the present work is discussed within this context.

Chapter 2

Theoretical Principles of *In Vitro* Electroporation

2.1 Introduction

Within a tissue, the local electric field strength is hypothesized to be related to the ablation field and, if modeled appropriately, can provide invaluable information to a medical operator towards the visualization of the expected final lesion volume. The electric fields used in electroporation technologies permeabilize cell membranes and allow molecules to flow between the intracellular and extracellular compartments, which disrupts cellular homeostasis. In this chapter, I review the relevant background for studying electroporation-mediated membrane permeability. I begin with a brief discussion of the electrical waveforms and parameter space typical of electroporation schemes and a review of the tracer molecules typically used to study electroporation *in vitro*. I end with a discussion of the biophysical principles that have driven the advancement of this technique, including Maxwell's equations, and the solutions, assumptions, and considerations critical to computational models of single-cell electroporation.

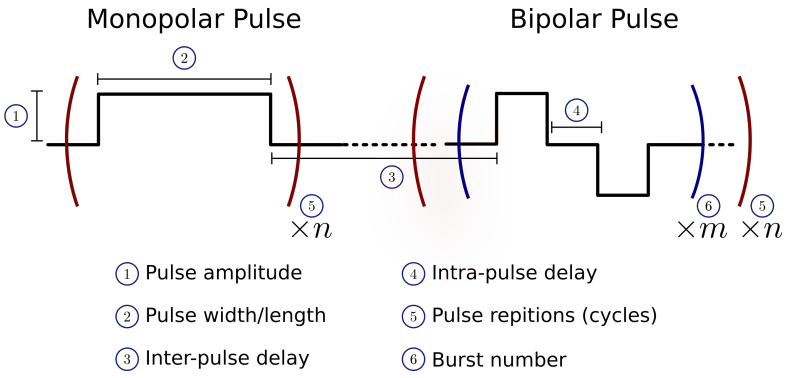

Figure 2.1: Anatomy of bipolar and monopolar square electrical pulses. Waveforms commonly used in IRE are shown schematically to indicate terminology. A train of n monopolar pulses are shown followed by a train of n bipolar pulses in bursts of m pulses.

2.2 Pulse Parameter Space

The parameter defining the electrical pulses used for electroporation treatments is largely a combination of four variables: the pulse width of the applied signal, its polarity (monopolar or bipolar) and amplitude, and the number of times a pulse or set of pulses is applied to a tissue (Fig. 2.1). Perhaps the most obvious parameter impacting the electroporation treatment is the amplitude of the applied pulse. Typically, this amplitude is applied as an electric potential between two or a number of electrodes. However, it is the electric field intensity in the vicinity of the cell that acts to raise the TMP of the cell membrane [61, 62]. Generally speaking, the required amplitude to elicit electroporation is inversely proportional to pulse duration. Together with the pulse width and number of pulses, the pulse amplitude plays a role in the Joule heating that occurs in during treatment [132].

The duration of the applied electric field is correlated to the degree to which a cell becomes permeabilized. Typically, electrical pulses are subdivided into three lengths: millisecond, microsecond, and nanosecond. Millisecond electrical pulses are typically utilized to not only permeabilize a cell, but to electrophoretically drive charged molecules through the cell membrane following initial permeabilization. Gene electrotransfer (GET) uses pulse durations of 1 ms to enhance the efficiency with which genetic information passes through the cell membrane [133]. Microsecond electrical pulses are frequently used to permeabilize cells and rely on the simple diffusion to of drug molecules [80, 81, 134] into the cell during electrochemotherapy (ECT) or to directly and irrecov-

erably damage the cell in IRE procedures [16]. Microsecond pulses are conventionally delivered as a train of 100 μs pulses applied at 1 Hz. Nanosecond pulses—also referred to as nanosecond pulsed electric fields (nsPEFs)—have been utilized with pulse durations from 10 to 600 ns and are hypothesized to penetrate deeper into the cell beyond what is possible with longer pulse durations. nsPEFs have been shown to induce apoptosis-like cell death [96, 123] and result in a phenomenon termed supraelectroporation in which the nanoscale defects form throughout the cell membrane, rather than larger pore structures forming at at the cell poles [135, 136, 137].

The polarity of the electrical pulses applied to a cell are especially important when two pulses are delivered in rapid succession. For example, when a pulse is delivered, the cell membrane has a both a conductive response and a dielectric response and takes time for the TMP to reach a steady state transmembrane potential. Similarly, after the cessation of an applied electric field, it takes time for the the induced TMP to fall to its resting potential. However, if an opposite-polarity pulse is delivered rather than simply removing the applied pulse, the cell membrane discharges more rapidly [138, 139]. This assisted discharge mechanism has been hypothesized to be a contributing mechanism underlying the experimental observation that 1 μs pulses delivered in rapid succession have a higher electroporation threshold [94]. Similar to the assisted discharge mechanism, if the induced TMP is not allowed to reach a steady state prior to the cessation of the applied pulse, the TMP will not be able to reach its maximum, as it would for longer pulses, and will instead settle to an oscillating sawtooth waveform [94]. Conventionally, these bipolar pulses would be delivered in an alternating symmetric or antisymmetric manner, though recently a technique utilizing asymmetric bipolar pulses has also been shown to be effective for cellular ablation [139].

Viewing an aggregate of cells or a tissue in terms of a passive dielectric-conductive model involves an ensemble of cells with thin dielectric membranes surrounding and immersed in a conductive medium. It has been shown that high-freqency bipolar pulses are better able to generate a uniform electric field in such a medium, resulting in a more homogenous ablation [109]. Scaling this phenomenon to tissues, high-frequency bipolar pulses mitigate impedance differences between adjacent conductive and dielectric mediums by applying the electric field pulses at a frequency at

which the difference in the dielectric and conductive contributions of each medium component are more similar [140].

The cell death that results from a particular electroporation treatment is largely correlated to two parameters: the effective energized time and the induced electric field intensity. Rather than applying a single long pulse, breaking the total energized time into a train of smaller pulses allows similar effects to be obtained as longer pulses, but with significantly less Joule heating and associated thermal damage [132, 141], provided the electrical pulses are delivered in sufficiently close succession [137, 138, 139]. The number of electrical pulses delivered during a specific electroporation treatment is determined by the application. For example, electrochemotherapy and gene electrotransfer rely on molecular entry into a permeabilized cell and thus use a smaller number of electrical pulses from 1 to 8. However, in procedures such as IRE, the goal of the treatment is to destabilize cells for the express purpose of inducing cell death. As such hundreds to thousands of pulses are delivered to ensure maximal cell damage within the target tissue [142].

2.3 Molecular Tracers for Membrane Permeabilization

As cells are electroporated, membrane damage and restructuring result in an increase in membrane permeability to small molecules. In order to study the effects of varying pulse parameters on membrane permeability *in vitro*, two major methods have been developed that utilize the fluorescence intensity from molecular tracers a surrogate measurement for membrane permeability. In the first method, cells are loaded with a reagent, such as FluxOR [90] or Fluo-3 [144], Fura-2/AM [145] prior to electroporation that will bind to with a molecular tracer. When the tracer and the pre-loaded reagent bind in the cell interior, the fluorescence intensity of the complex indicates the relative concentration of the tracer molecule within a cell. The second method relies on cellular structures that natively exist within the cellular anatomy, such as nucleic acids. This method is the more popular of the two as it eliminates the need pre-treat cells. In the more common protocols, an exclusion dye such as propidium [77, 81, 94, 116, 146, 147] or YO-PRO-1 [90, 120, 148, 149, 150, 151]

Table 2.1: Common small molecule nucleic acid exclusion dyes [143].

Solute	CAS No.	M_w (g/mol)	λ_{ex} (nm)	λ_{em} (nm)	z	QY	ε_{max} (cm^{-1} M^{-1})
Propidium	25535-16-4	414.6	533	617	+2		5.9×10^3
TO-PRO-1	157199-59-2	391.6	515	531	+4	0.25	6.28×10^4
TO-PRO-3			642	661	+4	0.11	1.02×10^4
TO-PRO-5			748	768	+4		1.09×10^5
YO-PRO-1		375.5	491	509	+4	0.44	5.20×10^4
YO-PRO-3			612	531	+4	0.16	1.00×10^4
PO-PRO-1	157199-56-9	325.5	435	455	+4	0.39	5.01×10^4
PO-PRO-3		325.5	539	567	+4	0.57	8.79×10^4
JO-PRO-1		376.5	530	546	+4	0.38	9.44×10^4
TOTO-1	143413-84-7	795.1	514	533	+4	0.34	1.17×10^5
TOTO-3			642	660	+4	0.06	1.654×10^5
YOYO-1		763.1	491	509	+4	0.52	9.89×10^4
YOYO-3	156312-20-8	815.1	612	631	+4	0.15	1.67×10^5
POPO-1	169454-15-3	662.9	434	456	+4	0.60	9.24×10^4
POPO-3	154757-99-0	715.0	534	570	+4	0.46	1.46×10^5
BOBO-1			462	481	+4	0.22	1.14×10^5
BOBO-3			570	602	+4	0.39	1.48×10^5
JOJO-1			529	545	+4	0.44	1.71×10^5
7-AAD	7240-37-1	1270.45	546	647	0		2.7×10^4
EthD-1	61926-22-5	715.0	528	617	+4		7.0×10^3
EthD-2		785.0	535	624	+4		8.0×10^3

are introduced into the extracellular buffer prior to the application of an electric field. Due to its simplicity and lack of requirement of pre-loading, this second method is employed in Chapters 3 and 4.

While propidium and YO-PRO-1 are the most common choices of tracer molecules to measure membrane permeability, many of other molecules have been developed that use similar mechanisms (Table 2.1). These molecules dramatically increase their fluorescence intensity upon intercalating DNA or binding to RNA. When a membrane is electroporated, nano-scale pores are formed in the cell membrane and allow enable tracer molecules to enter the cell. The variation in molecular radius between propidium, carbocyanines (YO-PRO-1, etc.), and dimeric cyanines (YOYO-1, etc.) results in a variation in the sensitivity of the permeabilization measurements obtained with each tracer based on how well they pass through an electroporated membrane [90, 151]. Due to its smaller radius, YO-PRO-1 is generally considered more sensitive than propidium, though even smaller tracers such as ionic calcium or ionic thallium have been shown to have even greater sensitivity but require a pre-loaded reagent for fluorescence measurements.

Charge number (z_i) is also an important consideration when selecting a tracer molecule for electroporation studies. When these tracers are employed as an indicator of cell death, the charge number of a particular tracer is less significant as dead cells exhibit a dramatic loss of membrane integrity. However, the generation of pores within the dielectric cell membrane results in an image potential in the presence of charges that opposes their entry into the cell [152]. Many of the common exclusion dyes have a relatively large charge ($z_i = +4$; Table 2.1). Propidium ($z_i = +2$) and 7-AAD ($z_i = +0$) both have smaller charge numbers than YO-PRO-1, which result in smaller image forces opposing their entry into a permeabilized cell. Although smaller tracers such as YO-PRO-1 appear more sensitive than propidium, charge number is still a theoretical consideration common to computational models of electroporation-mediated mass transfer [136, 144, 153].

In addition to the electrical and geometric properties of fluorescent tracer molecules, the optical properties of tracer molecules also impact the permeability measurements obtained using them.

A fluorophore's quantum yield (QY) is the ratio of the photons emitted for each photon absorbed when excited and, in addition to the microscope optics and excitation source, affects the brightness (intensity) of the fluorescence signal. Brightness is calculated as a product of the QY of a fluorescent tracer and its molar extinction coefficient (ε_{max}) [154, 155]. Fluorophores with low QYs generate faint signals and often require longer exposures when imaging them in order to allow the camera to collect enough photons to resolve the image above the background. Due to these longer exposures, low-QY fluorophores impede the rapid imaging of rapid fluorescence changes, such as nucleic acid binding or changes in the distribution of the fluorescence signal. For example, propidium entry into the cell occurs on the order of seconds [94] and intercalating DNA occurs in less than 60 μs [156]. A low QY would make measurements of these phenomenon, and membrane permeability in general, difficult using standard microscopy equipment.

The photostability of the fluorophore in the molecular tracer used to assay electroporation is also critical to fluorescence measurements. Photostability is a measurement of the half-life of the fluorophore brightness and is strongly affected by environmental factors, including pH, its solvent, and the illumination source [157]. Photobleaching occurs when the fluorophore is exposed to light at durations and intensities that irreversibly damage it. Photostability is a crucial consideration when selecting a molecular tracer as the enhanced membrane permeability observed following electroporation can last longer than 30 min (Chapter 4).

In general, a tracer molecule used to assay electroporation *in vitro* using fluorescence microscopy should have a small electrical charge and small molecular radius to mitigate the repulsive forces hindering its passage through the cell membrane. It should also have a large quantum yield and large extinction coefficient to optimize the fluorescence signal to noise ratio. Finally, the fluorophore in the tracer molecule should be as photostable as possible to maximize the duration of experimental observation. Propidium was selected the appropriate tracer molecule for the work in this dissertation due to its small charge number, small radius, and favorable optical properties (Table 2.2).

2.4 Maxwell's Equations and Current Continuity

Electroporation is a bioelectrical phenomenon and that fundamentally relies on the flow of charges, including molecular tracers, small ions, proteins, and other molecules, within biological medium. The flow of these charges generate electrical currents, which are given by Maxwell's equations [158, 159] in their differential forms as

$$\nabla \cdot \mathbf{D} = \rho, \tag{2.1}$$

$$\nabla \cdot \mathbf{B} = 0, \tag{2.2}$$

$$\nabla \times \mathbf{E} = -\frac{\partial \mathbf{B}}{\partial t}, \tag{2.3}$$

$$\nabla \times \mathbf{H} = \mathbf{J}_c + \frac{\partial \mathbf{D}}{\partial t}, \tag{2.4}$$

where $\mathbf{D}$ is the electrical displacement field, $\mathbf{E}$ is the electric field, ρ is the electrical charge density, $\mathbf{J}_c$ is the conduction current, $\mathbf{H}$ is the auxiliary magnetic field, $\mathbf{B}$ is the magnetic field. The constitutive equations relating these quantities are $\mathbf{J}_c = \sigma\mathbf{E}$ (Ohm's law), $\mathbf{D} = \varepsilon\mathbf{E}$, $\mathbf{B} = \mu\mathbf{H}$, where σ, ε, and μ are the electrical conductivity, electrical permittivity and magnetic permeability of a given medium. These values are, by no means, restricted to the real domain or necessarily uniform. Imaginary components represent losses and off-diagonal components represent anisotropies within a material. For an arbitrary geometric domain, exposed to electric field $\mathbf{E}$, a conduction current density $\mathbf{J}_c$ will develop in each direction. $\mathbf{J}_c$ is described as the flow of charged particles (generally, electrons or ions) per unit volume within a given material. Rather than simply allowing electron flow, a material may become polarized in the presence of an electric field at high frequencies. This behavior is known as permittivity and is generally expressed relative to the permittivity of free space ε_0. Permittivity quantifies how much electric flux is generated when the molecular architecture of a given material is manipulated (shifts in dipoles, etc.) to accommodate an applied electric field. Because it takes time for molecules to rearrange when the electric field is applied and removed, the permittivity of a material gives rise to its transient response and may be thought of

as the ability of a material to store electrical energy. Materials with such properties are well-suited for use in discrete electrical components such as capacitors that are designed for that purpose. The displacement (capacitive) current $\mathbf{J}_d$ through a material with permittivity ε is given as

$$\mathbf{J}_d = \frac{\partial \mathbf{D}}{\partial t} = \frac{\partial}{\partial t}(\varepsilon \mathbf{E}). \tag{2.5}$$

A material that exhibits such polarization properties is called a dielectric and its relative permittivity ε may also be referred to as its dielectric constant. By taking the divergence of equation 2.4 and commuting the time and spatial derivatives, the current continuity condition is developed

$$0 \quad = \quad \nabla \cdot \mathbf{J}_c + \frac{\partial}{\partial t}\Big(\nabla \cdot \mathbf{D}\Big), \tag{2.6}$$

as the divergence of the curl of any vector is identically zero. Further, by substitution of the constitutive relations $\mathbf{D} = \varepsilon \mathbf{E}$ and $\mathbf{J}_c = \sigma \mathbf{E}$, the continuity equation in may be rewritten in terms of $\mathbf{E}$ as

$$\nabla \cdot (\sigma \mathbf{E}) + \frac{\partial}{\partial t}\Big(\nabla \cdot (\varepsilon \mathbf{E})\Big) \quad = \quad 0. \tag{2.7}$$

For physical systems containing free charges, the force experienced by a particle i with charge q_i is a combination of an electric and a magnetic force that together comprise the Lorenz force ($\mathbf{F}_i$), given by

$$\mathbf{F}_i = q_i(\mathbf{E} + \mathbf{v}_i \times \mathbf{B}), \tag{2.8}$$

where $\mathbf{v}_i$ is the velocity of the moving particle. For a particle moving sufficiently slowly (non-relativistic), the magnetic induction term is negligible and Coulomb's law is recovered

$$\mathbf{F}_i = q_i \mathbf{E}. \tag{2.9}$$

This comprises the quasi-electrostatic approximation. Alternatively stated, if the electric field vector is approximately irrotational ($\nabla \times \mathbf{E} \approx 0$), the quasi-electrostatic approximation is valid as magnetic induction negligibly contributes to the electromagnetic force experienced by the charged particle.

2.5 Drift-Diffusion of Dilute Charged Species

In physical systems containing free charges, several different modes of mass transport comprise the conduction current $\sigma\mathbf{E}$, including diffusive transport along a concentration gradient, drift facilitated by an electric field, and transport facilitated by the movement of the fluid containing these charges. In the case of a charged solute molecule in the absence of significant magnetic field effects, Coulomb's law describes the electrical force applied to charged molecules. This force results in a translational motion, which reaches a terminal drift velocity $\mathbf{v}_d$. The mobility of a particle μ_i is defined as the ratio of the terminal drift velocity to the applied electric field ($\mu = v_d/\mathbf{E}_0$). For a single particle in an ensemble, the Coulombic flux of molecules is

$$\mathbf{J}_{E_i} = -\mu_i \nabla u, \tag{2.10}$$

where the electric field vector is $\mathbf{E} = -\nabla u$, where u is the scalar electric potential. Casting this net electrical force as a flux of an ensemble of solute molecules of concentration c_i gives

$$\mathbf{J}_{E_i} = -\mu_i c_i \nabla u_i. \tag{2.11}$$

Fick's law is a conservation law in which a concentration of solute is subject to simple diffusion through molecular motion. Fick's first law states that the flux of a molecule $\mathbf{J}_M$ is equivalent to its spatial gradient multiplied by the rate at which diffusion is allowed to occur in each direction, known as the diffusion coefficient. Diffusion coefficients and mobilities (drift coefficients) for common biological molecules are given in Table 2.2. Explicitly, the molecular flux at a point in

space with a concentration of solute c is given by Fick's first law as

$$\mathbf{J}_{M_i} = -Dz_i \nabla c \tag{2.12}$$

were D is the diffusivity. Continuity is expressed through Fick's second law as

$$\frac{\partial c_i}{\partial t} = -\nabla \cdot \mathbf{J}_{M_i} = \nabla \cdot (D_i \nabla c_i). \tag{2.13}$$

Alternatively stated, Fick's second law states that the change in concentration of a solute c at a point in space is equivalent the the sum of the fluxes through that point. The flow of a fluid containing charged particles c_i flowing with a velocity $\dot{\mathbf{x}}$ also contributes to the flux of the molecular ensemble. The electrical flux density of c_i in such a flow is given by

$$\mathbf{J}_{F_i} = -z_i c_i \dot{\mathbf{x}}. \tag{2.14}$$

Substituting these fluxes into equation 2.6 yields

$$\nabla \cdot \left(\sum_i \mathbf{J}_{M,i} + \sum_i \mathbf{J}_{F,i} + \sum_i \mathbf{J}_{E,i} \right) + \frac{\partial}{\partial t} \left(\nabla \cdot (\varepsilon \mathbf{E}) \right) = 0, \tag{2.15}$$

where $\mathbf{J}_M + \mathbf{J}_F + \mathbf{J}_E$ is the flux density of the free charges i and $\varepsilon \mathbf{E}$ is the flux of bound charges. Fick's second law applied to free charged particles provides a mass balance of the free charges that yields the canonical form of the Nernst-Planck equation that describes the transport of species i given by

$$\begin{aligned} \frac{\partial c_i}{\partial t} &= -\frac{1}{z_i} \nabla \cdot (\mathbf{J}_M + \mathbf{J}_F + \mathbf{J}_E), \\ &= \nabla \cdot \left[D_i \nabla c_i - c\dot{\mathbf{x}} + \frac{\mu_i}{z_i} c_i \nabla u \right]. \end{aligned} \tag{2.16}$$

Substituting the $\partial c_i/\partial t$ terms for all charged species i back into equation 2.15 generates

$$0 \quad = \quad \frac{\partial}{\partial t}\left(\sum_i z_i c_i + \nabla\cdot(\varepsilon\mathbf{E}),\right). \tag{2.17}$$

Integration of 2.17 in time yields Gauss' Law $\rho_i - \varepsilon\nabla^2 u = 0$ in the form of Poisson's equation

$$\nabla^2 u \quad = \quad \frac{F}{\varepsilon}\sum_i z_i c_i. \tag{2.18}$$

where $\rho_i = z_i F c_i$ is the charge density of species i and F is Faraday's constant. This coupling of mobile charge concentrations of species c_i to the electric potential field u results in the formulation of a Poisson-Nernst-Planck (PNP) system under the quasi-electrostatic assumption within a given spatial domain $\Omega \in \mathbb{R}^3$

$$\begin{cases} \dfrac{\partial c_i}{\partial t} = \nabla\cdot\left(D_i\nabla c_i - c_i\dot{\mathbf{x}} + \mu_i c_i \nabla u\right), & \forall c_i \in \Omega \\ \nabla^2 u = \dfrac{1}{\varepsilon}\sum_i q_i c_i, & \forall u \in \Omega \end{cases}. \tag{2.19}$$

Often, within a medium with a low dielectric constant, PNP systems reach equilibrium quickly ($\partial c_i/\partial t \approx 0$) and flow conditions are negligible ($\dot{\mathbf{x}} \approx 0$; Fig. 2.2). Under such conditions, equation 2.16 reduces to the balance

$$\mathbf{J}_{E_i} + \mathbf{J}_{M_i} = -\mu_i c_i \nabla u - D_i \nabla c_i = 0, \tag{2.20}$$

where the flux due to electrical drift and the flux due to diffusion are at equilibrium. By rearrangement and the chain rule applied to equation 2.20,

$$\nabla c_i = \frac{dc_i}{du}\nabla u, \tag{2.21}$$

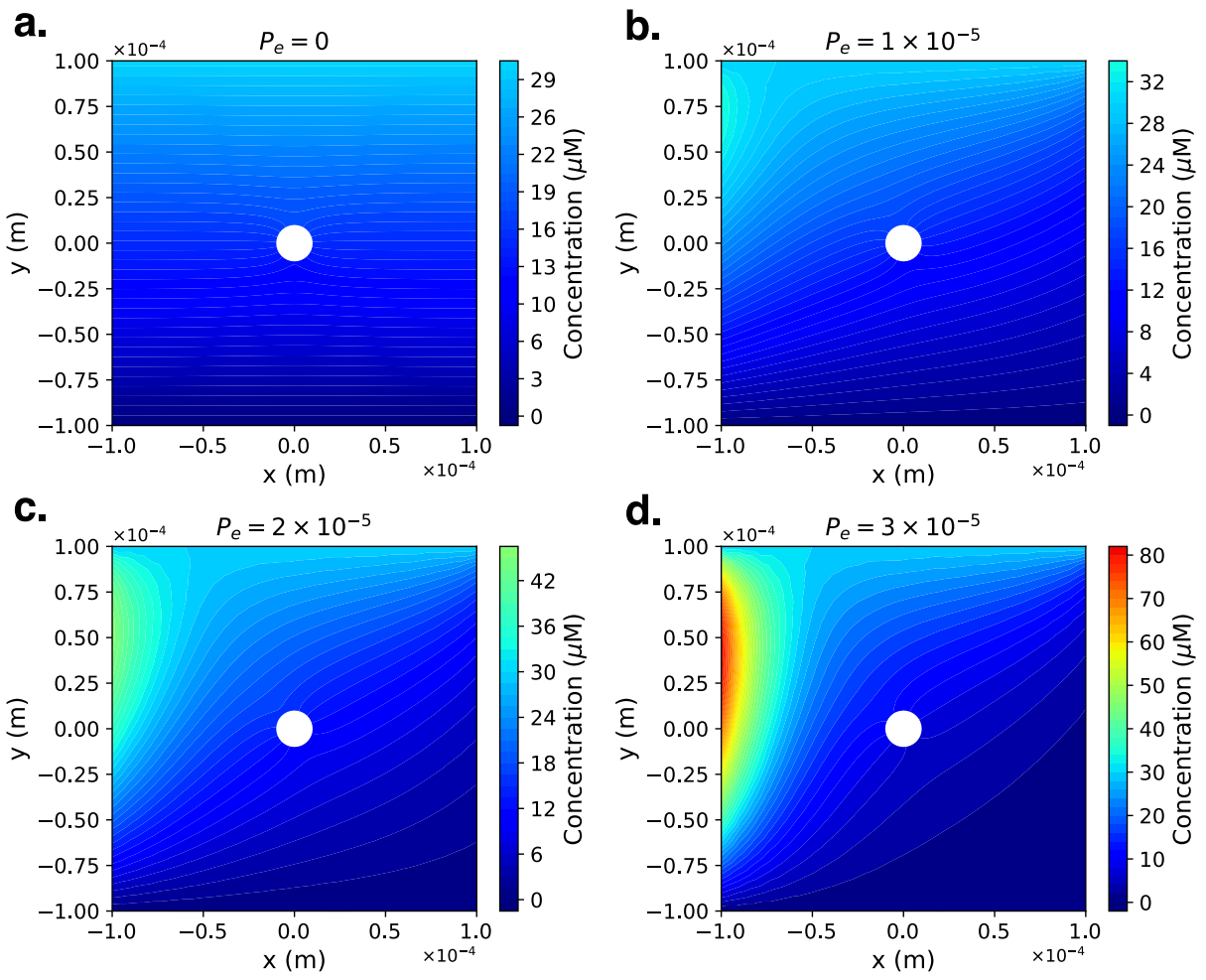

Figure 2.2: Steady state simulations of diffusion and drift of a dilute charged solute ($z_i = +2$) around a circular occlusion in two dimensions. (a) In the absence of an applied electric field, the simple diffusion of the charged solute was simulated with the top boundary set to 30 μM and the lower boundary set to 0 μM. The application of electric fields of strengths (b) 0.1, (c) 0.2, and (d) 0.4 μV/m generate Péclet numbers ($P_e = z_i F \nabla u/(RT)$) from 0 to 3×10^{-5} affect the resultant distribution of the charged solute. In all simulations, a positive voltage was applied on the right boundary and the negative voltage placed on the left boundary.

which yields

$$\left(\mu_i c_i + D\frac{dc_i}{du}\right)\nabla u = 0. \tag{2.22}$$

The Maxwell-Boltzmann distribution describes the expected concentration of particles c_i that exists at a given potential u as

$$c_i = Ae^{-z_i F u/(RT)}, \tag{2.23}$$

where R is the universal gas constant, and T is the temperature. dc_i/du from equation 2.23, substituted into equation 2.22, yields the Einstein relation

$$\mu_i \quad = \quad \frac{D_i z_i F}{RT}. \tag{2.24}$$

Table 2.2: Bulk properties of common small molecule solutes including molecular weight (M_w) given in g/mol, elemental charge (z_i), van der Waals (V_s) in nm^3, radius of spherical approximation (r_s) given in nm, electrophoretic mobility (μ_i) calculated using equation 2.24 and given in ($\times 10^{-8}$) m^2/(V·s), and diffusion coefficient (D_i) in m^2/s. Calculations performed at $T = 298$ K. Values from [101, 136]

Solute	M_w	z_i	V_s	r_s	μ_i	D_i
ATP	507.2	-3.49	0.379	0.62	-5.57	0.41
Ca^{2+}	40.1	+2.00	0.034	0.2	7.63	0.98
Calcein	622.5	-3.61	0.520	0.58	-6.60	0.47
Cl^-	35.5	-1.00	0.023	0.18	-4.36	1.12
FITC	389.4	-0.05	0.310	0.60	-0.10	0.49
Fluoroscein	332.3	-0.05	0.271	0.57	-0.10	0.49
Glucose	180.2	0.00	0.150	0.32	0.00	0.73
K^+	39.1	+1.00	0.087	0.28	0.00	0.70
Na^+	23.0	+1.00	0.049	0.23	3.31	0.85
Propidium	414.6	+2.00	0.404	0.69	3.35	0.43
Sucrose	342.3	0.00	0.283	0.45	0.00	0.52
YO-PRO-1	375.5	+2.00	0.353	0.53	4.12	0.53

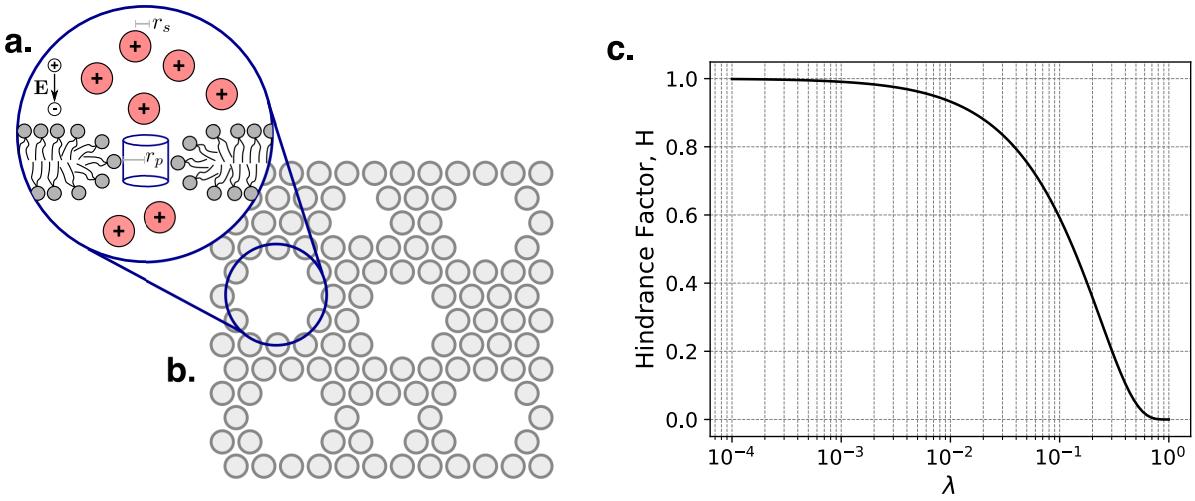

Figure 2.3: Electrical drift and diffusion along concentration gradients govern the the transport of charged solutes. (*a*) The transmembrane transport of a positively-charged species, such as propidium ($z_i = +2$) is governed by the local electric field at the cell membrane as well as the concentration gradient across it at each pore. (*b*) Many pores exist in an electroporated cell membrane resulting in many parallel ion fluxes as charged solutes flow through each pore. (*c*) The hindrance factor (H) for the transport across the porous cell membrane depends on the ratio of the solute radius to the pore radius ($\lambda = r_s/r_p$) and expresses a porous membrane's net resistance to molecular transport.

2.6 Mass Transport Through a Semipermeable Membrane

Diffusive mass transport through a semipermeable membrane is described by a linearization of Fick's law at the membrane center. In cells, membrane permeability may be assessed using exclusion dyes, such as those in Table 2.1. The permeability equation is

$$(\mathbf{J}_i + \mathbf{J}_e) \cdot \mathbf{n}|_m = \frac{D_{m,i}}{h}(c_0 - c_i). \tag{2.25}$$

where $c_0 - c_i$ is the concentration differential across the membrane thickness, and $D_{m,i}$ is the diffusion coefficient of particle i through the cell membrane of thicknesss h. Considering the mass transport through the cell membrane as a continuum of parallel ionic currents allows membrane transport to be considered hindered diffusion with a hindrance factor H accounting for the resistance the membrane provides to the mass transport across it. The membrane hindrance depends on the ratio of the radius of the solute (r_s) and the radius of the membrane pores (r_p) where $\lambda_M = r_s/r_p$

and is given by the empirical relationship [160, 161]

$$H = \frac{9}{8}\lambda_M \log(\lambda_M) - \sum_{k=0}^{7} a_k \lambda_M^k. \tag{2.26}$$

This formula has been corrected for solutes of radii similar to the radii of the membrane pores and where $a_0 = 1$, $a_1 = -1.56034$, $a_2 = 0.528155$, $a_3 = 1.91521$, $a4 = -2.8190$, $a_5 = 0.270788$, $a_6 = 1.10115$, and $a_7 = 0.435933$. The parallel ionic currents through pores with surface area πr_p^2 on a membrane fraction with area A can therefore be modeled as

$$(\mathbf{J}_i + \mathbf{J}_e) \cdot \mathbf{n}|_m = \frac{\pi r_p^2 HND_i}{h}(c_0 - c_i), \tag{2.27}$$

where N is the surface density of membrane pores. In the absence of a velocity field, the flux of charged solutes subject to drift and diffusion across a thin membrane is given by

$$(\mathbf{J}_i + \mathbf{J}_e) \cdot \mathbf{n}|_m = -\mu_i c_i \frac{du}{dx} - D_i \frac{dc_i}{dx}, \tag{2.28}$$

where $\mathbf{J}_i$ and $\mathbf{J}_e$ are the internal and external molecular fluxes and du/dx and dc_i/dx are the fluxes along the outward-facing normal $\mathbf{n}$ of the membrane. The potential gradient through an isolated pore structure varies with position within the pore according to

$$u = u_i + \frac{u_m}{\log(\sigma_e/\sigma_i)} \log\left(1 + \frac{x}{h}(\sigma_e - \sigma_i)\right), \tag{2.29}$$

where $\log(\cdot)$ is the natural logarithm, σ_e is the conductivity of the extracellular medium, σ_i is the cytoplasmic (intracellular) conductivity, $u_m = u_i - u_e$ is the transmembrane potential, u_i is the electrical potential immediately inside the cell membrane, and u_e is the electrical potential immediately outside the cell membrane [79]. Applying this result to the membrane flux balance yields

$$(\mathbf{J}_i + \mathbf{J}_e) \cdot \mathbf{n}|_m = \frac{D_i}{h}\left(\frac{(Pe - \log(\sigma_e/\sigma_i)}{(\sigma_e/\sigma_i) - e^{Pe}} \frac{(\sigma_e/\sigma_i - 1)}{\log(\sigma_e/\sigma_i)}\right)(c_e - c_i e^{Pe}), \tag{2.30}$$

through simple integration with respect to the spatial coordinate x where $Pe = -z_i F u_m/(RT)$ [144]. Equation 2.30 is similar to equation 2.27 except for corrections to account for the molecular drift through the membrane. Considering both drift and hindered diffusion therefore leads to

$$(\mathbf{J}_i + \mathbf{J}_e) \cdot \mathbf{n}|_m = P_0 N (c_e - c_i e^{Pe}), \tag{2.31}$$

where

$$P_0 = \left(\frac{\pi r_p^2 H D_i}{h}\right)\left(\frac{\sigma_e/\sigma_i - 1}{\log(\sigma_e/\sigma_i)}\right)\left(\frac{(Pe - \log(\sigma_e/\sigma_i)}{(\sigma_e/\sigma_i) - e^{Pe}}\right). \tag{2.32}$$

Intuitively, when $\sigma_e = \sigma_i$ in the bulk solution on either side of the membrane, $P_0 = 0$, indicating no charge accumulation occurs. If the membrane does not contain any pores ($N = 0$), then $P_0 = 0$. The only non-physical condition in equation 2.31 occurs when $Pe = 0$, which arises with the $u_m = 0$. However, this discontinuity is removable and the final value of P_0 at $Pe = \log(\sigma_e/\sigma_i)$ is defined as the piecewise function

$$P_0 = \left(\frac{\pi r_p^2 H D_i}{h}\right)\left(\frac{\sigma_e/\sigma_i - 1}{\log(\sigma_e/\sigma_i)}\right)\begin{cases} \dfrac{(Pe - \log(\sigma_e/\sigma_i)}{(\sigma_e/\sigma_i) - e^{Pe}}, & Pe \neq \log(\sigma_e/\sigma_i) \\ -\dfrac{\sigma_i}{\sigma_e}, & Pe = \log(\sigma_e/\sigma_i) \end{cases}, \tag{2.33}$$

which includes corrections for both hindered diffusion and electrophoretic drift as a function of the membrane pore surface density (N).

2.7 Membrane Breakdown and Pore Formation

An intact bilayer membrane will form spontaneously in an aqueous medium. Once formed, a membrane is subject to thermodynamic fluctuations that govern its structural properties at the molecular level: the distance between charged lipid head groups fluctuates while maintaining the hydrophobic membrane core [162]. Representing these random fluctuations as a statistical distribution, it becomes conceivable that there is a small probability that the random motion of the lipid molecules

in the bilayer membrane will generate a defect in the membrane structure in which an intramolecular space will form that is large enough to permit a molecule to penetrate the hydrophobic core and emerge on the opposite side [12, 73, 163, 164, 165, 166]. The cellular membrane functionally isolates the interior of a cell from its external environment, thereby establishing chemical gradients that the cell utilizes for generating action potentials, nutrient uptake, and waste export. These chemical gradients establish an osmotic gradient across the relatively impermeant membrane. Due to the electrical charge distribution within many of these molecules, the chemical gradient established across the cell membrane also establishes a large electrical gradient -65 to -70 mV [60]. When an electric field is applied across a cell, opposing charges gather at each side of the membrane and generate an electrically-induced pressure across the membrane. When this pressure surpasses a threshold, defects in the membrane form form and are expanded, allowing molecular transport into and out of the cell.

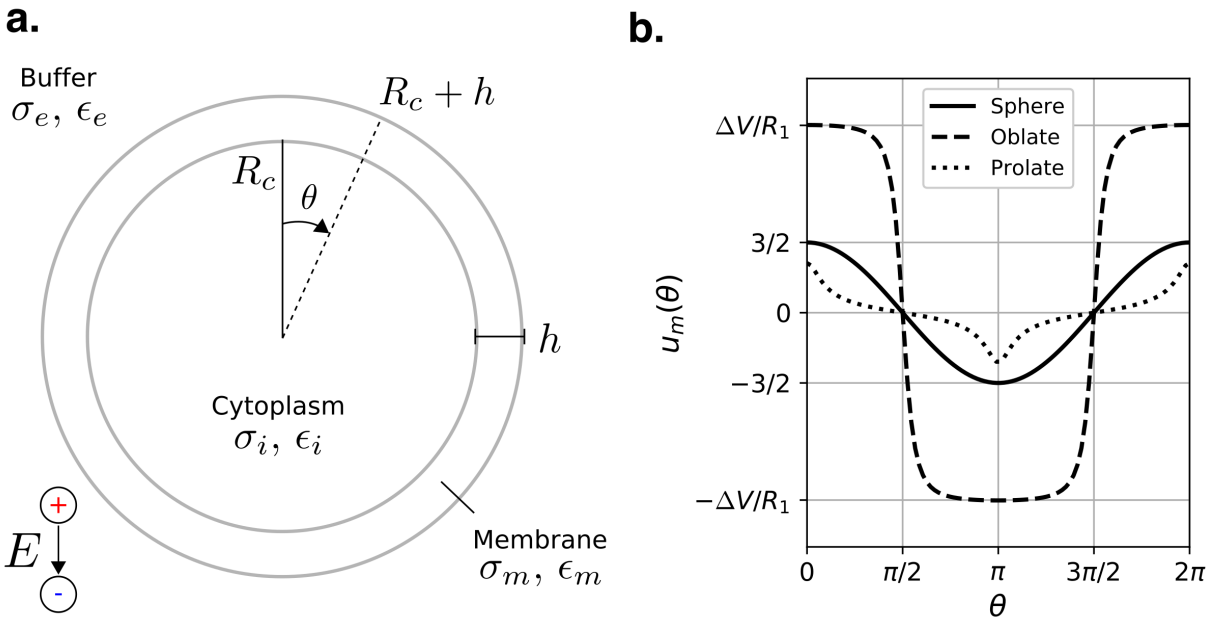

Figure 2.4: An idealized, single-shell model of a spherical cell containing domains for the extracellular buffer with conductivity σ_e and permittivity ε_e, a thin membrane with thickness h, conductivity σ_m and permittivity ε_m, and a spherical intracellular domain with radius R_c, conductivity σ_i and permittivity ε_i.

H. P. Schwan derived an expression that now carries his name for the transmembrane potential

induced by an external electric field applied to a spherical cell [61]. The Schwan equation is commonly employed to provide an intuitive, analytical description of the mechanism giving rise to the electroporation phenomenon. The formulation of the Schwan equation considers concentric spherical regions to represent a cell. The transmembrane potential is the difference in potential in the radial direction across the thin dielectric membrane shell separating the conductive intracellular region from the conductive extracellular region. In such a case, the transmembrane potential ($u_m = u_i - u_e$) is defined as

$$u_m(r,\theta) = f_s E_0 R_c \cos(\phi), \tag{2.34}$$

where R_c is the radius of the cell, measured to the interior surface of the membrane, ϕ is the polar angle, and $|\mathbf{E}| = E_0$ is the applied electric field in the radial direction in which the cell is immersed, and

$$f_s \quad = \frac{2\sigma_e\Big[3hR_c^2\sigma_i + (3h^2R_c - h^3)(\sigma_m - \sigma_i)\Big]}{2R_c^3\Big(\sigma_m + 2\sigma_i\Big)\Big(\sigma_m + \frac{1}{2}\sigma_i\Big) - 2(R_c - h)^3\Big(\sigma_e - \sigma_m\Big)\Big(\sigma_i - \sigma_m\Big)}.$$

In this case, the cell membrane has a thickness of h and the radius of the cell to the internal surface of the membrane is R_c. The conductivity of the cytoplasm, membrane, and extracellular medium are given as σ_i, σ_m, and σ_e respectively. In reality, there is a time-dependence on the induced transmembrane potential u_m. This time dependance can be approximated through further simplifications performed under the conditions that the membrane diameter is much smaller than the radius of the cell ($h << R_c$). Through substitution of $\sigma + j\varepsilon_m\omega$ for σ in order to obtain the transient components of the transmembrane potential given by the Schwan equation, if the permittivities of the internal and the external media are negligible ($\varepsilon_i \approx \varepsilon_e \approx 0$), and the conductivities are significantly greater than that of the membrane ($\sigma_m << \sigma_i, \sigma e$), the membrane charging time constant τ is given by

$$\tau = \frac{R_c\varepsilon_m}{2h\Big(\frac{\sigma_i\sigma_e}{\sigma_i + 2\sigma_e}\Big) + R_c\sigma_m},$$

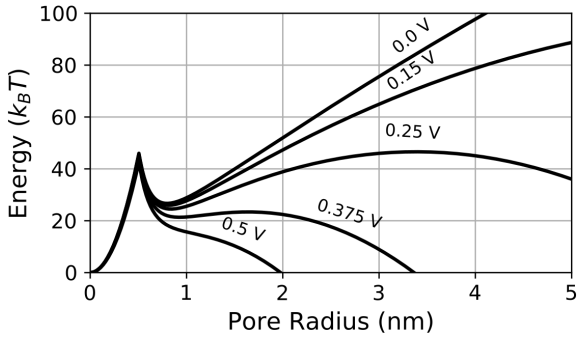

Figure 2.5: With increasing transmembrane potential, the energy of an electropore decreases beyond the generation of a 0.8 nm pore, where the local energetic minimum exists. Pore formation is a process that involves the expansion of a membrane defect within an intact membrane into a hydrophobic pore. Hydrophobic pores quickly becomes a hydrophilic pore as phospholipids migrate to line the pore.

and allows the time-dependent Schwan equation to be rewritten as

$$u_m(R_c,\theta,t) = f_s E_0 R_c \cos(\theta)\left(1-\exp\left(-\frac{t}{\tau}\right)\right), \tag{2.35}$$

It is important to note that the transmembrane potential expression is similar for prolate, oblate, and spherical cells, yet the oblate geometry experiences a considerably larger surface area of the membrane to larger transmembrane potentials than the prolate geometry [49, 167]. In practical terms, this indicates that cells positioned with their long axes perpendicular to the electric field (oblate) will exhibit a significantly greater average membrane permeabilization than if they are their long axis is parallel to the electric field.

In 1979, Abidor and colleagues linked the increased molecular transport observed following electroporation in bilayer membranes with the generation of membrane defects arising from the colloidal nature of lipid bilayers [12]. In so doing, they developed the modern biophysical explanation underpinning modern electroporation theory in which these pores evolve along their radius spaces along the cell membrane. Given that a generalized force $\mathbf{F}$ is given by $\mathbf{F} = -\nabla U$ where U is the pore energy, the flux $\mathbf{S}_r$ along the radius space of a pore is given by a Smolchowski-type model [73, 165, 168] as

$$\mathbf{S}_r = \frac{dN}{dt} - D_r\left(\nabla N + \frac{N}{k_B T}\nabla U\right), \tag{2.36}$$

where N is the pore density distribution, D_r is the diffusion coefficient in pore radius space, and k_B and T are Boltzmann's constant and the temperature, respectively. The pore energy U is conven-

tionally given as the minimum of two curves: one curve representing the energy of a hydrophobic pore and one curve representing a hydrophilic pore. Later, Neu et al. simplified the explanation of the second type of defects that form as hydrophilic pores by introducing a quadratic term to represent the energy of this enlarged defect—termed a hydrophobic pore—rather than the modified Bessel functions used previously [168]. Once the radius of a defect reaches a critical value, denoted $r = r_*$, the lipid head groups invert and energetically stabilize the pore, bridging the two membrane leaflets and creating a hydrophilic pore (Fig. 2.5). This stabilization is reflected as a local minimum in the energy function $r_m > r_*$, and indicates that once hydrophilic pores are formed, they tend to aggregate at $r = r_m$ before collapsing back to an intact membrane. Physically, these dynamics are captured by modeling a hydrophobic pore using the quadratic term proposed by DeBruin et al. such that a global minimum energy is achieved at $r = 0$, where the hydrophobic pore of radius is normalized to the radius at which the hydrophilic-hydrophobic transition occurs r_*. The energy associated with that transition is denoted $U(r_*) = U_*$. The hydrophilic pore energy is developed by considering a dielectric material separating two bulk phases of a conducting material. The term $\pi a_p r^2 u_m^2$ represents the electrical energy that motivates the transition of a hydrophobic to hydrophilic pore, similar to a discrete capacitor. The inside of a hydrophilic pore is associated with a linear tension $2\pi r\gamma$ and the whole membrane experiences a surface tension $\pi r^2\Gamma$ where γ and Γ are the line tension and surface tension of the pore, respectively. An additional term is added here as a quartic term to represent the steric interactions of the lipid head groups in the pore with C as the interaction constant. Together, with the introduction of an exogenous electric field added to the energy function,

$$U(r) = \begin{cases} U_*\left(\dfrac{r}{r_*}\right)^2 - \pi a_p r^2 u_m^2 & 0 \le r \le r_* \\ 2\pi r\gamma - \pi r^2\Gamma - \pi a_p r^2 u_m^2 + \left(\dfrac{C}{r}\right)^4 & r_* < r < h \end{cases}, \tag{2.37}$$

where u_m is the transmembrane potential and a_p accounts for the difference in dielectric properties

between an intact membrane and the surrounding aqueous environment, estimated as [12, 169]

$$a_p = \frac{\varepsilon_w - \varepsilon_l}{2h},$$

where ε_w and ε_l are the permittivities of the water in the surrounding aqueous environment and of the constituent phospholipids, respectively. Approximate values for all constants are given in Table 2.3. Dramatic deformation for $r > r_*$ occurs at potentials on the order of 200 mV, and have been experimentally measured to be between 0.2 to 1.0 V [85].

Reduction of the Smolchowski-type PDE model to an ODE model cast the equations governing the nucleation of a pore to be readily integrated with models of electric field distributions. Originally presented in [168], we briefly review the methods and assumptions used to eliminate the spatial dependence of the Smolchowski-type PDE. The source term $\mathbf{S}_r$ from the Smolchowski-type model has been modeled as a two step process in which pores with energies between U and $U + dU$ are generated at a rate

$$\frac{dN}{dt} = \nu_c h e^{-U/k_B T} d\left(\frac{U}{k_B T}\right), \tag{2.38}$$

where ν_c is the "attempt rate density"—or the frequency with which pore formation has the potential to occur [180]. It follows by substitution of the relation $dU = U dr$ from equation 2.37 that the formation of a pore with radius between r and $r + dr$ is given by

$$|\mathbf{S}_r| = \nu_c h \frac{U}{k_B T} e^{-U/k_B T} - \nu_d N H(r_* - r), \tag{2.39}$$

with the addition of a pore destruction rate of hydrophobic pores ν_d to model the net rate of pore formation. The Heaviside step function $H(r_* - r)$ represents the fact that only hydrophobic pores may be destroyed. In constraining the source term in this manner, it must be noted that there is an implicit assumption that all pores are created as hydrophobic pores and all pores are destroyed but not before passing back through a hydrophobic stage. The initial condition $n(0,t) = 0$ is applied, indicating that pores of radius zero do not exist. A hydrophobic pore is created through two routes:

Table 2.3: Typical electrical and morphological properties of cellular components of an isolated cell. Adapted from [72, 168, 170, 171].

Variable	Value	Unit	Parameter	Reference
ε_0	8.854×10^{-12}	As/(V·m)	Permittivity of free space	
k_B	1.380648×10^{-23}	m^2·kg/(s^2·K)	Boltzmann's constant	
R	8.314	J/(mol·K)	Universal Gas Constant	
T	300	K	Physiological temperature	
$\varepsilon_e\varepsilon_0$	$75\varepsilon_0$ - $85\varepsilon_0$	As/(V·m)	Saline permittivity	[64, 125, 126, 172, 173, 174]
σ_e	1.0	S/m	Saline conductivity	Chapter 4
$\varepsilon_m\varepsilon_0$	$2\varepsilon_0$ - $13.5\varepsilon_0$	As/(V·m)	Cell membrane permittivity	[64, 125, 126, 174]
σ_m	0.1×10^{-10} - 5.6×10^{-5}	S/m	Cell membrane conductivity	[64, 125, 126, 174, 175, 176]
h	4	nm	Cell membrane thickness	[177]
ε_i	$60\varepsilon_0$ - $154.4\varepsilon_0$	As/(V·m)	Cytoplasm relative permittivity	[125, 126, 174, 176]
σ_i	0.3 - 1.3	S/m	Cytoplasm conductivity	[125, 126, 174, 176]
$\varepsilon_{nm}\varepsilon_0$	$28\varepsilon_0$ - $41\varepsilon_0$	As/(V·m)	Nuclear membrane permittivity	[125, 126, 174, 178]
σ_{nm}	3×10^{-3} - 6×10^{-3}	S/m	Nuclear membrane conductivity	[125, 126, 174, 178]
h_{nm}	$1-40$	nm	Nuclear membrane thickness	[125, 126, 178]
$\varepsilon_n\varepsilon_0$	$52\varepsilon_0$ - $120\varepsilon_0$	As/(V·m)	Nucleoplasm permittivity	[125, 126, 174, 178]
σ_n	0.95 - 1.35	S/m	Nucleoplasm conductivity	[125, 126, 174, 178]
R_n	3	μm	Nuclear radius	[126]
R_c	7.5	μm	Mammalian cell radius	Chapter 4
r_p	0.8	nm	Pore radius	[73]
σ_p	1.3	S/m	Hydrophilic pore conductivity	[72]
u_{th}	258	mV	Threshold electroporation potential	[72]
Γ	10^{-3}	J/m	Interfacial tension	[179]
γ	1.8×10^{-11}	J/m	Pore edge energy	[73]
C	9.67×10^{-15}	$J^{1/4}$/m	Steric constant	[73, 166, 168]
r_*	0.5	nm	Critical pore radius	[73]
E_*	$45k_BT$	J	Hydrophobic pore energy constant	[73]
$\varepsilon_l\varepsilon_0$	$2\varepsilon_0$	As/(V·m)	Lipid permittivity	[73]
ε_w	$80\varepsilon_0$	As/(V·m)	Aqueous medium permittivity	[73]

either $r < r_*$ or $r > r_*$. The formation of pores $r < r_*$ is significantly smaller than the rate of pore formation for $r > r_*$ and therefore, by extension of the absorbing boundary condition, the approximation $n(r_*,t) = 0$ is justified. In so doing, the boundary value problem is effectively reduced to

$$\frac{U}{k_B T}\left(\frac{E_* r_*^2 \nu_d}{D_r}\right) e^{-UE_*/k_B T} = \frac{dN}{dt} - D_r \frac{\partial}{\partial r}\left(N + \frac{n}{k_B T} U\right). \tag{2.40}$$

Through further approximation and simplification [168], it has been shown that the pore density N(t) is well approximated as

$$\frac{dN}{dt} = \alpha e^{(u_m/u_{th})^2}\left(1 - \frac{N}{N_{eq}(u_m)}\right) \tag{2.41}$$

where

$$N_{eq}(u_m) = N_0 e^{q(u_m/u_{th})^2}. \tag{2.42}$$

and where N_0 is the equilibrium pore number, u_m is the transmembrane potential, u_{th} is the transmembrane potential electroporation threshold, and α and q are fitting parameters. The transformation of the Smoluchowski-type pore nucleation PDE model to the asymptotic Smoluchowski-type ODE model (ASM) enables the formation of pores to be modeled efficiently in existing computational strategies, such as a transport lattice network [181] or a finite element [144, 153, 182], finite volume, or finite difference framework [183, 184, 185].

2.8 Conclusion

Here, we have outlined the current state of the biophysical mechanisms underlying electroporation. Beginning from Maxwell's equations, we have derived the electrostatic potential field that is typically utilized in calculations related to the transmembrane potential induced by an electroporation treatment. By further simplification, we arrived at the passive Schwan model of transmembrane potential. We briefly reviewed a conventional model of pore formation based on Smoluchowski-type

energetics and the role electrodiffusion plays in mass transport across the cell membrane following electroporation. These fundamental relationships will herein guide the discussion of electroporation and will be used extensively in the discussion of possible mechanisms that appear in our experimental results.

Chapter 3

Quantification of cell membrane permeability induced by monopolar and high frequency bipolar bursts of electrical pulses

Daniel C. Sweeney[a], Matej Reberšek[b], Janja Dermol[b], Lea Rems[b], Damijan Miklavčič[b], and Rafael V. Davalos[a*]

[a] Department of Biomedical Engineering and Mechanics, Virginia Tech, Blacksburg, VA, USA

[b] Faculty of Electrical Engineering, University of Ljubljana, Ljubljana, Slovenia

* Corresponding author

Author Contributions

DCS and MR conceived of and performed the experimental portion of this work and wrote and edited the manuscript. JD and LR conceived of and assisted in experimental development and design and edited the manuscript. RVD and DM conceived of and edited the manuscript.

The following chapter was published under the citation: **DC Sweeney**, M Reberšek, J Dermol, L Rems, D Miklavčič, and RV Davalos. *Quantification of cell membrane permeability induced by monopolar and high frequency bipolar bursts of electrical pulses*. BBA-Biomembranes. 1858(11), pp.2689-2698. (2016).

3.1 Introduction

Biological membranes are critical to maintaining cellular homeostasis by isolating a cell's interior from its extracellular environment. The cell utilizes its membrane as a barrier to general transport, but allows for the controlled exchange of valuable nutrients, chemical signals, and waste products through transmembrane structures, which shuttle molecules into and out of the cell and maintain the precise homeostatic balance necessary for the cell's function and survival. When biological membranes are exposed to sufficiently intense pulsed electric fields (PEFs), their permeability increases, enhancing the molecular exchange between the cell and its environment. This phenomenon, known as electroporation or electropermabilization, enables processes like gene transfection [186, 187] and chemotherapy [188, 189] to be performed much more efficiently. Molecular dynamics simulations have suggested that the formation of pores in the lipid bilayer occurs when water molecules align at the water-bilayer interface and are driven through the hydrophobic bilayer core by local electric field gradients [14, 71, 190, 191]. When water molecules cross the membrane, the surrounding lipid head groups usually follow the penetrating water molecules into the pore to energetically stabilize the pore structure [12, 190, 192]. This restructuring of the lipid bilayer has been hypothesized to alleviate the electrotension caused by collection of oppositely-charged ions on each side of the membrane [130, 131]. As long as the electric field is sustained, the pore can further expand in size facilitating the transport of ionic/molecular species across the pore [73, 168, 193]. Nevertheless, other mechanisms have been proposed to explain the increased cell membrane permeability caused by electric pulses, such as lipid peroxidation and restructuring of the membrane due to changes in membrane protein conformation [183, 194].

Electroporation has been used clinically to either directly ablate tumor tissue or transiently increase membrane permeability to enhance drug delivery at the target sites inside the cell interior. In irreversible electroporation (IRE), the cellular membrane is disrupted to generate an irrecoverable homeostatic imbalance [16, 141, 195, 196]. In gene electrotransfer (GET) [35, 40] or electrochemotherapy (ECT) [48, 197, 198], electroporation enables therapeutic molecules to be more

efficiently delivered into cells. During an ECT procedure, a drug such as cisplatin [44, 199] or bleomycin [45, 134, 200] is first injected into a tumor site and is shortly followed by a PEF treatment, enabling the chemotherapeutic drugs to be administered with greater potency by overcoming the cell membrane's transport barrier. Because ECT is delivered locally to the tumor site, minimal systemic side-effects present as a direct result of the treatment while retaining an equivalent or greater clinical efficacy compared to traditional chemotherapy [37, 201, 202, 203]. GET is a non-viral gene transfer method that depends on PEF treatment to enhance the delivery of therapeutic genetic material [34, 204]. By inserting DNA carrying specific genetic code into cells, GET enables targeted introduction, replacement, or inactivation of selected genes. PEF treatment has dramatically improved gene-transfer efficiencies in tissues such as liver, skin, and skeletal muscle [35, 205, 206, 207].

IRE technology has been used to treat tumors in canine brain tissue [208], human and porcine liver tissue [209, 210, 211, 212], and and human and porcine pancreatic tissue [25, 213, 214]. By destroying malignant cells while mitigating damage to critical stromal tissue components [215, 216], it enables the treatment of tissues around critical structures that would otherwise render the site untreatable. A notable recent improvement in IRE has been termed high-frequency IRE (HF-IRE) and replaces the long monopolar pulsing schemes traditionally used in IRE (80×100 μs-long pulses delivered at 1 Hz) with bursts of short bipolar pulses [141]. These bursts of short pulses partially mitigate intra-operative impedance changes [140] and virtually eliminate muscle contractions [141, 217, 218, 219] during the treatment to potentially improve both current treatment planning algorithms [141, 220] and the procedural safety for the patient due to the reduced need for neuroparalytic drugs typically required to inhibit muscle contraction. For the same reason, bursts of short pulses could also be advantageous in ECT and GET, which have historically utilized pulse widths of hundreds of microseconds to milliseconds to permeabilize the cell membrane.

In the food processing industry, however, PEFs comprised of trains of pulses of 1 to 10 microseconds are routinely used to kill pathogenic and spoilage microorganisms around vegetal and animal tissue [221, 222]. Only recently has such electroporation been studied in mammalian tissue for

medical applications that utilize controlled, square electrical pulses on the order of one microsecond [195, 223]. The observations about PEFs with single-microsecond pulse widths from the field of PEF-based food processing do not directly provide information on the efficiency of these pulses to enhance molecular transport across mammalian cell membranes. Consequently, more detailed study of the molecular transport occurring between a mammalian cell and its environment is needed during these types of pulses. We thereby aimed in the present study to compare membrane permeabilization obtained with 1 μs bipolar pulses and conventional 100 μs pulses, used in IRE and ECT.

In order to characterize molecular transport induced by different pulsing protocols, we performed real-time microscopic imaging of propidium iodide (PI) transport at the single cell level during and after PEF treatment. The measured changes in PI fluorescence intensity due to the uptake and subsequent binding of PI ions to intracellular nucleic acids enabled us to calculate the time course of the effective permeability of a cell membrane. This method can be further refined and validated against mechanistic models of the electroporation and membrane permeabilization processes to advance electroporation-based treatments and therapies. The results presented herein demonstrate that high-frequency bipolar electrical pulses may be designed to achieve similar degrees of electroporation as current IRE, ECT and GET pulsing schemes, but induce more symmetrical transmembrane uptake of small molecules than conventional treatments.

3.2 Materials & Methods

3.2.1 Cell Preparation

Chinese hamster ovary (CHO-K1) cells were obtained from the European Collection of Authenticated Cell Cultures and grown in HAM-F12 medium (PAA, Austria) supplemented with 10% fetal bovine serum (Sigma-Aldrich, Steinhei, Germany), 1 mM L-glutamine (StemCell Technologies, Vancouver, Canada), 5 mg/mL gentamicin (Sigma-Aldrich), and 0.01 μL/mL penicilin-streptomicin

(PAA) at 37°C under 5% CO_2. Cells were allowed to become $70-80\%$ confluent before being trypsinized, resuspended, and transferred into glass-bottom Lab-Tek II chambers (Nalge Nunc, Wiesbaden, Germany) (7×10^4 cells in 1 mL of growth medium) to easily observe the cells during and immediatly following treatment. Cells were then incubated at 37°C under 5% CO_2 for 2 hrs. during which they adhered to the bottom of the chamber but retained roughly spherical shape. After 2 hrs., the growth medium was removed and replaced with low-conductivity, isoosmotic (292 mOsm/kg) potassium phosphate electroporation buffer (KPB: 10 mM KH_2PO_4/K_2HPO_4 in a ratio of 40.5:9.5, 1 mM $MgCl_2$, and 250 mM sucrose; pH = 7.2; electrical conductivity of 0.16 S/m) at 25°C containing 0.15 mg/mL propidium iodide (PI) (Life Technologies, Carlsbad, USA). As KPB is approximately 10-fold less conductive than the growth medium, it was used to reduce the electrical current and minimize the effects of Joule heating on the cells during PEF treatment.

3.2.2 Electrode Design and Numerical Modeling of Electric Field Distribution and Thermal Considerations

Two parallel Pt/Ir alloy (90:10) wire electrodes (0.8 mm diameter wires spaced 4 mm edge-to-edge) were inserted into the Lab-Tek II chamber seeded with cells (as described) on the bottom of the glass surface. With the goal of tightly controlling the electric field to which the cells were exposed, the electric field distribution between the electrodes was simulated numerically in COMSOL Multiphysics (Version 5.1, COMSOL, Burlington, MA) using the electrostatics module. The numerical calculations showed that the cells centered between the electrodes (which were monitored in the experiments) experience practically homogeneous electric field. The electric field was simulated using a 1 V test pulse (2.2 V/cm along the midline between the electrodes) to give the normalized distribution of the electric field as a result of the applied potential (Fig. 3.1, center and right panels).

The energy delivered during electroporation treatment was approximated in a manner similar to

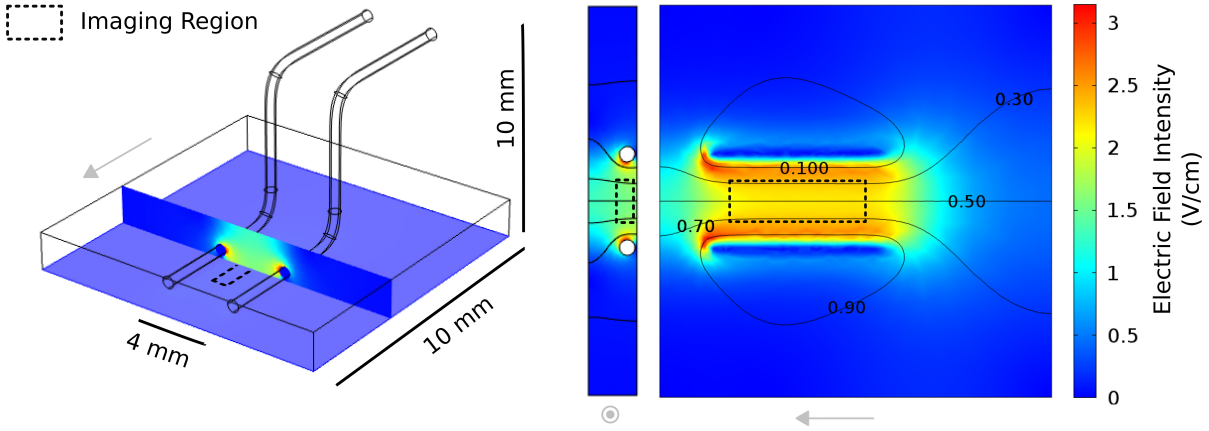

Figure 3.1: Cells were exposed to electric field pulse trains using a pair of electrodes to generate a homogeneous electric field between the electrodes. From left to right: the entire electrode setup with a vertical slice showing the electric field distribution on that plane; the vertical slice from the left pane expanded; and the electric field distribution 5 μm above the bottom surface of the chamber shown in the horizontal slice in the left pane. *In vitro* application of electric fields was performed in glass-bottom chambers with Pt/Ir electrodes submerged in low-conductivity KPB pulsing medium. The electric field shown was modeled at steady state and with a voltage of 1.0 V applied to produce a relatively homogenous electric field ($\pm$3.5% variation in intensity between the electrodes). The isopotential contours and the colormap indicates the distribution of the electric field within the imaging chamber and the dotted line indicates the region from which images were obtained. The gray arrows all point in the same direction to indicate the orientation each image.

[224] with several caveats. Assuming the load may be modeled as having parallel resistive and capacitive components, $R(t)$ and $C(t)$, leading to resistive current $I_R(t)$ and capacitive current $I_C(t)$, respectively. Assuming that the resistance of the medium is constant $R(t) = R$ and ideal pulses are delivered (i.e. each pulse starts and ends as $V_0 = V_f = 0$), the capacitive current disappears, giving

$$\begin{aligned} E = \int_0^{\tau_{on}} V(t)\big(I_R(t) + I_C(t)\big)dt &= \int_0^{\tau_{on}} \left(\frac{V^2(t)}{R(t)} + V(t)C(t)\frac{dV}{dt}\right)dt \\ &\approx \sum_{i=1}^{N} \frac{V_i^2}{R}\tau_i = \frac{V^2}{R}\tau_{on}, \end{aligned} \tag{3.1}$$

where $\tau_{on} = \sum \tau_i$ is the total energized time of the electrodes during the treatment scheme, N is the total number of pulses in either polarity, τ_i is the pulse width of each pulse, and V is the steady-state amplitude of the pulse. Each of the treatments were designed to have equivalent τ_{on} and the

applied potentials $|V_{hi}|$ in treatments B, C, and D were equivalent (500 V). Estimating the total energy delivered for treatments B, C, and D, $V_{hi}^2 \tau_{on}$ is considered constant and, if the resistance is also considered constant and estimated from V-I measurements as $R \approx 150\ \Omega$, similar applied energies were used for each treatments B, C, and D, with treatment A having a slightly lower applied energy due to the lower potential. The estimated energy dosage delivered during treatment A is estimated to be 0.12 J and 0.33 J for treatments B, C, and D. These estimates are corroborated by the measured potentials (Fig. 3.2). To estimate the worst-case Joule heating experienced by the cells during treatments B, C, and D, we assume that the energy delivered to the cells over the course of the treatment was immediately and entirely converted to heat to induce an instantaneous temperature rise as [225]

$$\Delta T = \frac{|V|^2 \sigma}{d^2 c_p \rho} \tau_{on} \tag{3.2}$$

where V is the amplitude of the voltage applied between the two electrodes, σ is the conductivity of the medium d is the distance separating the two electrodes, and c_p and ρ are the heat capacity and density of the medium, respectively. Assuming the properties of the medium are approximately that of water with altered conductivity ($c_p = 4200$ J/(kg·K); $\rho = 1000$ kg/m^3; $d = 0.004$ m; $\sigma = 0.16$ S/m; $\tau_{on} = 0.02$ s), we calculate that the worst-case temperature increase would be 11.9°C for treatments B, C, and D. This increase would result in an increase from 25°C to 37°C, which is approximately within the normal physiological temperature range. Furthermore, when Joule heating was considered in the finite element model of the electrodes (results not shown), the temperature increase of the portion of the chamber in which the cells were observed was calculated to be less than 10°C for treatments B, C, and D and less than 4°C for treatment A.

3.2.3 Microscopy & Fluorescent Staining

Imaging was performed using an inverted fluorescence microscope (AxioVert 200, Zeiss, Oberkochen, Germany) with a 100x oil immersion objective ($NA = 1.4$). To monitor PI uptake, the cells were

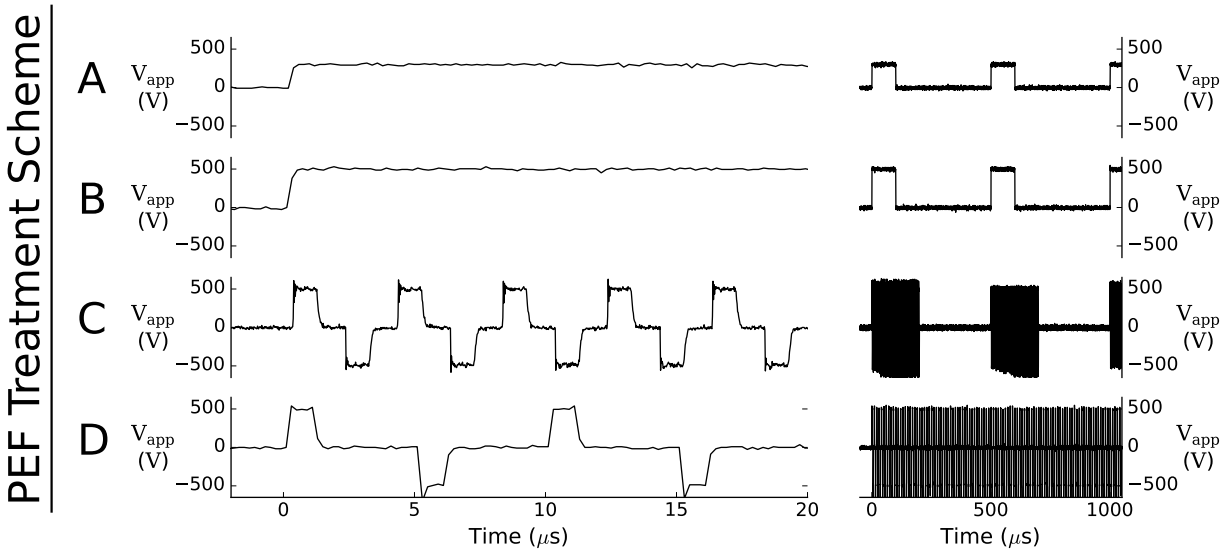

Figure 3.2: Pulsed electric fields (PEFs) were applied using several schemes. Each treatment scheme is shown listed a single row. The left plot in each row shows both voltage V_{app} trace for the first 20 μs of the applied pulse train. The right plot shows two characteristic periods of each pulsing scheme. Each treatment was performed as follows: **A**.) 200 monopolar pulses of 100 μs in length and 300 V amplitude; **B**.) 200 monopolar pulses of 100 μs in length and 500 V amplitude; **C**.) 200 bursts of containing 50 pulses each (10,000 total pulses) of alternating polarity at 500 V absolute amplitude with 1 μs delay between each pulse; **D**.) 200 bursts containing 50 pulses each (1×10^4 total pulses) of alternating polarity at 500 V absolute amplitude with 4 μs delay between each pulse to create a continuous pulse train across the whole treatment duration. 200 periods of length 500 μs comprised each treatment scheme to conserve equivalent total treatment time across all treatments (100 ms).

illuminated using a monochromator set to an excitation wavelength of 490 nm (Polychrome IV, T.I.L.L. Photonics, Munich, Germany) and the emitted PI fluorescence was detected through a 605 nm bandpass filter (605/55 nm Chroma, Rockingham, VT) and a cooled CCD camera (Visi-Cam 1280, Visitron Systems, Puchheim, Germany) as previously described [65]. Fluorescence images (12-bit) were captured using MetaMorph 7.7.5 software (Molecular Devices, Downingtown, PA). Control images were obtained immediately prior to PEF treatment.

3.2.4 Time Series Images & Pulse Parameters

Time-series images were obtained by synchronizing a laboratory prototype H-bridge-based pulse generator (University of Ljubljana) with the image acquisition software using a 3 ms logical trigger pulse (5 V) from the computer controlling the image acquisition to the input trigger on the pulse generator. The triggering delay between the rising edge of the trigger pulse and the beginning of the pulsing protocol was 200 ns. Pulses were applied as described above and imaging was performed at a rate of 5 Hz with the first frame being synchronized with the beginning of the pulse treatment. Oscilloscope recordings (Wavepro 7300A, LeCroy, USA) of the applied voltage V_{app} using a high voltage probe (ADP305, LeCroy) from each treatment are shown in Fig. 3.2. Specifically, treatment A is a train of 200 positive-polarity pulses of 300 V amplitude, each lasting 100 μs and repeated at a rate of 2 kHz (repetition period of 500 μs). Treatment B is exactly the same as treatment A, except with a pulse amplitude of 500 V. Treatment C composed of 200 $\times$ 500 μs periods containing 50 alternating positive and negative pulses of 1 μs duration and 500 V, separated by a 1 μs delay between each pulse, and the whole burst followed by a 300 μs delay before the beginning of the next burst (20,000 total pulses). Treatment D is a series of $20,000 \times$ 1 μs alternating bipolar pulses of 500 V with a delay of 4 μs between each pulse. Each treatment consisted of 200 periods ($N = 200$) lasting 500 μs each ($T = 500$ μs), for a total treatment time of exactly 100 ms for each pulsing scheme ($N \times T = 100$ ms).

3.2.5 Determination of Cell Electroporation Threshold

Measurements were obtained from images captured three minutes post-treatment from cells treated with PEFs composed of waveforms similar to those appearing in treatments A & B, C, and D with varying amplitudes from 0 to 500 V, corresponding to electric field intensities of $0 - 1250$ V/cm ($\pm 3.5\%$, depending on cells' precise location between the two electrodes). Cells were stained with PI in the same manner as described above. To generate the electroporation threshold curves in Fig. 3.3, the ratio of cells containing detectable levels of PI to total cells was calculated and plotted.

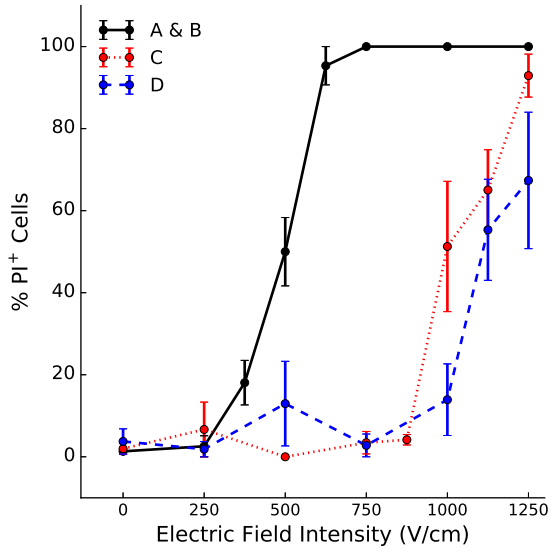

Figure 3.3: Cells exposed to PEF treatments of high-frequency bipolar pulses become similarly electroporated to cells exposed to longer monopolar pulses, though at higher electric field intensities. Fluorescent images were thresholded at 1% of the camera's dynamic range and overlaid on corresponding bright field images prior to counting. If a cell contained any fluorescence above the threshold value, it was considered electroporated.

3.2.6 Image Processing

Image processing was performed using ImageJ (2.0.0) (U. S. National Institutes of Health, Bethesda, MD) and Python 3.5.1. For the time series data, images were thresholded by intensity at 0.5% of the total dynamic range of the 12-bit camera used. Within each image, a rectangular region of interest was identified around the fluorescent polar regions of the cell and the arc lengths. The corresponding arc angles within these regions were calculated using additional information from bright field images taken prior to electroporation to estimate the radii of the spheroidal cells (Fig. 3.4). The fluorescence intensity at the anodic and cathodic poles along the cell membrane were determined by averaging 10 pixels along the radial direction for each pixel around the cell membrane to estimate the circumferential fluorescence intensity profile. The fluorescence intensity at the cell poles is reported as the average intensity of the circumferential between $\pm 5^\circ$ of the pole (90° for the cathode and 270° for the anode) normalized to the background. To quantify the anodic-cathodic crescent asymmetry, two-sample z-tests were performed for each treatment group for the cathodic and anodic electroporated arc lengths and average fluorescence intensities.

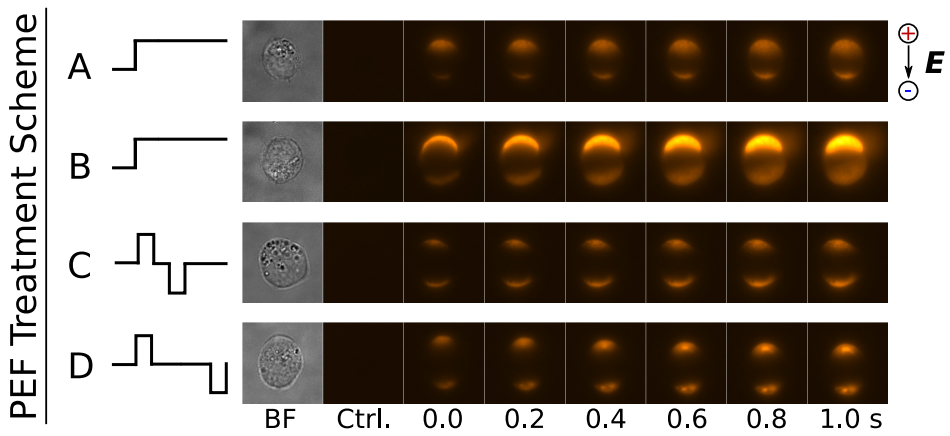

Figure 3.4: Propidium fluorescence rapidly increases asymmetrically at the electropermeablized cellular poles for long monopolar pulses and symmetrically for equivalent energy short, bipolar pulses. Images of cells are plotted every 200 ms during and post-treatment for pulsing scheme. The anode is located at the top of each image and the cathode at the bottom, as indicated by the legend to the right of the images. Cell images are representative of typical observations for each PEF treatment scheme.

3.2.7 Propidium Uptake Calculation

The Nernst-Planck equation describes the conservation of mass in an electro-diffusion system, and has historically been used to model the mass transport in electroporated cells [80, 85, 156]. In the case of a cell in a media-filled well, the fluid is stationary $|\mathbf{u}| = 0$. Additionally, over the time-scales observed, the image exposure time was 2 times greater than the total duration of the electrical pulses, which only took place during the first imaging frame. Therefore, the applied electric field is not present in the subsequent frames ($|\mathbf{E}| = 0$) and the potential-dependent term disappears. These simplifications leave the purely diffusive Fick's law $\mathbf{J} = -D_c \nabla c$ as the principle equation governing the molecular transport during the post-pulsing imaging sequences where c and D_c are the concentration of and diffusivity of PI, respectivtly and $\mathbf{J}$ is the flux vector. Assuming that there exists an ample concentration of PI in the cell exterior such that the concentration anywhere outside the cell along the radial direction is the same,

$$J_r = \frac{V}{A}\frac{\partial c}{\partial t} = -D_c \frac{\partial c}{\partial r} \tag{3.3}$$

where A is the surface area of the cell membrane and V is the volume of the cell. The radial derivative in Eq. 3.3 can be discretized using $\partial c/\partial r \approx (c_{out} - c)/d_m$ and the whole equation may then be rewritten in terms of the net permeability P_m of the membrane along the outward radial direction as [85]

$$\frac{dc}{dt} = P_m(c_{out} - c), \tag{3.4}$$

$$P_m \approx D_c A/(V d_m) \tag{3.5}$$

where d_m is the thickness of the cell membrane. It has been shown that there exists a linear relationship between average fluorescence intensity I and concentration c of bound fluorescent PI at concentrations on the order of those in the experimental setup herein [81, 146, 156]. Representing this relationship as $c = \alpha I$ with proportionality constant α, and substituting this expression into Eq. 3.4, an expression may be found that approximates the effective membrane permeability by the equation

$$\begin{aligned} P_m &= \left(\frac{1}{\alpha I_{sat} - \alpha I}\right)\frac{d(\alpha I)}{dt}, \\ &= \left(\frac{1}{I_{sat} - I}\right)\frac{dI}{dt}, \end{aligned} \tag{3.6}$$

where I_{sat} is the average fluorescence intensity of the cell at saturation. Fig. 3.7 shows the intensity of an average cell exposed to PEF treatments A, B, C, and D. In each frame (5 Hz image acquisition rate), the average fluorescence intensity of the cell is shown on the left panel. The change in intensity over time is shown in the middle panel and indicates that the fluorescence intensity reached a maximum for cells exposed to treatment A before decaying. Using the data from treatment B to determine the saturation concentration of PI (i.e. the fluorescence intensity at $t = 10$ s) the permeability of the membrane may be determined for the remaining treatments: A, C, and D (right panel of Fig. 3.7). The right panel shows the permeabilization of each cell calculated using Eq. 3.6. The trace for treatment B introduces a singularity in the permeabilization plot because the

denominator becomes zero when the fluorescence intensity is at a maximum. This is not the case for treatments A, C, and D because they are less permeabilized and therefore are evaluated in this manner.

3.3 Results

3.3.1 Short Bipolar PEFs Require Higher Amplitudes to Obtain Detectable Cell Permeabilization Compared to Long Monopolar PEFs

In cell populations exposed to the long, monopolar pulses in PEF treatments A and B (indicated as A & B), we detected intracellular PI at electric field intensities approximately 500 V/cm lower than in populations exposed to the bursts and continuous applications of short, bipolar pulses in PEF treatments C and D, respectively. For waveforms A & B, cell permeabilization is detected above 250 V/cm, at least 20% of the cell population is repeatably permeabilized, with the fraction of permeable cells increasing steeply until saturation at approximately 600 V/cm, where 100% of the population of cells is permeabilized as determined by measurable concentrations of PI (Fig. 3.3). Waveforms C an D require higher amplitude electric fields to permeabilize cells, whereby membrane permeabilization by PI can be detected above 900 to 1250 V/cm. However, little difference exists in the permeabilized population between C and D waveforms, with only marginally lower thresholds exhibited for the bipolar bursts in waveform C. Due to the limitations of the pulse generator, 500 V (corresponding to an electric field intensity of 1250 V/cm) was the maximum amplitude tested experimentally, which was slightly too low to achieve complete permeabilization in the case of treatments C and D.

3.3.2 Bipolar Bursts of PEFs Generate Shorter, Less Permeabilized Regions on the Cell Membrane than Monopolar PEFs

Spatially and temporally resolved PI uptake into single cells was observed *in vitro* and quantified using images obtained during and immediately following PEF treatment (Fig. 3.4). The results indicate that the electroporated region of the cell membrane allowing PI transport is smaller for treatments C and D than for treatments A and B. These crescent-shaped regions correspond to regions on the cell membrane that have exceeded the transmembrane potential threshold and become electroporated or exhibit increased permeability. For all tested waveforms, PI uptake was detected only across membrane regions facing the anode (positive electrode) and cathode (negative electrode). As known from previous studies, the regions of the cell membrane allowing PI transport correspond to regions of the membrane that have become destabilized and allow molecular exchange between the intracellular and extracellular environments. For monopolar waveforms A and B, the arc length of the detected permeabilized membrane region was significantly ($p < 0.0001$) larger on the anodic side compared to the cathodic side, with waveform B resulting in larger permeabilized region than treatment A (Fig. 3.5). Both observations are consistent with previous reports [81, 168, 226]. Waveform C resulted in equal arc lengths corresponding to the permeabilized membrane regions on both sides of the membrane, whereas waveform D resulted in larger arc lengths on the anodic side, but at a lower significance level ($p = 0.0454 < 0.05$), with both waveforms C and D resulting in about 50% less PI uptake at the same amplitude and treatment time as treatments A and D (Fig. 3.5). This trend is evident in Fig. 3.5, by the significantly lowered cathodic electroporated regions in treatments C and D compared to those in treatment A and B. The much greater time rate of intensity change in Fig. 3.6 also indicates less surface area of the membrane is electroporated and within this area, the transport of PI is reduced by 50% in treatment C, compared to treatments A and B. Significant changes in the cell's spherical shape were not apparent during the observation period with an average change in radius elicited in cells by treatment A of $-4.25 \pm 2.10\%$ ($n = 16$), by treatment B of $-6.84 \pm 1.91\%$ ($n = 15$), by treatment

C of $5.62 \pm 0.61\%$ ($n = 22$). and by treatment D of $5.83 \pm 0.53\%$ ($n = 18$). The change in radius of the untreated cells was $2.27 \pm 0.93\%$ ($n = 7$; mean $\pm$ standard error).

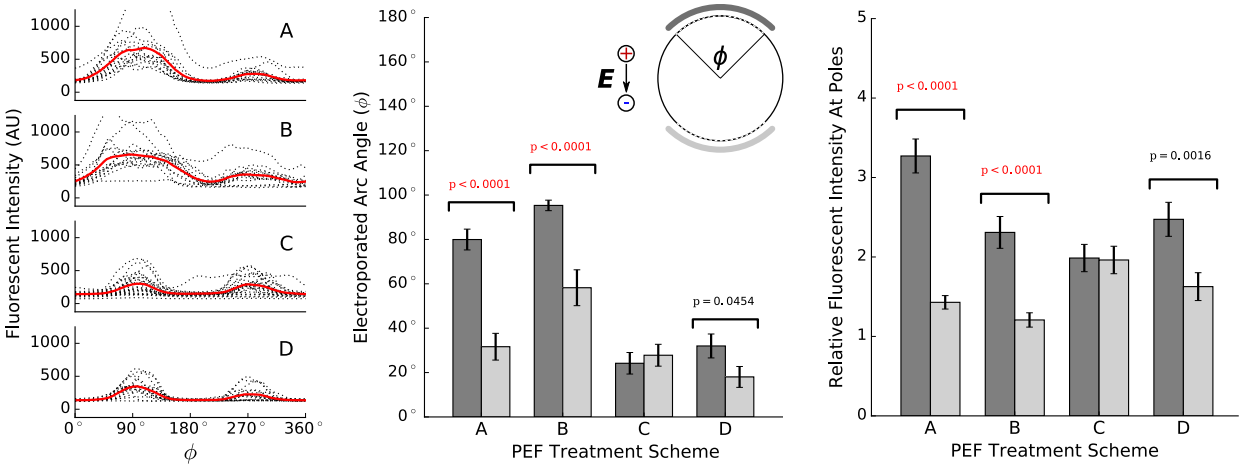

Figure 3.5: The spatial extent and degree of the electroporation cap are skewed in the direction of the cathode during long monopolar pulsing whereas for short bipolar pulses show more symmetric electroporated caps. fluorescence intensity values were quantified around the circumference of each cell and plotted for each treatment (dotted black lines) and the average for each treatment group (solid red line) (left panel). electroporated caps were identified as regions along the cell membrane exhibiting fluorescence intensity more than 0.5% of the total dynamic range of the camera with exposure of 100 ms beginning immediately following pulse treatment (middle panel). The angle ϕ is the arc angle on which 2-dimensional arc length projection lies. The fluorescence intensity average over 10° centered on the cathode and anode are shown (right panel). Statistics presented are the result of a two-sample z-test performed to compare the anodic (*dark gray*) and cathodic (*light gray*) arc lengths.

3.3.3 Membrane Resealing and Concentration Gradients Compete to Limit PI Influx

PI flux into an electroporated cell is ultimately limited by two competing mechanisms: concentration gradients and membrane resealing (Eq. 3.4). Fig. 3.6 shows how the fluorescence intensity time derivative along a cell's anode-to-cathode diameter (parallel to the electric field) changes over time, normalized to the cell radius. In order to become maximally fluorescent, PI must enter the cell and bind to nucleic acids. It was observed that the binding process is sufficiently rapid and occurs within microseconds of the PI entering the cell [156]. While small portions of the fluorescent

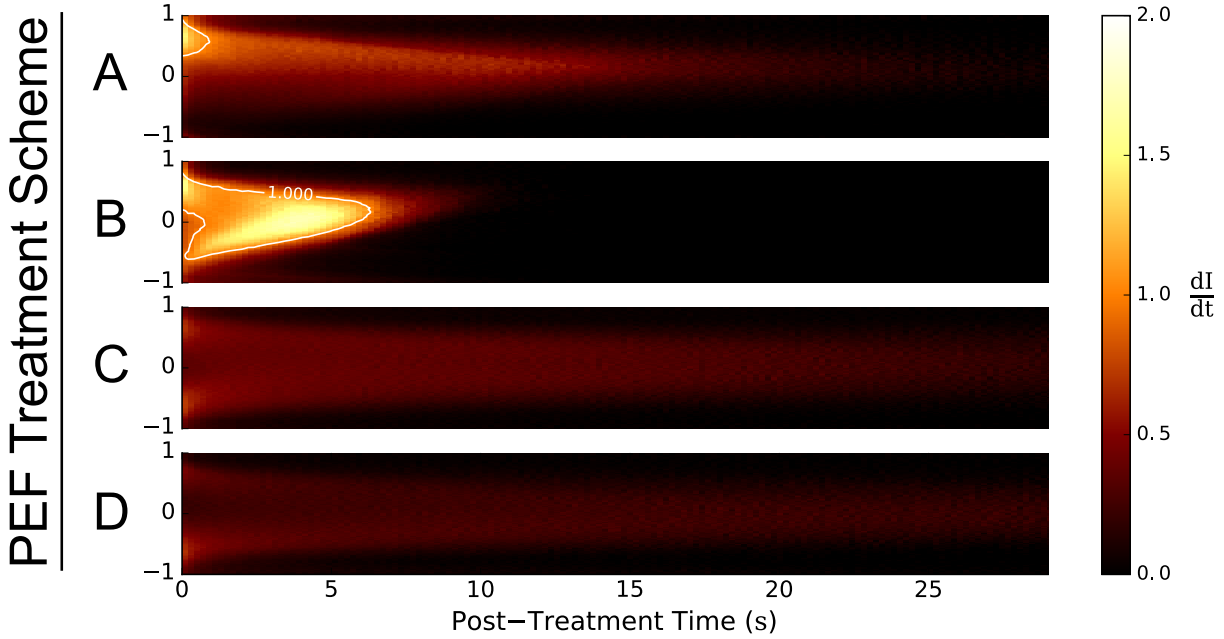

Figure 3.6: Propidium flux magnitude along the normalized cellular diameter is rapid and asymmetric for long monopolar pulses while elongated and symmetric for rapid bipolar pulsing schemes. The relative change in propidium fluorescence with respect to time is calculated every 200 μs and plotted along a normalized cellular diameter where 1 and -1 correspond to the cathode-facing and anode-facing hemispheres, respectively. The time derivative is given in units of AU/s (arbitrary units per second) and where $dI/dt > 1$ is the region inside the white contour and $dI/dt < 1$ outside.

region in some cells reach values near the saturation intensity of the camera sensor, the whole-cell fluorescence measurements are an average over the entire cell and plateau at a value roughly 75% of the maximum 12-bit camera sensor value (i.e. 4095). Therefore, the average fluorescence intensity changes within the cell are directly proportional to the PI that has entered the cell. Fig. 3.6 shows how the change in fluorescence intensity at the two cell poles is rapid at time $t \approx 0$, corresponding to the initial rapid entry of the PI into the cell unilaterally across all treatments. However, differences quickly arise when the evolution of the intensity change profile is observed between each PEF treatment. Treatments A, C, and D indicate that an initial rapid influx of PI occurs at the cell poles followed by a long, gradual decay, though the values are always positive. The asymmetries observed between the PI uptake at the cells' anodic and cathodic poles in treat-

ment A are recapitulated in the temporal-spatial evolution profiles in Fig. 3.6. Following treatment B, however, the change in PI intensity reaches steady state for $t > 10$ s, indicating that the membrane permeability has saturated the nucleic acid binding sites state relatively quickly. Treatments C and D of equivalent amplitude never reach this equilibrated state within the observation period (30 s post-treatment). In treatment A, the membrane never reaches the same permeabilized state as in treatment B to allow similar concentrations of intracellular PI. Because treatment B reaches equilibrium much faster than treatments A, C, and D and in each trial, the cell was exposed to the same concentration of extracellular PI, membrane permeability is the effect in treatments A, C, and D that largely limits the observed PI uptake for PEF treatments prior to reaching diffusive equilibrium.

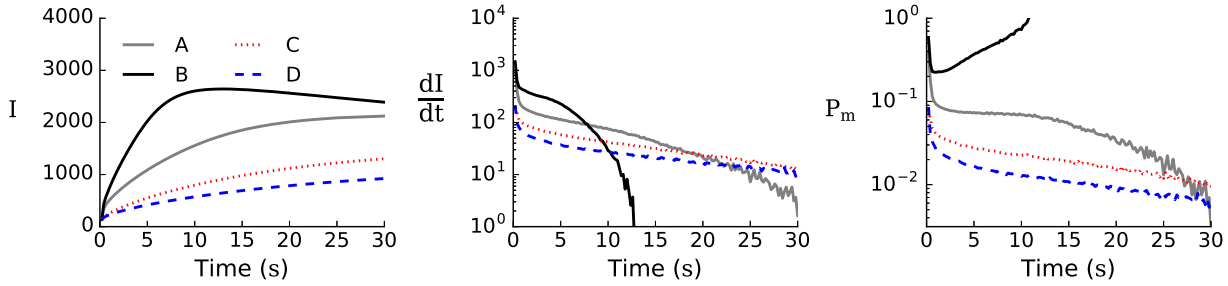

Figure 3.7: The permeability induced by long, monopolar PEF treatments A and B induce significantly greater membrane permeability than short bipolar treatments C and D. The evolution of the average fluorescence intensity of the cells over time is plotted for treatments A, B, C, and D (*left*). The evolution of the change in fluorescence intensity over time is plotted for each of the treatments (*center*). Knowing the evolution of fluorescence intensity and its first derivative with respect to time enables the calculation of membrane permeability P_m using Eq. 3.4 (*right*). If, as in the case of the treatment B, the propidium concentration ceases to change while $P_m \neq 0$, as evidenced by the continued change in the other treatment plots in Fig. 3.6, diffusive equilibrium has been established quickly. This enables the calculation of the maximum saturation intensity I_0 used in Eq. 3.4 to calculate the permeability of the other treatments. Fluorescence intensity measurements I are given in arbitrary units and permeability P_m is given in AU/s (arbitrary units per second). The effective permeability generated by treatment B reaches equilibrium quickly and creates the singularity in the P_m profile in the third panel, as the equilibrium fluorescent value induced by treatment B was used in the calculation of the other profiles using Eq. 3.6.

3.4 Discussion

3.4.1 Higher Amplitude is Required for Short Bipolar PEFs to Achieve Similar Permeabilized Region Sizes and Degrees as Longer Monopolar PEFs

The degree of permeabilization and surface area of the permeabilized membrane region both depend on PEF parameters used. Here, we show that PEF treatments consisting of trains of bipolar pulses on the order of 1 μs require much greater amplitudes to generate similar levels of electroporation compared to those observed in longer pulse width monopolar PEFs (Fig. 3.3), for equivalent total treatment times. As determined through PI transport, these permeabilized regions appear similarly fluorescent to cells exposed to monopolar PEFs on the order of 100 μs (treatments A and B; Figs. 3.5). Further, in treatments A and B, (delays of 400 μs between pulses), and treatment D (delays of 4 μs between pulses), cells exhibited greater permeability on the cathode-facing cell region than the anode-facing region ($p = 0.01$). The span of the permeabilized region, in addition to the the degree of permeabilization, is varied between short bipolar pulses and longer monopolar pulses and increases the net PI uptake observed *in vitro*. Treatment C, however induced similar degrees of permeabilization within similarly-sized regions at both poles, indicating that the mechanisms driving PI uptake occur on the time scale of ~ 1 μs.

The decreased permeabilization observed following short bipolar PEFs, despite equivalent-amplitude and equivalent treatment times, has been largely attributed to two biophysical mechanisms: incomplete charging and assisted discharge. The characteristic charging time of the cell membrane is on the order of 1 μs [227], which is two orders of magnitude smaller than the pulse width of PEFs typically used in ECT, GET, and traditional IRE. Low-conductivity extracellular medium used in *in vitro* studies to limit heating by minimizing the current flow further lengthens the charging time of the membrane. When the pulse width of the applied electric field approaches the charging time of the membrane, a significantly reduced induced transmembrane potential (Fig. 3.8; calculation

performed as in [167], using the conductivity of the low-conductivity buffer given in Section 3.2.1). Low-conductivity extracellular medium typically used in *in vitro* studies to limit heating by minimizing the current flow may lengthen the membrane charging time further. If the transmembrane potential is unable to reach the same amplitude attained by short bipolar pulses as it does when longer monopolar pulses are applied, the probability of membrane permeabilization decreases.

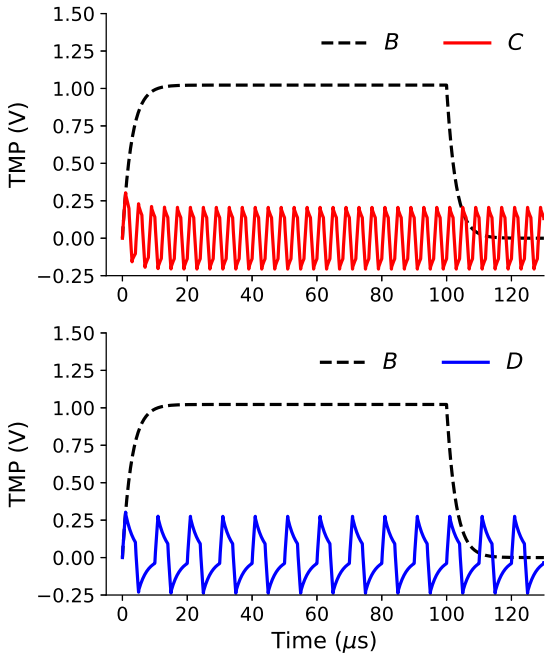

Figure 3.8: The transmembrane potential φ for short bipolar PEFs are unable to achieve the same amplitudes as longer monopolar pulses in low-conductivity medium. The calculation is based on the Laplace transform to determine the transient response of a cell in the presence of PEF treatments with equivalent-amplitude pulsing schemes B, C, and D with rise times of 20 ns.

For such short bipolar pulses, a pulse cancellation or healing mechanism has also been proposed to account for decreased PI uptake for pulses of nanosecond pulse widths (nsPEFs). While not yet rigorously explained, the second square nsPEF pulse following an initial nsPEF pulse of opposite polarity has been observed to negate a portion of the membrane restructuring induced by the first pulse [138, 228]. When the delay between the first and second pulse is increased, the cancellation effect is mitigated, as if two pulses were delivered independently [229]. This cancellation mechanism could explain the greater electroporation voltage threshold (Fig. 3.3) in addition to the asymmetries between treatments A and B. (Fig. 3.5). The alternating polarity, pulse width, and intra-pulse delay on the order of the membrane charging time could account for the symmetry in electroporated region observed in treatment C: both sides of the membrane become similarly permeabilized because the differences induced on any particular side by one pulse are quickly mitigated and/or balanced by a second pulse of opposite polarity.

3.4.2 Propidium Ions Continue to Enter the Cell Long After Completion of PEF Treatment

The presence of fluorescence signal indicates that the cell membrane remains permeabilized long after the conclusion of the applied electric field (Fig. 3.5). If electrophoresis is the dominant mechanism for propidium ion influx, the electrophoretic force acting on the propidium ions is necessarily parallel to the electric field [80, 81]. The ions would enter the cell from only one of the poles, depending on their charge and the directionality of the electric field. In this case, it is possible that the electrophoretically-driven propidium ion flux would force concentrations of propidium ions into the cell membrane beyond the concentration of binding sites available. Upon removal of the electric field, intracellular diffusion would slowly allow binding of the remaining propidium ions until the binding sites are saturated with propidium ions throughout the cell, even if the membrane quickly reseals [80]. The presence of fluorescence signal in both regions following completion of monopolar PEF treatments A and B indicates that propidium ions are able to diffuse throughout the unsaturated binding sites on the cellular interior. If the permeability of the cell membrane is sufficiently large as to allow diffusive equilibration and subsequent binding-site saturation, as in the case of cells exposed to PEF treatment B, the cell's fluorescence intensity plateaus quickly and it becomes difficult to visualize changes in a cell's net permeabilization. In this case, all of the propidium ion binding sites are occupied and the fluorescence intensity will not increase further. Fig. 3.5 indicate that the cells exposed to treatment A (long monopolar PEFs) have a larger membrane areas that are permeabilized to a greater degree than for treatments C and D. With 60% lower amplitude, treatment A is able to generate a two-fold increase in effective permeability over treatments C and D (Fig. 3.3), which generate similar permeability states (Fig. 3.5).

Spatial observations of the regions of increased permeability *in vitro* are also important for a computational model seeking to accurately describe electroporation. The electroporated membrane regions around a spherical cell must be finite for a molecule of a specific size. If a molecule is typically unable to pass through the membrane, and only through portion does transport occur,

and in agreement with previous literature, the permeabilized region of the membrane is finite and dependent on the pulse parameters chosen for a given PEF treatment [85]. Though treatments A and B elicited significantly larger electroporated regions than treatments C and D (Fig. 3.5), the fluorescent regions of the cells in Fig. 3.4 are discrete and considered the only portions of the membrane to allow transmembrane transport of propidium ions [85]. The presence or absence of asymmetry in electroporated arc length has been shown to depend on the waveform of the applied electric field. For treatments comprised of long-duration monopolar pulses (100 ms), longer than those in as treatments A and B (100 μs), asymmetrical uptake of PI has been observed [81] and this effect has been replicated here with the intensity (Fig. 3.5) and time change of intensity on the cathodic and anodic hemispheres of the cells observed (Fig. 3.6).

3.4.3 Objective Analysis of Different Electroporation Protocols May Be Performed Using Permeability Estimates

When PI binds to nucleic acids, it undergoes a dramatic fluorescence increase, making it useful in assays for evaluating membrane integrity, such as cell death [195] or membrane permeabilization [81, 226], which rely on a binary result. Continuous measurements have been performed [146] using chemical agents to calibrate fluorescence intensity measurements, though they have not been used to study the temporal evolution of membrane permeability induced by electric fields with pulse widths on the order of the characteristic membrane charging time. Fig. 3.6 and Fig. 3.7 show that the fluorescence change over time has ceased and the average fluorescence intensity has plateaued at $t \approx 10$ s, indicating that the PI binding reached a maximum. By quantifying the cell membrane's permeability, it may be possible to objectively evaluate treatments with radically different pulse parameters by comparing the effective permeability—and therefore potential molecular transport—induced by different PEF treatments. Electroporation pulse parameters of different timescales, different amplitudes, and different waveforms may be analyzed by evaluating the permeabilization they induce. Indeed, two arbitrary sets of pulse parameters may be

theoretically evaluated for clinical treatment using the membrane permeabilization as an objective measurement for the efficacy of the treatment.

Complicated by the binding kinetics that generate the observed PI-based fluorescence, the ultimate fluorescence value at each point depends on the concentration distribution of nucleic acids within the cell. A valid discussion of these results is not complete without a consideration of the limits and drawbacks of this type of analysis. First, the saturation intensity I_{sat} may not correspond to an absolute concentration, but rather serves as a point of comparison between several treatment schemes. Assigning a value of I_{sat} to the maximum intensity observed allows permeability measurements to be evaluated between each treatment. Therefore, it also must be noted that the permeability measures observed are relative to a specific fluorescence value: in this case, the maximum observed in a cell. However, referenced to that point, the relative permeability induced by several different PEF treatment schemes may still be determined.

One particularly apparent drawback of calculating the relative membrane permeability in this manner is apparent in the third panel of Fig. 3.7: the complication that photobleaching could present. Eq. 3.4 indicates that the average intensity at every time point is subtracted from the average maximum intensity at saturation to resolve the calibration curve. When these measurements are close to the maximum average fluorescent value of the saturated cell, the denominator approaches zero ($I_{sat} - I \rightarrow 0$) and the calculation no longer reflects the effective permeability of the cell membrane near this singularity, such as for treatment B in the third panel of Fig. 3.7. In order for Eq. 3.4 to reflect a realistic estimate of the relative permeability of one treatment with respect to a reference, the average fluorescence intensity of the cell I must be sufficiently lower than the reference point I_{sat}.

3.4.4 Clinical Implications for Bursts of Short Bipolar Microsecond Pulsing Schemes

Recently, reports of *in vivo* high-frequency IRE (HF-IRE) treatments have shown that bursts pulses of 1 μs widths and alternating polarities (bursts similar to those in treatment C), applied at a repetition frequency of 1 Hz, could be useful in the clinical setting. These HF-IRE pulses overcome the need for pre-operative neuroparalytic treatment and intra-operative cardiac synchronization when performing IRE treatments [141, 195, 215]. If incomplete charging is the primary mechanism driving decreased cell permeability at similar amplitudes using shorter pulse widths, the lack of muscle contractions observed in HF-IRE could be the result of a similar mechanism. By not sufficiently charging neurons to generate an action potential with a single pulse, then quickly discharging them with an electrical pulse of opposite polarity to exploit an assisted discharge effect, a much greater probability exists that neurons may never reach the necessary voltage threshold for the necessary duration elicit an action potential [230]. Through such a mechanism, cellular electroporation (Fig. 3.4) may still occur, but without the muscle contractions induced by excited nervous tissue.

In overcoming these challenges, HF-IRE has the potential to enable electroporation-based treatments with reduced pain in an out-patient clinical environment. HF-IRE, however, presents the added challenge of rendering the cell membrane significantly less permeabilized (treatments C and D) than the traditional longer monopolar pulses at similar pulse amplitudes and total treatment times (treatments A and B), as observed in Fig. 3.5. It should be noted that the low-conductivity buffer used in this study artificially increases the transmembrane potential rise time by limiting the electrical charge allowed to build on either side of the membrane. In so doing, the system deviates from an *in vivo* scenario with higher-conductivity extracellular media, but may still explain the increased potential threshold requirement for electroporation using HF-IRE over IRE. The results of this *in vitro* study do not exactly mirror an *in vivo* tissue, but instead serve to highlight the differences between different clinically relevant PEF treatment parameters and identify a possible mechanism to explain the differences observed on the cellular level when different pulse parameters are

applied. It must be noted, however, that this study was expressly designed to study electroporation and subsequent transport immediately post-treatment. The viability of cells will decrease following exposure to temperatures in excess of 40°C for extended periods of time [231], whereas the observational period for this study was immediately prior to, during, and post-treatment for 30 s and the temperature increase increased the temperature yet remained within a physiological range ($\Delta T \approx 12$°C from 25°C to 37°C). Therefore long-term thermal damage (i.e. protein denaturation, etc.) affecting cellular viability was not considered in this work.

The practical implication of using HF-IRE treatments over IRE is that greater-intensity electric fields must be applied to offset the decreased transport while retaining the potential utility of HF-IRE treatments. The challenges presented by HF-IRE's shorter pulse widths may be mitigated through using higher pulse amplitudes to maximize the total membrane permeability (Fig. 3.3), while retaining its benefits of overcoming the need for neuroparalytics and generating more homogeneous lesions. The electrical stimulation threshold required to generate action potentials in neurons increases with decreasing pulse widths [230], which allows the short bipolar electrical pulses used in HF-IRE to remain below these thresholds yet sill effectively electroporate cells [141], as demonstrated here. *In silico* modeling of electroporation is particularly useful and may provide a numerical method for further optimizing pulse parameters to achieve similar effectiveness as IRE while retaining the tangible *in vivo* benefits HF-IRE offers for patient care.

3.5 Conclusion

Clinical electrochemotherapy, gene electrotransfer, and irreversible electroporation treatments directly depend on cell membrane permeabilization and consequent transmembrane molecular transport of small molecule drugs to perturb cellular homeostasis. Real-time imaging and subsequent single-cell analysis were performed on cells exposed to pulsed electric fields composed of significantly different pulse parameters and schemes. The effective cellular membrane permeability was calculated using saturated cells to determine the maximum fluorescence intensity of PI-saturated

nucleic acids. Fick's law used to calculate the change in permeability over time for cells treated with each pulsing scheme. Cells treated with short bipolar pulses delivered in bursts of rectangular pulses on the order of 1 μs with a 1 μs inter-pulse delay produce more symmetric permeabilization, in both size and degree, at the extreme cathodic and anodic regions along the cell membrane while exhibiting a higher electroporation threshold. These data were observed through transport and subsequent binding of PI across the cell membrane and suggest that efficient membrane permeabilization may be achieved using high-frequency bipolar bursts of electrical pulses. The permeabilization of cells using HF-IRE may be achieved at the cost of greater electric field amplitudes to overcome the challenges presented by electric fields with pulse-widths on the order of the membrane charging time. These results indicate that HF-IRE type electrical pulses are able to generate similar, though more symmetrical permeabilization, which translates to more predictable cellular response and, therefore, may ultimately result in greater clinical precision when performing IRE, ECT, and GET procedures.

Chapter 4

Characterization of Cell Membrane Permeability *In Vitro* Part I: Transport Behavior Induced by Single-Pulse Electric Fields

Daniel C. Sweeney[a*], James C. Weaver[b], and Rafael V. Davalos[a]

[a] Department of Biomedical Engineering and Mechanics, Virginia Tech, Blacksburg, VA, USA

[b] Harvard-MIT Division of Health Sciences and Technology, Massachusetts Institute of Technology, Cambridge, MA, USA

[*] Corresponding author

Author Contributions

DCS designed and performed the experimental portion of this work, analyzed the results, and wrote and edited the manuscript. JCW and RVD conceived of the research, analyzed the results, and edited the manuscript.

Manuscript in review

4.1 Introduction

Pulsed electric fields (PEFs) are effective in overcoming the transport barrier of the cell membrane by increasing its permeability. A specific motivation for the basic studies reported here is irreversible electroporation, which has been developed with the purpose of directly inducing cell death. It is a non-thermal ablation technique that destabilizes a tissue's constituent cells [16, 59]. Although clinical electroporation treatments are highly effective, the thermal damage associated with long trains of high-strength pulses presents an obstacle to treatment of larger tissue volumes. Furthermore, the inability to measure the degree of cellular damage after treatment has impeded the direct comparison of different PEF application schemes.

Following PEF application, a cell membrane can gradually reseal [87]. The greater the duration of the permeability increase, the less viable the local cell population will become [58, 85]. This loss of viability is attributed to the formation of pores within the cell membrane driven by large transmembrane potentials (TMPs) [14, 67]. Pores decrease the membrane's ability to inhibit the flow of solutes into and out of the cell [111, 148]. The degree to which molecules flow through a membrane following PEF application is often due to the membrane's enhanced diffusive permeability. This quantity is widely used to study membrane dynamics following PEF application [49, 90, 91, 232]. Small-molecule tracers, including propidium (Pro), have been developed to emit a strong fluorescence signal when metabolized or bound to intracellular structures, but are blocked by an intact membrane. Through calibration, such molecules are used to measure molecular flow into cells following PEF application [81, 89, 146, 147]. Measuring the diffusive permeability of a cell has also been proposed as a quantitative method of comparison between different PEF applications [94]. However, such measurements have not been reported beyond recent estimates involving PEFs with thousands of pulses.

Here we quantify the increase in the diffusive permeability of cell membranes following single-pulse PEF application. We show that the permeability of a cell membrane in the minutes following the application of an electrical pulse is a good indicator of the ultimate molecular uptake and that

the cell remains permeable to Pro ions for tens of minutes following PEF application. This is, to our knowledge, the first report to provide a method to quantitatively measure membrane permeability to small molecules using standardized fluorescence microscopy techniques and equipment. We report the first of such measurements from individual cells following the application of a single electrical pulse. We also identify a subpopulation of cells that exhibit a prolonged uptake of Pro at lower strengths and shorter pulse durations than is generally required to elicit a larger, more rapid uptake response. We then hypothesize that there exists a diffusive permeability threshold beyond which the cell is irreversibly permeabilized. Our results further indicate that it may be possible to effectively apply electroporation treatments with a single electrical pulse, resulting in less thermal damage than would be generated by longer pulse trains.

4.2 Materials and Methods

4.2.1 Microfluidic Chamber Design

The geometry of a microfluidic chamber was designed to generate a linear electric field gradient along the length of the chamber (Fig. 4.1a-c) by tapering the channel along its length according to the equation $y(x) = a/(x+b)$ with appropriate boundary conditions ($y(0) = 0.63$ mm and $y(10\text{ mm}) = 0.13$ mm; $a = 1.6$ and $b = 2.5$) [100]. To solve for the electric potential field within the chamber, Poisson's equation was formulated as a boundary value problem with homogenous conductivity in the three-dimensional, source-free chamber interior. A first-order tetrahedral mesh was generated using GMSH (version 2.9.3) [233] for analysis within the FEniCS finite element environment (version 2016.2.0) [234]. Dirichlet boundary conditions were prescribed for the cylindrical regions at either end of the chamber that represent the electrode surfaces inserted into the channel and set to the steady state voltage obtained from the 10, 100, and 1000 μs pulses (Fig. 4.2). No-flux Neumann boundary conditions were prescribed to the exterior boundary of the chamber. The numerical error was calculated under the L^2 norm and the mesh of the chamber iteratively re-

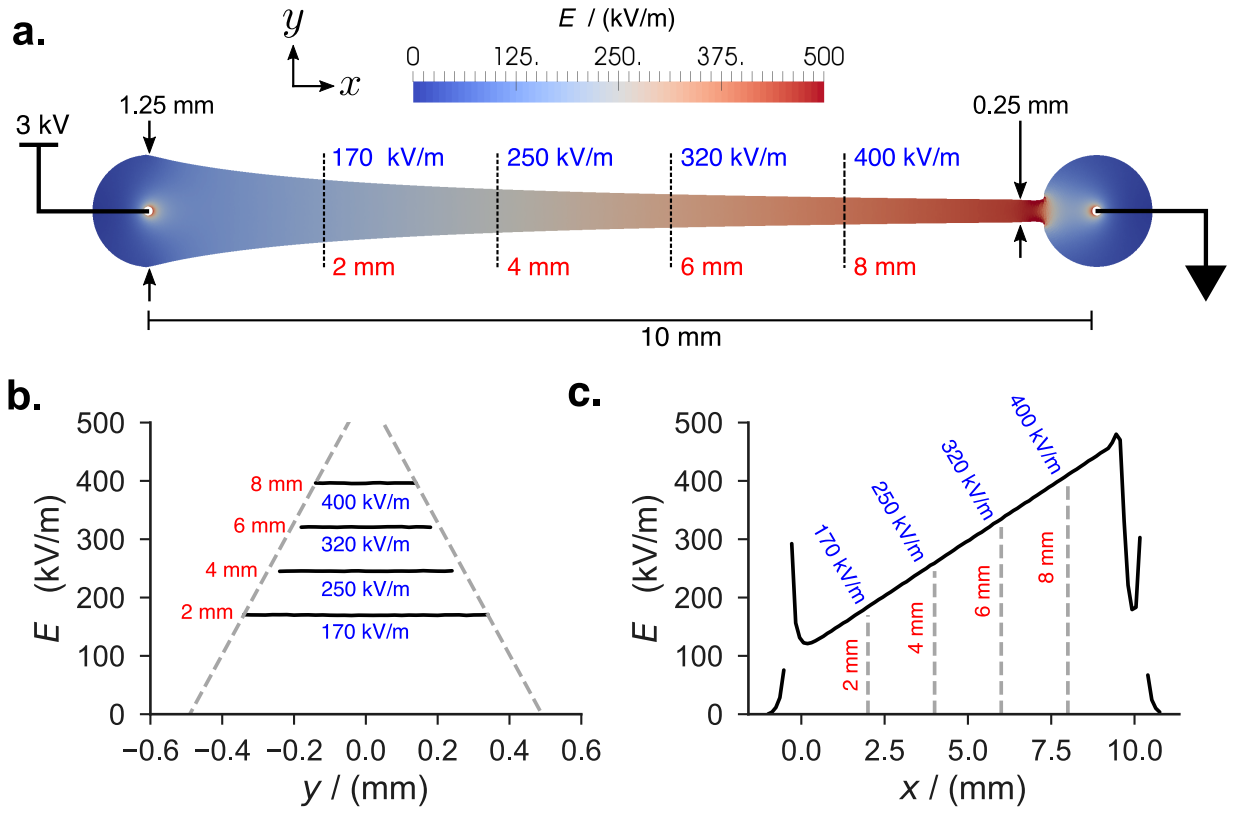

Figure 4.1: Microfluidic chamber for exposing cells to electric fields, E. (a) The electric field strength increases linearly along the axial direction (x-axis) of the tapered microfluidic chamber. Stainless steel electrodes are present at either end of the chamber to generate E during voltage application. (b) E is presented as a function of distance along the vertical axis of the chamber y at 2, 4, 6, and 8 mm along the x-axis. The dotted gray lines indicate the chamber boundaries. (c) E is also presented as a function of the distance along the horizontal axis of the chamber x. The dotted gray lines indicate the positions within the chamber at which the cells were observed.

fined until the relative error between two consecutive solutions was $< 5\%$. The electric field values reported are calculated from the voltage measured at the electrode after the ringing on the rising edge has stabilized (i.e. 170, 250, 320, and 400 kV/m; Fig. 4.5). The same naming convention was followed for the 1 μs pulse for consistency, recognizing that ringing dominates its waveform and is not accurately described by a single value.

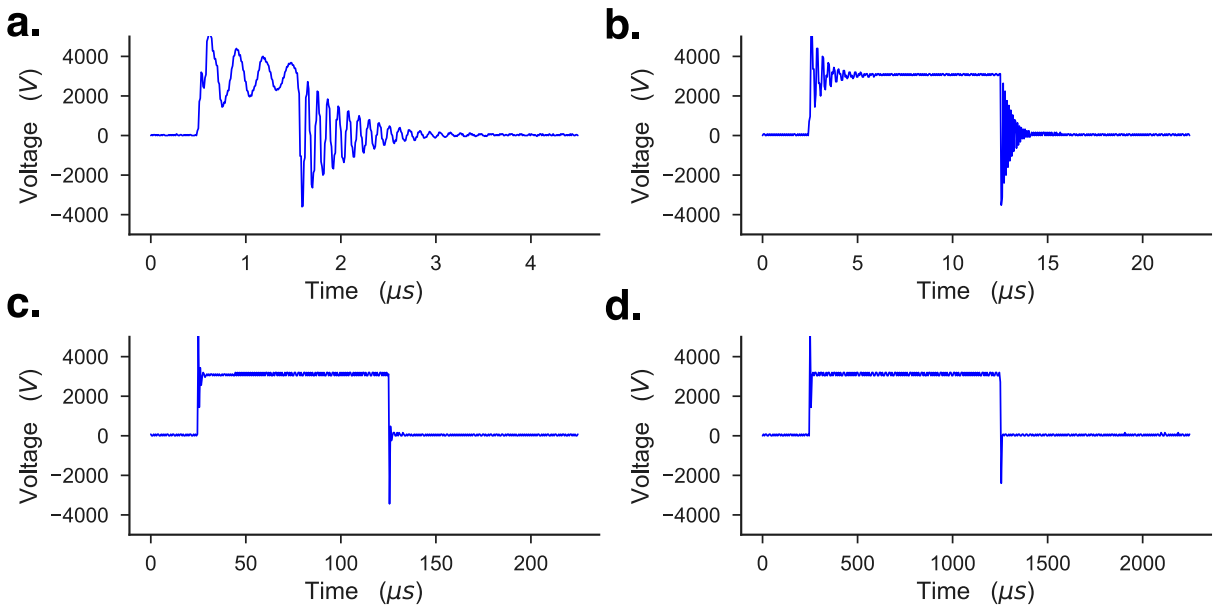

Figure 4.2: An electric potential was applied across the microfluidic chamber through the electrodes at either end at a set potential of 3 kV. The microfluidic chamber contained PBS during these measurements. Ringing on the solid-state half-bridges in the pulse generator generated peaks in the voltage trace lasting between 100-200 ns at peak potentials of approximately 6 kV for each pulse waveform. Though this ringing could induce electroporative effects, these were not considered in the analysis presented here. Accordingly, the pulse widths are referred to as 1 μs (*a*), 10 μs (*b*), 100 μs (*c*), and 1000 μs (*d*) in the present text.

4.2.2 Microfluidic Chamber Fabrication

The physical chamber design was patterned on a silicon wafer using deep reactive ion etching [235], then placed under a vacuum for one hour. Polydimethylsiloxane (PDMS; Sylgard 184, Dow Corning, Midland, MI, USA) was mixed in a ratio of 10:1 monomer to cross-linker, degassed under a vacuum, poured over the silanized negative master mold, and heated at 65°C. After 15 min, the temperature was increased to 100°C for at least an hour before the mold was allowed to cool to room temperature. Once cool, the cured PDMS was removed from the mold and holes were punched in either end of the chamber (Fig. 4.1a) using a 24 AWG biopsy punch (Integra LifeSciences, Plainsboro, NJ, USA) to allow access to the chip interior once assembled. The cured PDMS was then plasma-bonded to a 1 mm thick glass slide that served as the base of the chamber to complete the fabrication process. For confocal imaging, a 0.1 mm thick glass slide was used.

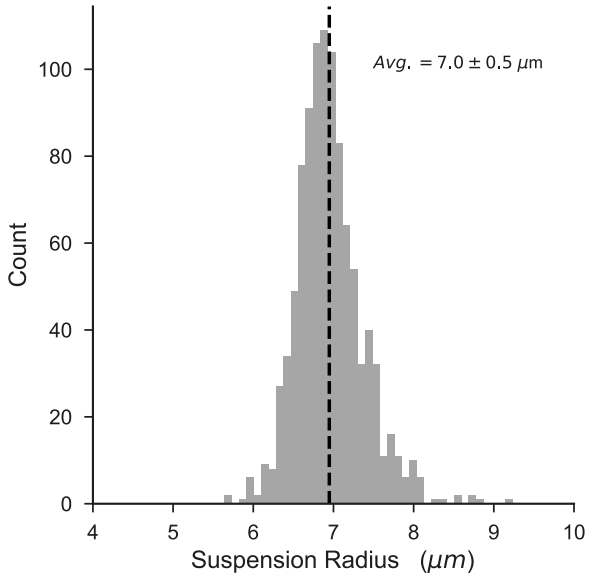

Figure 4.3: The radial distribution of CHO-K1 cells in suspension prior to introduction into the microfluidic chamber. The average radius of CHO-K1 cells suspended in complete F12-K growth medium was 7.0 ± 0.5 μm (dotted line) immediately prior to introduction int the microfluidic chamber ($n = 1000$ cells). Data was obtained using images recorded by a Vi-Cell system, with each image containing an average of 13 ± 6.4 cells. Reported values are given as $mean \pm std$.

4.2.3 Cell Culture and Microfluidic Chamber Seeding

CHO-K1 cells (ATCC, Manassas, VA, USA) were cultured in Ham's F12-K medium (Gibco, Grand Island, NY, USA) supplemented with 10% fetal bovine serum (FBS; Atlanta Biologicals, Flowery Branch, GA, USA) and 1% penicillin/streptomycin (penn/strep; Life Technologies, ThermoFisher Scientific, Waltham, MA, USA). At 70-90% confluence, the cells were trypsinized, counted using a ViCell cell counter (Beckman-Coulter, Indianapolis, IN, USA), resuspended in fresh medium containing 2 drops/ml of NucBlue (Life Technologies), 10% FBS, and 1% penicillin/streptomycin with a concentration of cells 1×10^6 cells/ml, and injected into the microfluidic chamber using 24 AWG PTFE tubing (Cole-Parmer, Vernon Hills, IL, USA). At the time of injection, the suspended cells had an average radius of 7.0 ± 0.5 μm (Fig. 4.3). The chamber was incubated overnight (12-16 hrs) at 37°C and 5% CO_2 in a humidified environment to allow the cells to become adherent to the base of the chamber.

4.2.4 Fluorescence Time-lapse Imaging

Widefield fluorescence imaging was performed on a DMI6000B (Leica Microsystems, Bannockburn, IL, USA) equipped with a 63x/0.7 HC PL Fluotar L objective and a 20x/0.4 HCX PL FLUOTAR objective, L5 (Ex. 480/40; Em. 527/30) and Y3 (Ex. 545/25; Em. 605/70) filter cubes (all from Leica Microsystems), and a CM-9100-02 EMCCD camera (Hamamatsu Photonics, K.K. Shizuoka Pref., Japan). Confocal fluorescence imaging was performed on a LSM 800 (Carl Zeiss Microscopy, LLC, Thornwood, NY, USA) using a 63x/1.4 Plan Apochromat M27 oil immersion objective using 353 nm and 488 nm lasers for excitation and detection wavelength bands 400-490 nm and 490-617 nm for the NucBlue and CellTracker channels, respectively.

4.2.5 Cell Area and Volume Reconstruction

A z-stack of confocal images of cells adherent to the base of the chamber were obtained at a z-resolution of 0.37 μm, with each image measuring 100 μm $\times$ 100 μm (1000 $\times$ 1000 pixels). Image stacks were reconstructed in 3D Slicer (4.6.2) [236], imported into Mesh Lab (v2016.12) [237], and cleaned to remove isolated edges and vertices and close holes to make the mesh watertight. The surface area and volume of each cell were then calculated from these reconstructions. The mean and standard deviations of the cell surface area and volume ($n = 56$ cells) were plotted as histograms and against each other (Fig. 4.4a-b). The Pearson's r for the best fit regression line was $r = 0.71$, corresponding to a p-value of $p = 0.049$, indicating a good linear fit by the line $A = k_0 V + k_1$, where A and V are the cellular surface area and volume, in μm^2 and μm^3 respectively, and $k_0 = 1.2$ μm^{-1} and $k_1 = -390$ μm^2 are the constants that describe the statistical best fit line (Fig. 4.4c).

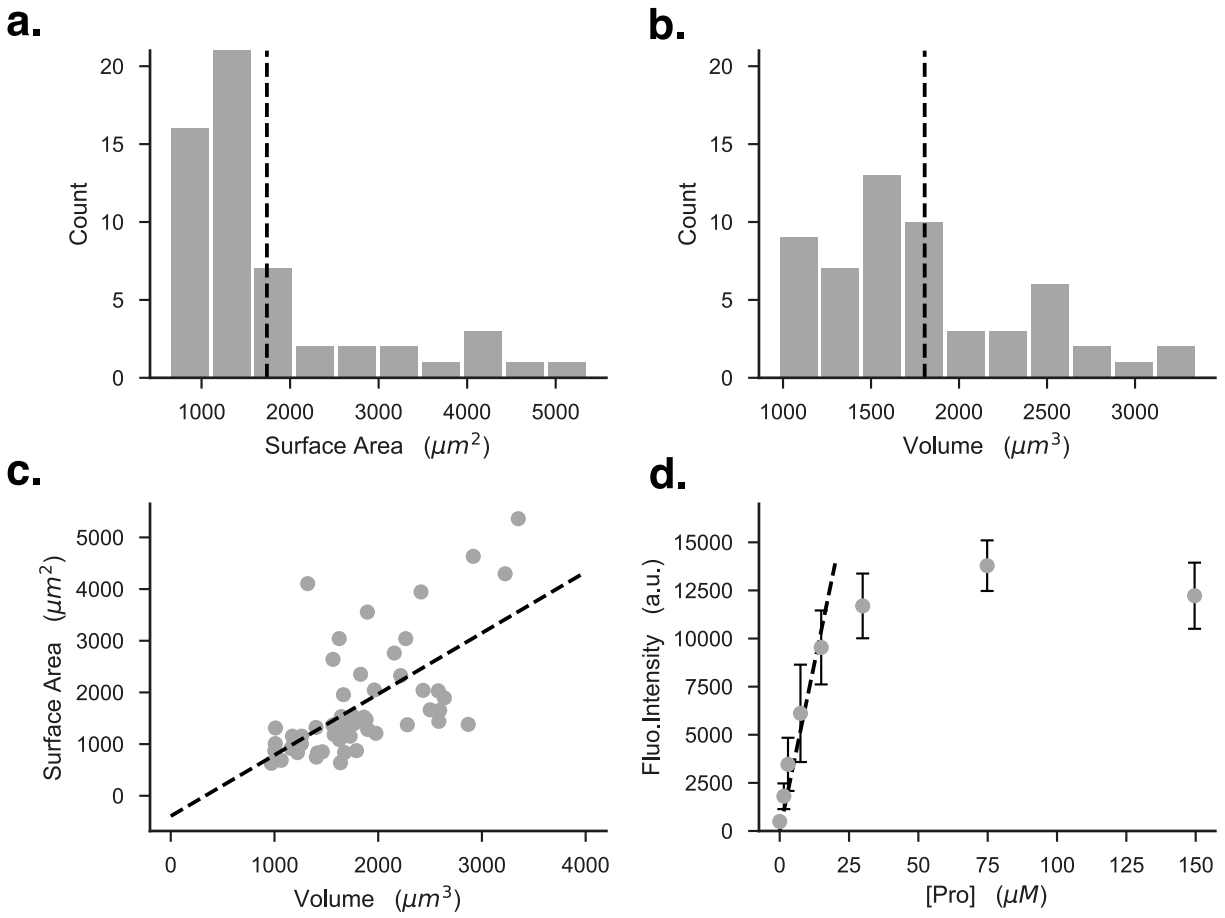

Figure 4.4: Calculating the average surface area and volume of a typical CHO-K1 cell in the microfluidic chamber enables the surface area to volume ratio to be calculated. The cells in the microfluidic chamber had a sphericity of $0.5 \pm .18$ with an average surface area of 1700 ± 1100 μm^2 (*a*) and average volume of 1800 ± 570 μm^3 (*b*). (*c*) The surface area and volume are correlated with a Pearson's r of $r = 0.71$ ($p < 0.05$) to the linear regression $A = 1.2V - 390$, where A and V are the cellular surface area and volume. (*d*) Chemical permeabilization was performed using 0.2% triton in PBS with varying concentrations of Pro and the slope of the concentration to fluorescence intensity standard curve was be calculated. The best fit line for the fluorescence intensity-concentration curve is 700 $a.u./\mu$M and passes through the origin.

4.2.6 Chemical Permeabilization and Fluorescence Calibration

Chemical permeabilization was performed in the microfluidic chamber using a solution of 0.1% Triton-X100 (Sigma, St. Louis, MO, USA) with propidium (0, 1.5, 3, 7.5, 15, 30, 75, 150 μM; ThermoFisher Scientific, Waltham, MA, USA) in PBS introduced into the chamber using a 1 ml syringe and 24 AWG PTFE tubing. Images were obtained five minutes following permeabilization

using a 20× objective with exposures of 20 ms, once the fluorescence intensity in the channel had stabilized (data not shown). Five images were obtained at each Pro concentration and each exposure using a 2×2 binning scheme. Chemical permeabilization treatments were performed in triplicate and it was determined that an extracellular Pro concentration of 30 μM at an exposure of 20 ms would allow free Pro ions to enter the cell, bind to double stranded nucleic acids, and remain below the saturation limit of the imaging system (Fig. 4.4d). The fluorescence intensity-concentration calibration relationship was determined to be $I = 700[Pro]$, where I is the fluorescence intensity and $[Pro]$ is given in μM, with a Pearson's r value of $r = 0.63$ and corresponding p-values of $p = 2.0 \times 10^{-7}$. This calibration provides a correlation between the bound intracellular concentration of Pro and the free intracellular concentration of Pro at equilibrium.

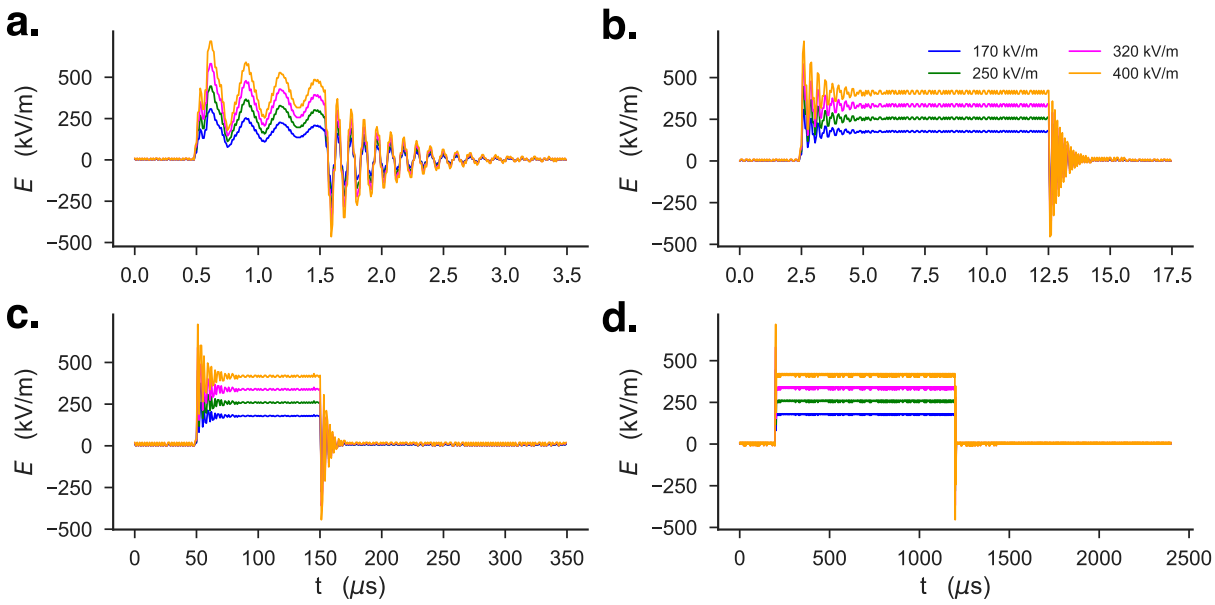

Figure 4.5: The strength of electric field E at each point in the channel is estimated using voltage measurements at the two electrodes and the chamber geometry. Pulse durations include waveforms of 1 μs (a), 10 μs (b), 100 μs (c), and 1000 μs (d). In each figure, E is presented as a function of time t. Significant ringing exists on the rising and falling edges of each pulse, and is consistently present between each pulse waveform. E is estimated using voltage traces (Fig. 4.2) as the Dirichlet boundary conditions on the electrode surfaces and solving for the static field inside the chamber. In these calculations, it is assumed that the medium in the chamber is purely ohmic. The labels 170, 250, 320, and 400 kV/m are derived from the E values at positions 2, 4, 6, and 8 mm along the long axis of the microfluidic chamber (Fig. 4.1), simulated using a idealized square pulse in an ohmic environment. These values are indicated by the steady-state portions of the square wave in this representation. For simplicity, each value of E is referenced using these labels.

4.2.7 Electric Field Applications

Electric field pulses were applied to the cells in the microfluidic chamber through stainless steel electrodes (0.18 mm diameter) inserted into the tubing at the inlet and outlet of the chamber. During PEF application, cells were immersed in one of three buffer solutions: phosphate buffered saline (PBS) containing 30 μM propidium (ThermoFisher) with no calcium and no magnesium, phenol–free serum-free culture medium (SFDF) 1:1 DMEM/F-12 (Gibco) containing 1% penn/strep and 30 μM propidium, or a low-conductivity, calcium-free medium containing 10 mM HEPES (Sigma, St. Louis, MO, USA), 250 mM sucrose (Fisher Scientific, Pittsburgh, PA, USA), 7.5 mM NaCl (Fisher Scientific) and 30 μM propidium. The pH of each buffer was adjusted to 7.2 using HCl and NaOH. The electrical conductivity of the buffers were 1.01, 0.93 and 0.08 S/m for the PBS, SFDF, and HEPES, respectively, while their respective osmolarities were 278, 306, and 310 mOsmol/l. An electrical amplifier based on an H-bridge topology was used to deliver 3 kV electrical pulses across the length of the chamber. A function generator (SDG 5082, Siglent, Solon, OH, USA) was used to trigger the amplifier and the output voltage was monitored using a high-voltage probe (BTX High-Voltage Probe, Harvard Apparatus, Hollistion, MA, USA) connected to an oscilloscope (DS1104, RIGOL Technologies Inc, Beaverton, OR, USA). The anode of the amplifier output was always positioned at the wide inlet of the chamber. PEFs were applied using a single pulse with four durations. Electrical pulses were always applied as a single 1, 10, 100, or 1000 μs pulse (Fig. 4.2), as measured from the initialization of the rising edge of the pulse, to the initialization of the ringing on the falling edge of the pulse. Images following the pulse application were obtained within 15 s of completion of the application and once every minute for the following 30 min. The electric field strengths at each position in the chamber are 170, 250, 320, and 400 kV/m, as estimated from the channel position (Fig. 4.1). Each electric field strength and pulse duration was tested on subpopulations of cells ($n = 27$ to 114 cells) in triplicate. Worst-case analysis of the Joule heating concomitant with pulse applications indicates that the Joule heating at the 250, 320, and 400 kV/m positions in the microfluidic chamber during a 1000 μs pulse in the most conductive buffers (PBS and SFDF) induced a $> 19^{\circ}$C temperature increase above room temperature (22°C), neglecting

any thermal loses. The resultant temperature increase would therefore remain below 37°C and well below the threshold for thermal damage for all other conditions, including the applications with the low-conductivity HEPES buffer under the same PEF conditions (Fig. 4.6).

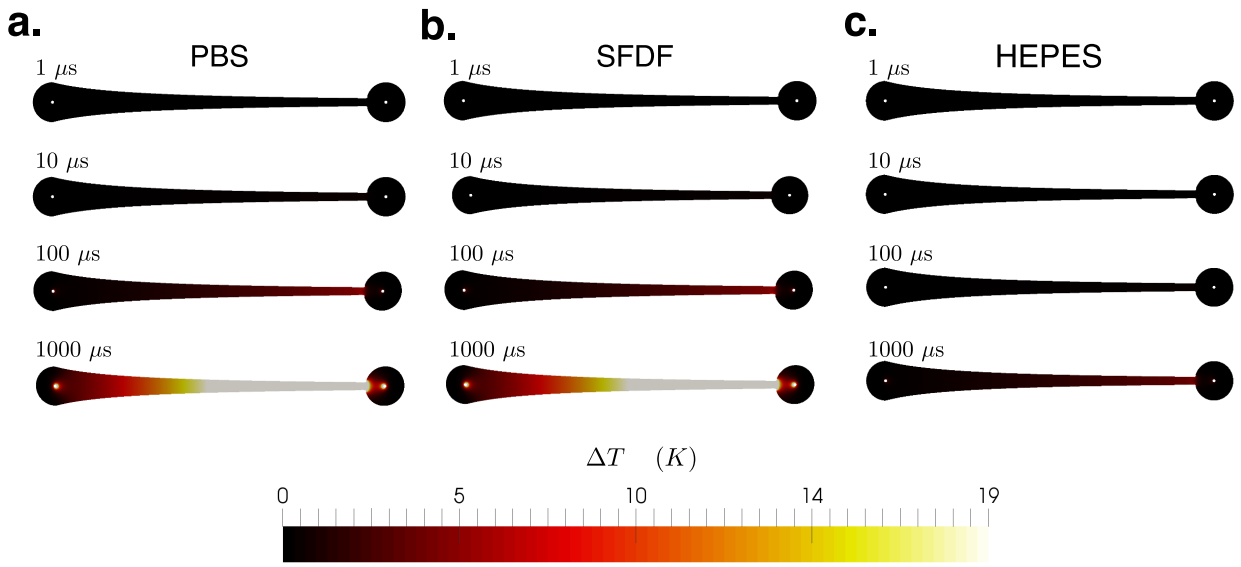

Figure 4.6: Numerical simulation of the Joule heating occurring during the microfluidic chamber during the course of treatment for a single pulse 1, 10, 100, and 1000 μs in width indicates that thermal damage is not a significant factor except for the cells in PBS (a) and SFDF (b) buffers treated with a 1000 μs pulse, and not at all for the cells in the HEPES buffer (c). Simulations were solved for the electrostatic case using $-\nabla\cdot(\sigma\nabla U)=0$ where U is the electric potential within the channel and applying 3 kV along the electrode surface on the wide end of the chamber. The electric field intensity distribution was used as the source term in the heat equation $\partial_t T-\alpha\nabla^2 T=\sigma|E|^2$ where $|E|=|-\nabla U|$, T is the temperature in the channel, the thermal diffusivity $\alpha=0.14$ m^2/s, and σ is the electrical conductivity for PBS (1.1 S/m), SFDF (0.98 S/m), and HEPES (0.08 S/m). Thermal analysis was performed by neglecting the ringing in the applied voltage waveforms and instead using the steady-state set voltage (3 kV) from the longer pulses. The ambient temperature was 22°C during all treatments.

4.2.8 Image Processing

Image files were parsed using FIJI (version 2.0.0-rc-43/1.51d) [238]. Batch image processing was performed on each stack of images at each time point and each position with the chamber using CellProfiler (v2.2.0) [239]. First, edge detection was performed on the blue channel (NucBlue-stained cells) of each image set using a Sobel filter and the nuclei in the resulting images were

identified. The nuclei in the blue channel were mapped to the red channel (Pro-stained cells) and the mean intensity, circularity, and area of the nuclei were measured and recorded at each point in time for each experimental condition.

4.3 Results

4.3.1 Quantitative Calculation of Pro Uptake

Previously, the diffusive permeability of the cell (herein referred to as *permeability*) has been shown to depend on the duration and degree of permeabilization of the membrane [58, 227, 232]. To measure permeability, time-lapse microscopy was used to observe the fluorescence intensity of the nuclei of CHO-K1 cells in a microfluidic chamber (Fig. 4.1). To ensure camera settings did not interfere with these correlations, calibrations were performed under imaging conditions under which fluorescence intensity of fluorescence signals did not saturate the camera sensor anywhere in the image. The nucleus was selected for observation because it exhibits a significantly greater fluorescence intensity than the other cellular components. In order to make our results quantitative, the average cell volume and surface area were determined. We experimentally established the relationship between the fluorescence of bound Pro within a cell's nucleus and the free Pro inside the cell ($[Pro]_{free}$) by developing standard curves. To obtain these curves, we chemically permeabilized cells in the presence of increasing fixed extracellular concentrations of Pro. Once the extracellular free Pro equilibrated with the intracellular free Pro and the intracellular bound Pro, the fluorescence intensity of the intracellular bound Pro became proportional to concentration of intracellular free Pro. Extracellular Pro concentrations were selected to be well below those determined to saturate the binding sites in the nucleus (Fig. 4.4d) once diffusive equilibrium between the intracellular free Pro and extracellular free Pro equilibrium and the binding equilibrium between the intracellular bound Pro and free Pro had been obtained. Therefore, at equilibrium inside the cell, our calibration provided an estimate the intracellular free Pro as a function of the fluores-

cence intensity of the bound Pro in the nuclei of permeabilized cells, based on the expectation that their interiors are well-mixed [240] and close to equilibrium [241].

This assumption of diffusive equilibrium is supported by many previous reports where the fluorescence of Pro and similar molecules are used as surrogates to assess the diffusive transport into cells. It has been shown that Pro-mediated intracellular fluorescence is able to reach it's peak intensity approximately 2 s following the delivery of an electrical pulse 100-fold longer than the maximum used in the present work [81]. Furthermore, it was noted that Pro is able to enter the cell, bind to nucleic acids in the cytosol, and become fluorescent in 60 μs, indicating that the binding process alone requires < 60 μs to occur [156]. Similarly-sized molecules have also been shown to readily and rapidly diffuse throughout the cell and cross the nuclear membrane after being microinjected into the cytoplasm [101, 242]. These measurements indicate that Pro is able to enter the cell, bind to nucleic acids, and become fluorescent within a time period tens to thousands of time smaller than the time scale of the 60 s interval between consecutive images we employ here. Furthermore, the fluorescence intensity of the Pro-bound nucleic acids outside the nucleus contribute a negligible integrated fluorescence intensity compared to those within due to the larger concentration of double-stranded nucleic acids it contains [94, 243]. We assume that the cell interior is well mixed and the bound Pro is close to equilibrium with free Pro in the cell interior and we therefore approximate the fluorescence intensity of the nucleus as reflective of the free Pro within the cell.

For the present study, a negligible pressure gradient existed across the cells in the microfluidic chamber [91, 146, 147]. Electrophoretic forces were neglected and the total flux of free Pro was considered purely diffusive $J_{Pro}(t) \approx \Delta(V[Pro](t))/A\Delta t$ [94, 156, 244], where $[Pro]$ refers to the concentration of intracellular free Pro. By determining the intracellular change in free Pro concentration over time ($\Delta[Pro]/\Delta t$) and treating the cell area and volume as constants, the permeability of the cell membrane $P_{m,Pro}(t)$ may be estimated as

$$P_{m,Pro}(t) \approx \frac{1}{[Pro]^{ext} - [Pro](t)} \left(\frac{V}{A}\right) \left(\frac{\Delta[Pro](t)}{\Delta t}\right), \tag{4.1}$$

where $P_{m,Pro}(t)$ is the membrane permeability, V and A are the volume and surface area of an average cell respectively, and $[Pro]^{ext} = 30\ \mu$M is the external concentration of Pro. $\Delta[Pro](t)$ and Δt are the change in Pro concentration and time, respectively, between two consecutive images in a time series. The slope $\Delta[Pro]/\Delta t$ was calculated numerically using a forward finite difference scheme between an image and the one immediately after it. The fluorescence intensity of the nuclei in each image were averaged and $P_{m,Pro}(t)$ was calculated using the image and the subsequent image in the series. A linear fit was performed for the first three minutes of each $[Pro](t)$ curve and the slope of this line was used to approximate its initial slope $\Delta[Pro]/\Delta t$. Then, the permeability of the cell membrane to Pro was calculated using equation 5.3. During the first three minutes of observation, $[Pro]^{ext} << [Pro](0 < t < 3)$ and therefore $[Pro]^{ext} - [Pro](0 < t < 3) \approx [Pro]^{ext}$ was assumed in these calculations (Tables 4.1, 4.2, 4.3).

Table 4.1: Average diffusive permeabilities of CHO-K1 cells immersed in PBS immediately following ($P_{m,Pro}(t \sim 0)$) and the final concentration of intracellular Pro 30 min after PEF application ($[Pro]_f$). Reported values are given as $mean \pm std$.

Pulse Width (μs)	E (kV/m)	$[Pro]_f$ (μM)	$P_{m,Pro}(t \sim 0)$ (pm/s)
n/a	n/a	0.34 ± 0.34	60 ± 22
n/a	n/a	0.049 ± 0.041	47 ± 32
n/a	n/a	0.053 ± 0.051	42 ± 33
n/a	n/a	0.035 ± 0.11	21 ± 25
1	170	0.96 ± 1.1	62 ± 39
1	250	0.21 ± 0.37	62 ± 52
1	320	0.12 ± 0.14	31 ± 25
1	400	0.070 ± 0.10	34 ± 24
10	170	0.48 ± 0.39	68 ± 50
10	250	0.38 ± 0.80	110 ± 85
10	320	0.31 ± 0.31	130 ± 110
10	400	0.64 ± 0.67	290 ± 180
100	170	0.29 ± 0.39	140 ± 890
100	250	1.1 ± 3.6	290 ± 900
100	320	1.2 ± 1.4	460 ± 300
100	400	2.0 ± 2.5	640 ± 560
1000	170	3.0 ± 4.4	1700 ± 2400
1000	250	9.3 ± 6.1	4800 ± 4600
1000	320	14 ± 6.5	7200 ± 4600
1000	400	15 ± 6.9	12000 ± 5900

To ensure that our calculations are consistent with these assumptions, the mass transfer Biot num-

Table 4.2: Average diffusive permeabilities of CHO-K1 cells immersed in SFDF immediately following ($P_{m,Pro}(t \sim 0)$) and the final concentration of intracellular Pro 30 min after PEF application ($[Pro]_f$). Reported values are given as $mean \pm std$.

Pulse Width (μs)	E (kV/m)	$[Pro]_f$ (μM)	$P_{m,Pro}(t \sim 0)$ (pm/s)
n/a	n/a	0.054 ± 0.055	21 ± 12
n/a	n/a	0.16 ± 0.84	62 ± 430
n/a	n/a	0.0050 ± 0.013	1.0 ± 8.7
n/a	n/a	0.28 ± 1.8	7.1 ± 13
1	170	0.045 ± 0.043	20 ± 26
1	250	0.045 ± 0.022	19 ± 20
1	320	0.042 ± 0.027	18 ± 15
1	400	0.059 ± 0.028	30 ± 18
10	170	0.095 ± 0.20	59 ± 36
10	250	0.28 ± 0.85	59 ± 51
10	320	0.24 ± 0.58	66 ± 37
10	400	0.45 ± 1.1	79 ± 37
100	170	0.43 ± 0.95	100 ± 44
100	250	0.69 ± 1.5	110 ± 56
100	320	1.1 ± 2.5	230 ± 280
100	400	4.6 ± 4.9	390 ± 340
1000	170	1.7 ± 2.3	440 ± 170
1000	250	8.6 ± 4.9	1400 ± 870
1000	320	13 ± 8.0	6000 ± 6200
1000	400	16 ± 4.5	13000 ± 4400

ber Bi_m was used to characterize the ratio of fluidic resistance to the flow of Pro across the cell membrane compared to the resistance to relatively free diffusion of Pro in the aqueous intracellular and extracellular environments. $Bi_m = LP_{m,Pro}/D_{Pro}$, where $L = V/A \approx 1$ μm is the characteristic length of the cell expressed as the ratio of the volume of a cell V to its surface area A, $D_{Pro} \approx 5.3 \times 10^{-13}$ m^2/s is the diffusion coefficient of Pro and similarly-sized solutes inside the cell [146, 240, 242, 245, 246, 247]. Imposing $Bi_m \leq 1$ indicates that the transport across the cellular membrane is slow compared to the diffusion on its interior and exterior. From this calculation, $P_{m,Pro} << 5.3 \times 10^{-7}$ m/s in order to make the well-mixed approximation. The maximum values we estimate for $P_{m,Pro}$ are as high as $1.3 \pm 0.4 \times 10^{-8}$ m/s (Tables 1-3), which indicates that this assumption is valid and we consider the intracellular space well-mixed and close to diffusive equilibrium.

While we have presented quantitative estimates of the cell membrane's diffusive permeability to

Table 4.3: Average diffusive permeabilities of CHO-K1 cells immersed in HEPES immediately following ($P_{m,Pro}(t \sim 0)$) and the final concentration of intracellular Pro 30 min after PEF application ($[Pro]_f$). Reported values are given as $mean \pm std$.

Pulse Width (μs)	E (kV/m)	$[Pro]_f$ (μM)	$P_{m,Pro}(t \sim 0)$ (pm/s)
n/a	n/a	0.039 ± 0.018	16 ± 27
n/a	n/a	0.015 ± 0.036	24 ± 24
n/a	n/a	0.022 ± 0.014	25 ± 10
n/a	n/a	0.024 ± 0.021	21 ± 12
1	170	0.20 ± 0.16	110 ± 97
1	250	0.032 ± 0.029	21 ± 25
1	320	0.078 ± 0.073	55 ± 45
1	400	0.19 ± 0.084	110 ± 34
10	170	0.28 ± 0.094	210 ± 77
10	250	0.58 ± 0.28	430 ± 230
10	320	0.96 ± 0.45	600 ± 320
10	400	1.3 ± 0.49	780 ± 310
100	170	1.4 ± 0.97	880 ± 640
100	250	2.9 ± 1.4	1700 ± 960
100	320	5.7 ± 3.7	2900 ± 1980
100	400	8.3 ± 4.4	4300 ± 3100
1000	170	10 ± 3.6	6200 ± 3400
1000	250	10 ± 4.2	6700 ± 3400
1000	320	11 ± 2.3	7800 ± 2800
1000	400	12 ± 3.0	9500 ± 2700

Pro ($P_{m,Pro}$), we must specify the appropriate context and scope of our analysis. The resolution limit of the 14-bit camera is approximately 30 μM$/2^{14}$ bit depth ≈ 0.001 μM under these conditions. To quantify the reliable resolution for our measurements using equation 5.3, we set the smallest possible value between two consecutive time point measurements and selected the concentration $[Pro](t \sim 0) = 0$ to give the worst-case resolution of our diffusive permeability calculation as approximately $P_{m,Pro} \approx 1 \times 10^{-12}$ m/s during the first few seconds to minutes following PEF application and $\sim 2 \times 10^{-8}$ m/s after 30 min. We note that the low resolution of our determination at later time points made it difficult to quantify the membrane permeability at these times. Below these limits, it is possible that a membrane had become permeable, but to a degree less than the resolution of our analysis would allow (i.e. $P_{m,Pro} < 1 \times 10^{-12}$ m/s) and would be considered impermeable. Further, the untreated controls are all at or below the resolution threshold in all measurements, indicating that they are below the threshold for reliable quantification of Pro

uptake.

4.3.2 Total Pro Uptake Increases with Increasing Post-Pulse Uptake Rate

To efficiently measure the membrane permeability, our microfluidic chamber was designed to enable simultaneous measurements of four electric field strengths. By acquiring images at 2, 4, 6, and 8 mm along the long axis of the chamber (Fig. 4.1), cells exposed to four electric field strengths could be monitored in a single experiment. We emphasize that the electric field strengths presented are approximate representations of the applied electric field, obtained under electrostatic assumptions and modeled using an idealized square waveform. In order to ensure that our observations were robust to variability in medium composition, we performed experiments in phosphate-buffered saline (PBS), phenol-free serum-free DMEM/F12 medium (SFDF), and a low-conductivity HEPES buffer containing sucrose to balance its osmolarity to a physiological range (approximately 300 mOsm). The intracellular-extracellular concentration gradient of Pro persists beyond 30 min following application for all experimental conditions. In Fig. 4.7, it is clear that the 100 μs and 1000 μs pulses greatly increased the permeability for cells in each application buffer. Additionally, the molecular uptake of Pro 30 min after application was greatly enhanced over the controls (Fig. 4.7d-f). The initial permeabilities showed little difference between PBS and SFDF (Fig. 4.7a-b). However, cells in HEPES became permeabilized at lower strength-duration thresholds (Fig. 4.7c). These cells appeared to become permeabilized in a manner less dependent on the pulse duration than PBS and SFDF, but with a similar dependence on local electric field strength. The population response of cells treated in the low-conductivity HEPES buffer was more uniform at each electric field strength and across pulse durations (Fig. 4.7). We conclude that membrane resealing governs the decrease in molecular uptake over the minutes following PEF application before diffusive equilibrium is established (Fig. 4.7). Our data suggests that one of the strongest predictors of the ultimate Pro uptake is the permeability in the minutes following PEF application. There is a strong correlation between the initial Pro uptake rate and the final concen-

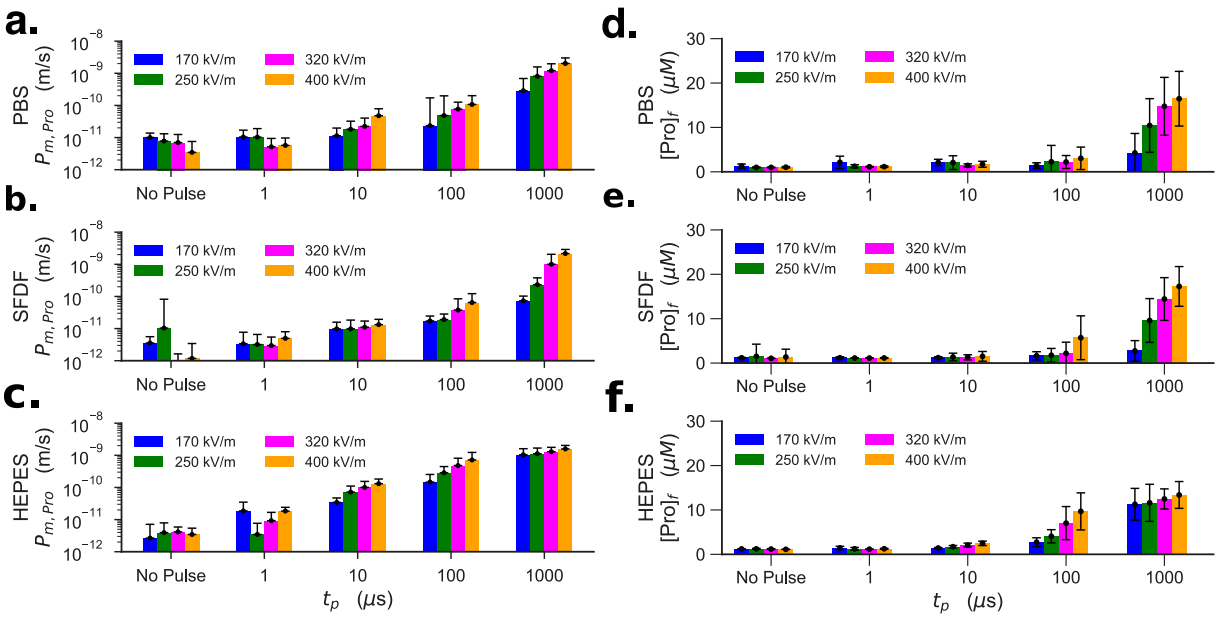

Figure 4.7: The cell membrane permeability to Pro, $P_{m,Pro}$ (log-scale), and the final Pro concentration 30 min following pulse application $[Pro]_f$ (linear-scale) increase with increasing pulse duration and electric field strength in each buffer. The permeability immediately following PEF application is calculated according to equation 5.3 for three different medium compositions: (*a*) PBS, (*b*) SFDF, and (*c*) HEPES. The average diffusive permeability of the cell membrane $P_{m,Pro}$ is averaged over the first three minutes of observation and presented as a function of pulse duration t_p and amplitude. Error bars are shown in only the positive direction due to the logarithmic scale on the vertical axis and represent the standard deviation. The total uptake of Pro 30 min following PEF application increases dramatically between pulse durations of 100-1000 μs and $E \geq 320$ kV/m for cells immersed in (*d*) PBS, (*e*) SFDF, and (*f*) HEPES. The final concentration of intracellular Pro $[Pro]_f$ measured 30 min following PEF applications is presented as a function of pulse duration t_p and amplitude. Error bars represent standard deviation. Numerical values are given in Supplementary Tables 1-3.

tration of Pro for cells in PBS, SFDF, and HEPES buffers, respectively (Fig. 4.8). Additionally, the pulse duration t_p and product of the pulse duration and local electric field strength t_pE are also strongly correlated to the concentration of Pro inside the cell after pulse application for cells in PBS, SFDF, and HEPES buffers, respectively. These observations are in good agreement with the current literature [224, 248, 249].

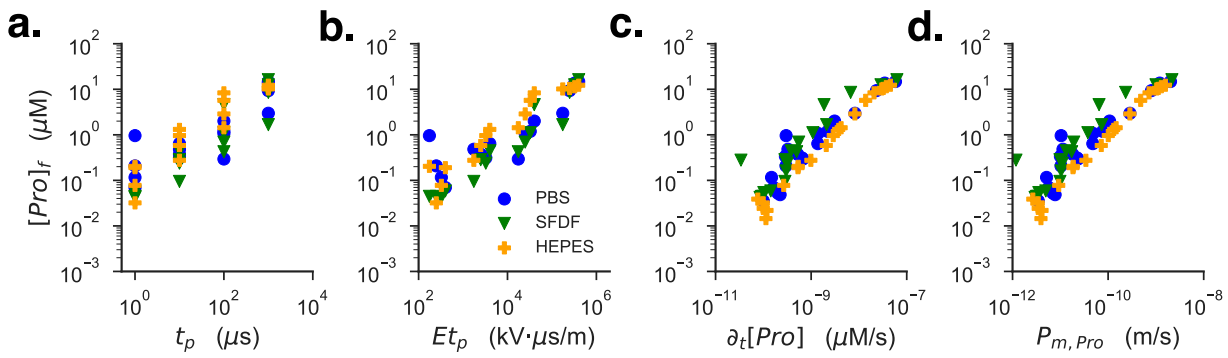

Figure 4.8: The final concentration of Pro inside a cell 30 min after application of a single electrical pulse is strongly correlated on (*a*) a log-log plot of $[Pro]_f$ (in μM; free concentration) vs. the pulse duration t_p ($p < 0.001$), (*b*) a log-log plot of $[Pro]_f$ vs. the strength-duration product Et_p ($p < 0.001$), (*c*) a log-log plot of $[Pro]_f$ the initial time rate of change of the intracellular concentration of Pro $\partial_t[Pro]^i$ ($p < 0.001$), and (*d*) a log-log plot of $[Pro]_f$ vs. the initial diffusive permeability of the cell membrane to Pro $P_{m,Pro}$ ($p < 0.001$). Pearson's r was determined for each correlation (data represented as log-log) and the p-values reported apply to each of the traces individually.

4.3.3 Slow Uptake Rates Correlate with Smaller Pulse Strengths

Following PEF application, we observed a subpopulation of cells exhibiting a prolonged uptake of Pro sufficient to achieve an intracellular concentration of 25% of the external Pro concentration after 30 min (Fig. 4.9a). This is an important basic finding. To identify this subpopulation, we calculated the final concentration of Pro inside the cell after 30 min ($[Pro]_f$) and the time at which the intracellular concentration reached half this value ($t_{1/2}$) (Fig. 4.9). For each cell $(t_{1/2}, [Pro]_f)$ was determined and plotted for each pulse duration and electric field strength combination (Fig. 4.9). Previous reports indicate that a delay of approximately 300 s may exist between the time of PEF application and significant permeabilization [93, 146, 147]. Therefore the cutoff of 5 min was used to discriminate between cells with overall slow rates of Pro uptake and those with more rapid uptake rates. Upon inspection, a threshold of 25% of the extracellular Pro concentration ($[Pro]^{ext}/4 = 7.5\ \mu$M) was selected to discriminate between cells allowing large or small quantities of Pro through the membrane.

This analytical scheme created four quadrants in the $(t_{1/2}, [Pro]_f)$ space (Fig. 4.10). The lower left quadrant is labeled Q_1 and corresponds to subpopulation of cells that reach their $[Pro]_f$ quickly,

but ultimately have $[Pro]_f < [Pro]^{ext}/4$. The lower right quadrant is labeled Q_2 and corresponds to the subpopulation of cells for which $[Pro]_f < [Pro]^{ext}/4$ and $t_{1/2} \geq 5$ min. The upper right quadrant is labeled Q_3 and corresponds to the subpopulation of cells for which $[Pro]_f \geq [Pro]^{ext}/4$ and $t_{1/2} \geq 5$ min. The upper left quadrant is labeled Q_4 and corresponds to the subpopulation of cells for which $[Pro]_f \geq 7.5$ μM and reached $t_{1/2} < 5$ min. At high electric field strengths and long

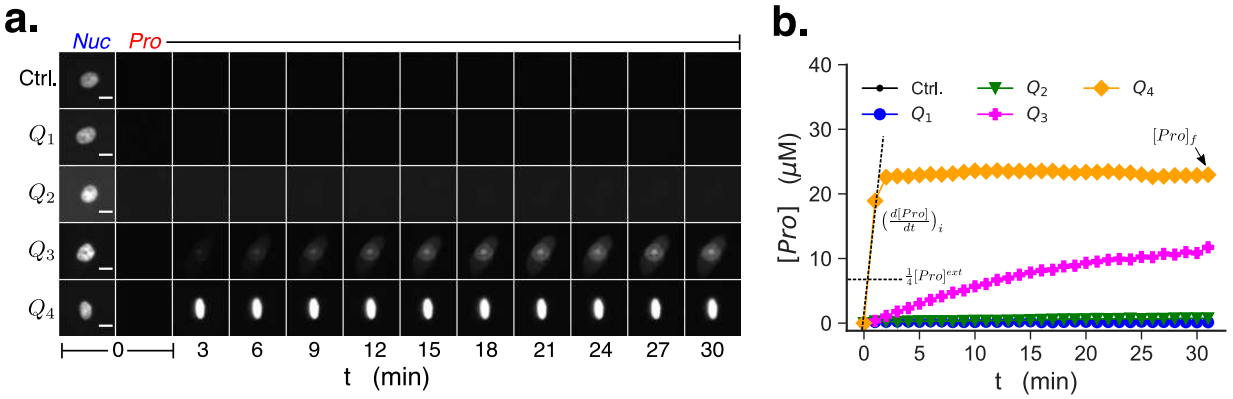

Figure 4.9: The intracellular concentration of Pro $[Pro]$ is presented as a function of time t for each image during the imaging period (30 min). (a) Time series images show uptake responses of single cells to a single electrical pulse as Pro enters cells at different rates. Nuclei are shown stained with NucBlue (Nuc; 10 μm scale bar) and Pro in the pre-treatment images and Pro alone in the remainder of the images. Control images are indicated by *Ctrl.*. (b) A cell's behavior is shown as one of four responses based on the time when the Pro fluorescence in the nucleus reached it's half-maximal concentration and the final concentration of intracellular Pro. A cell was classified as Q_1 if $t_{1/2} < 5$ min and $[Pro]_f < 7.5$ μM. The Q_2 subpopulation is based on $t_{1/2} \geq 5$ min. Q_3 is based on $[Pro]_f \geq 7.5$ μM and $t_{1/2} \geq 5$ min. Q_4 corresponds to $[Pro]_f \geq 7.5$ μM and $t_{1/2} < 5$ min. Uptake profiles are derived from the individual cells in (a) and show their individual Pro uptake responses over time. Untreated control data is indicated by *Ctrl.*.

pulse durations, cellular behavior is relatively homogeneous, with Pro rapidly entering nearly all cells rapidly after PEF application. Q_1 and Q_2 describe the behavior of cells exhibiting minimal Pro uptake regardless of whether the response is rapid (Q_1) or prolonged (Q_2). Cells in the Q_3 subpopulation, $t_{1/2} \geq 5$ min but eventually reach relatively large intracellular Pro concentrations compared to Q_1 and Q_2 cells ($[Pro]_f \geq [Pro]^{ext}/4$). Q_3 cells exhibit a large transient Pro uptake or experience a delay before becoming significantly permeabilized. The Q_4 subpopulation experiences a large, rapid influx of Pro. Across PEF application parameters and buffers, the Q_2 and Q_3 subpopulations appear to be intermediate responses between no electroporation and electropora-

tion (Fig. 4.11). Many of the cells exhibiting a prolonged Pro uptake (Q_3) have a similar $[Pro]_f$ compared with the subpopulation in Q_4, but with slower uptake rates and occur at lower strength-duration PEF thresholds. At the largest electric field strengths and longest pulse durations, the Q_3 subpopulation decreases and cells become more concentrated in the Q_4 subpopulation (Fig. 4.10).

4.4 Discussion

4.4.1 Large Membrane Permeabilities Induced by Single Pulses

We present estimates of the cell membrane permeability to Pro using measurements of the uptake rate into the cell. We show that a single 1000 μs electrical pulse at 400 kV/m can induce permeabilities of $1.3 \pm 0.4 \times 10^{-8}$ m/s to Pro, which is similar in size than ATP, but has a larger charge magnitude. Comparable permeabilities ($\sim 6 \times 10^{-9}$ m/s assuming a similar V/A ratio) have been induced for ATP by ten 100 μs or ten 1000 μs pulses in the same cell line and result in an ATP loss of 0.050 to 0.80 nmol/min with 120-400 nmol total ATP leakage [85]. Eight-pulse PEFs with amplitudes 80 to 120 kV/m have been shown to deplete cells of 50 to 95 % of their intracellular ATP [30, 31, 32, 250] and lead to a 25 to 50% decrease in cell viability in the presence 1 to 3 mM extracellular calcium.

At least two mechanisms could drive this loss of cell viability: ATP leakage and ATP depletion, though other physical and biochemical mechanisms could very well be implicated [117, 122]. Towards the former, approximately 5 nmol ATP is present within 10^6 typical mammalian cell [251, 252, 253]. With similar permeabilities of the cell membrane to ATP as those observed here for Pro, it may be possible to deplete cells within a given treatment volume of more than 25% of their intracellular ATP using a single electrical pulse.

With regard to the ATP depletion, it has been hypothesized that the entry of exogenous calcium re-

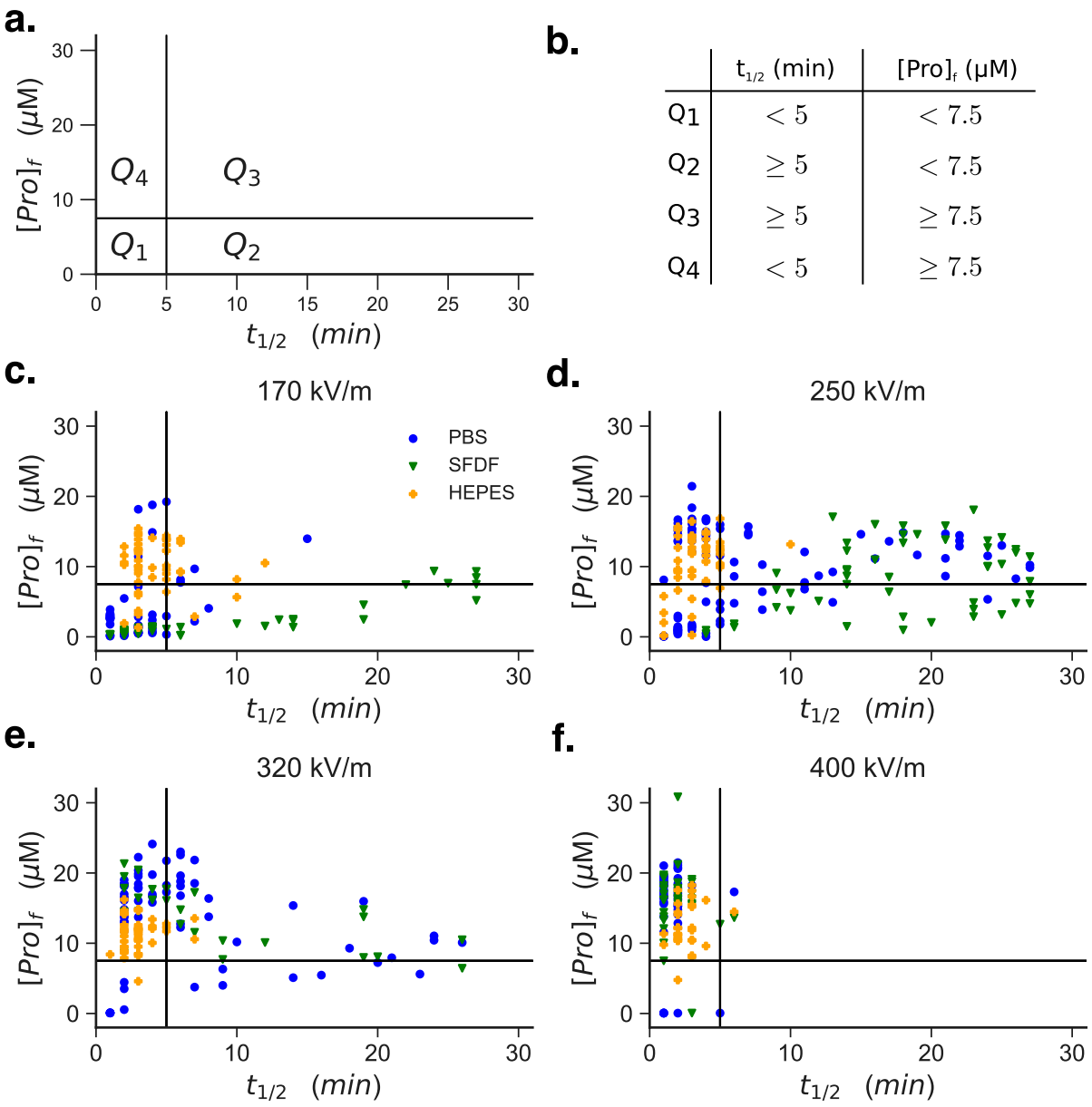

Figure 4.10: As the electric field strength increases, the fraction of cells in the Q_1 and Q_2 subpopulations decrease. Subsequently, a subpopulation with slow but more Pro uptake emerges (Q_3; upper right quadrant). At even larger E, most cells are part of the subpopulation exhibiting rapid Pro uptake (Q_4; upper left quadrant). Cellular response was quantified based on the final concentration of Pro 30 min post-application ($[Pro]_f := [Pro](t = 30 \text{ min})$) and the time at which each cell reached its half-final concentration ($[Pro](t_{1/2}) := [Pro]_f/2$) (*a*). Criteria for each quadrant are based on whether the Pro uptake of a cell 30 min following PEF treatment is $[Pro]_f \geq [Pro]^{ext}/4$ (horizontal lines) and whether the cell achieved $[Pro]_f/2$ within 5 min of PEF treatment ($t_{1/2} < 5$ min) (*b*). The data shown are for a single 1000 μs pulse at 170 (*c*), 250 (*d*), 320 (*e*), and 400 kV/m (*f*).

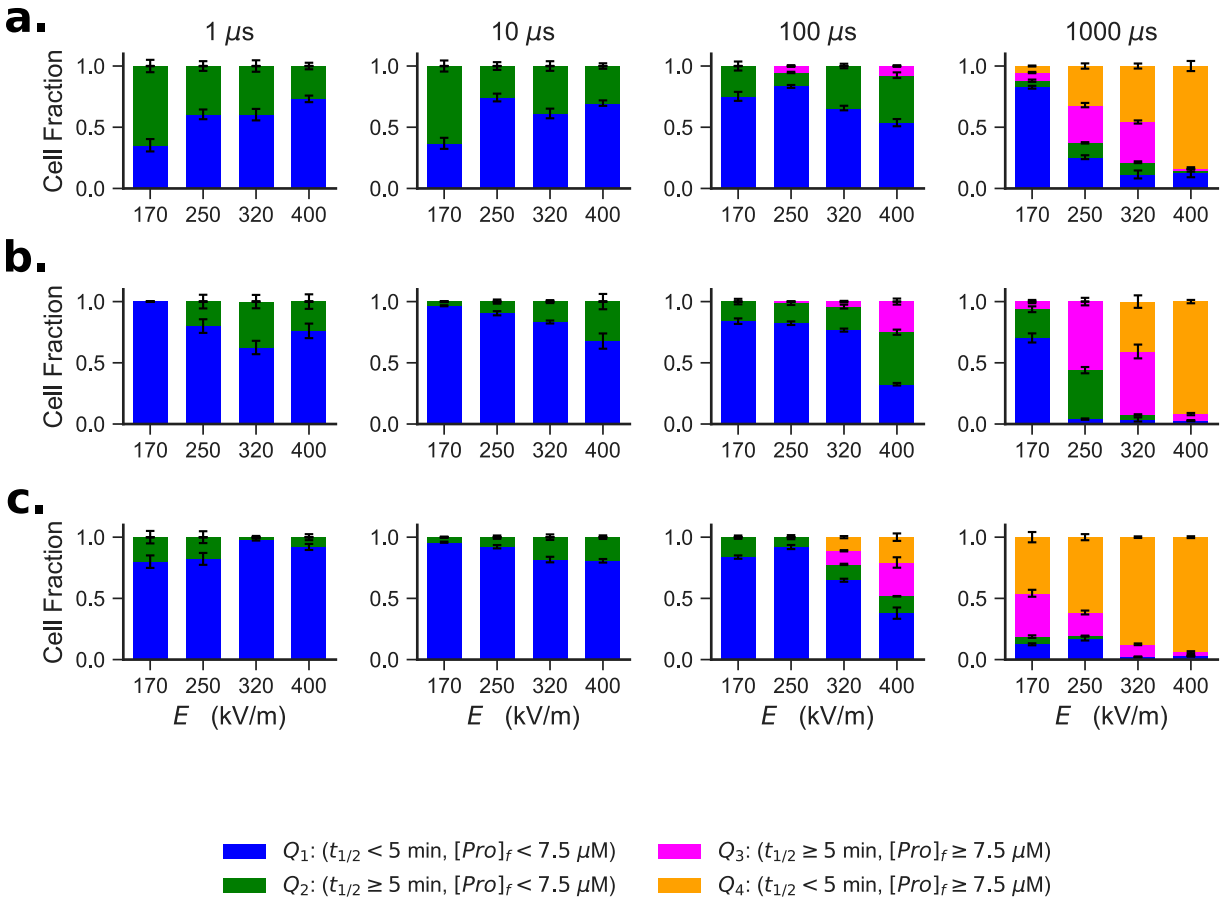

Figure 4.11: At electric field strengths and durations below the threshold for rapid Pro uptake, cells exhibit a prolonged uptake response that renders them sufficiently permeable to allow significant molecular transport. Data are shown for cells immersed each experimental buffer: PBS (*a*), SFDF (*b*), and HEPES (*c*). Each of the cell populations treated at a given pulse duration are split into four classifications Q_1, Q_2, Q_3, and Q_4. At shorter pulse durations (1-100 μs), the majority of cells contain relatively little Pro (Q_1 and Q_2 subpopulations). Larger Q_3 subpopulations are generated at intermediate pulse durations and strengths (320-400 kV/m with a 100 μs pulse; 170-400 kV/m with a 1000 μs pulse) and begin to become detectably permeabilized with $[Pro] \geq [Pro]^{ext}/4$ 30 min after PEF application, but with a slower, more gradual uptake rate ($t_{1/2} \geq 5$ min). Finally, at the longest pulse durations and largest electric field strengths, the Q_4 subpopulation contains the majority of the cells that facilitate fast rates of significant Pro uptake ($[Pro]_f \geq [Pro]^{ext}/4$; $t_{1/2} \leq 5$ min) through large cell membrane permeabilities up to $1.3 \pm 0.4 \times 10^{-8}$ m/s. The total cell population is presented as a sum of the fractional contributions from the Q_1, Q_2, Q_3, and Q_4 subpopulations. Error bars represent standard error and each column represents between 27-114 cells (62 average).

quires a cell to expend more ATP on calcium pumps to reestablish cellular homeostasis, potentially leading to its demise [30, 31, 32, 250]. We hypothesize that the estimates of $P_{m,Pro}(t)$ here pro-

vide a lower bound for quantitative estimates of calcium permeability, which has a similar charge and a diffusion coefficient approximately 2.5 times greater than that of Pro in water [136]. These estimates provide a heuristic context for the present work and indicate that it may be possible to take advantage of both of these mechanisms using single-pulse PEF application with a calcium adjuvant in order to decrease intracellular ATP and inhibit cellular recovery.

Other potential mechanisms of cellular damage have been reported including lipid peroxidation, the formation of reactive oxygen species (ROS), and metabolic thermal damage [254]. We note that bleb formation and biphasic increases in Pro (as in [93, 146, 147]) were observed (data not shown) and, with the prolonged Pro uptake of the subpopulation of cells in Q_3, could implicate the presence of ROS in the mechanism driving membrane injury [255]. Permeabilization is no doubt impacted by the temperature increase of greater than 19°C of the solution within the chambers containing PBS and SFDF for the 1000 μs pulse case (Fig. 4.6). However, these temperatures must be sustained for minutes for observable damage to occur [254], indicating that it is likely our observations still hold in the presence of such effects.

4.4.2 Prolonged Uptake at Intermediate Strength-Duration Thresholds

Our data shows a subpopulation of cells that experiences significant Pro uptake at lower electric field strength-duration thresholds than the general population (Q_3, Fig. 4.11). Due to the relatively long delay (3-10 min) between PEF application and the increase in Pro uptake, this phenomenon may be a biological or biochemical response. The Q_3 subpopulation appeared at strength-duration thresholds lower than required to produce large Q_4 subpopulations (Fig. 4.10). At larger electric field strengths and durations, this Q_3 subpopulation ultimately disappears as Pro enters the cells more rapidly (Q_4 subpopulation) [146, 147].

For PEF applications with pulse durations of nanoseconds to tens of microseconds, it has been shown that cells exhibit increasing delays of ≥ 5 min between application and a rapid influx of Pro [93, 146, 243]. In the present case this transition would fall into the Q_3 subpopulation, which

was observed to increase in cells exposed to applications of 100 to 1000 μs at 170 to 400 kV/m (Fig. 4.11). However, this lower strength-duration threshold still allows for the uptake of 25% of the external concentration of Pro (Fig. 4.8). While our data indicates that as many as 40% of a population of cells exposed to a single pulse are in the Q_3 subpopulation, others have suggested that this fraction could be as high as 83% for nanosecond pulses delivered in rapid succession [93]. These schemes induce delays on the order of 1000 s prior to appreciable membrane permeabilization. It was also observed that the fraction of cells in this state decreased when the time period over which the application was delivered increased [93]. These data are consistent with our results and implicate a transitional region in the electric field strength-pulse duration space (Q_3) that emerges for parameters that are insufficient to outright cause immediate permeabilization.

4.4.3 Impact of PEF Parameters on Cell Behavior

During our study, PBS, SFDF, and HEPES buffers were used to provide a more thorough investigation into post-PEF cell behaviors. Interestingly, cells immersed in the HEPES buffer appear to exhibit a homogenous response, compared to cells treated in PBS or SFDF. While similar trends exist in the appearance and disappearance of the Q_3 subpopulation with increasing PEF strengths and durations for each medium, the Q_4 subpopulation begins to contain the majority cells at lower strengths and durations for the cells treated in the HEPES buffer (Fig. 4.11). One explanation could be that the increased permittivity due to zwitterions [256, 257] and the decreased conductivity due to the sucrose [249, 258] in the HEPES buffer increases the electrical relaxation time of the membrane. In this way, effects of small variations in the capacitance of individual cell membranes could be reduced and therefore effectively reduce the variation in cellular response to PEFs. The increased permittivity of the HEPES buffer could also enhance the electrical force on the cell membrane and lower the strength-duration threshold at which appreciable electroporation is observed [256, 257]. This delay is present in cells treated in each buffer and may therefore be the result of an osmotic pressure difference. Cells that experience a prolonged permeabiliza-

tion may be more efficiently killed by an increased osmotic pressure difference change post-pulse, thereby minimizing thermal damage and improving tumor ablation protocols [259]. Regardless of the mechanism, cells belonging to the Q_3 subpopulation exhibit a prolonged Pro uptake and ultimately yield significant intracellular Pro concentrations ($[Pro]_f \geq [Pro]^{ext}/4$; Fig. 4.10). If such a mechanism could be exploited to affect cells *in vivo*, electroporation-based applications and therapies involve lower electric field strengths, resulting in significantly less thermal damage than present application paradigms.

One limitation of the present study is the significant ringing that complicates the rising and falling edges of the pulses (Fig. 4.5) with amplitudes approximately $\pm$3 kV beyond the 3 kV set voltage (Fig. 4.2). However, it was shown that the time spent above the strength-duration electroporation threshold that matters, with a 10% sinusoidal modulation of the pulse amplitude having little impact on the electric field strength and pulse duration at which cells become permeabilized [227]. It was determined the time spent above the critical electric field strength is the most significant parameter governing electroporation [232]. The ringing present on the rising and falling edges of each pulse was present for $\leq$50% of the total pulse duration for all but the 1 μs pulse, and therefore we anticipate that this ringing will not dramatically impact these results.

Such a waveform could be functionally similar to a high amplitude pulse followed by a longer low-amplitude pulse, which has been shown to enhance molecular delivery by first permeabilizing the membrane then electrophoretically driving the charged molecules into its interior [260]. Our data for 1 μs pulse applications differs little from the untreated controls and thus indicating a minimal permeabilization of the cell membrane (Fig. 4.8). We consider further analysis of this waveform's effects to be outside the scope of the present study.

4.5 Conclusion

We report a research method for quantitatively determining a membrane's diffusive permeability to Pro using fluorescence microscopy. We determine the diffusive permeability to propidium (Pro) for pulse durations of 1-1000 μs and electric field strengths of 170-400 kV/m in three buffers, and find that the cell membrane permeability to propidium ions can reach $1.3 \pm 0.4 \times 10^{-8}$ m/s. We also show that the increased permeability persists for at least 30 minutes. Further, for Pro the initial influx rate is a strong predictor of a cell's final intracellular Pro concentration. Finally, we identify a subpopulation of cells that have larger concentrations of Pro after a prolonged uptake (100 s) than cells exposed to smaller fields. Our results both technically enable and experimentally provide a basis for future quantitative investigations that: (1) determine lethal permeabilities, (2) examine transitions in Pro uptake kinetics, and (3) provide experimental uptake rates for comparison with predictions of cell-level computational models.

4.6 Appendix A: Electrostatics Simulation Code

The following code simulates the potential field within the microdevice developed in in this chapter for single-cell electroporation experiments. The geometry of the CAD drawing was created using a a separate script using polynomial splines to interpolate the boundary of the geometry, based on the CAD file. These splines were sampled and used to generate a GMSH geometry file (`.geo`), which included surface labels for the electrodes and a volume label for the 3D chamber geometry. GMSH was used to convert the file into a mesh (`.msh`), which was then converted into three XML files (`chamber.xml`, `chamber_facet_region.xml`, `chamber_physical_region.xml`) using `dolfin-convert` from the FEniCS project. The following code using linear ($p = 1$) Lagrange shape functions and strong-form boundary conditions to solve for the electrostatic potential field within the microdevice chamber. The code outputs a file readable in ParaView (`chamber.pvd`).

```
from fenics import *

## Import Mesh
ofilename = 'chamber.xml'
mesh = Mesh(ofilename)
subdomains = MeshFunction("size_t", mesh,
                "%s_physical_region.xml"%ofilename.split('.')[0])
boundaries = MeshFunction("size_t", mesh,
                "%s_facet_region.xml"%ofilename.split('.')[0])

## Assign boundary conditions
V = FunctionSpace(mesh, 'CG', 1)

## Define boundary conditions
boundary_conditions = {1: {'Neumann': 0},
                       12: {'Dirichlet': 1},
                       13: {'Dirichlet': 0}}

## Apply boundary conditions
bcs = []
integrals_N = []
integrals_R_a = []
integrals_R_L = []
for i in boundary_conditions:
    if 'Dirichlet' in boundary_conditions[i]:
```

```
        bc = DirichletBC(V, boundary_conditions[i]['Dirichlet'],
                         boundaries, i)
        bcs.append(bc)

    if 'Neumann' in boundary_conditions[i]:
        if boundary_conditions[i]['Neumann'] != 0:
            g = boundary_conditions[i]['Neumann']
            integrals_N.append(g*v*ds(i))

    if 'Robin' in boundary_conditions[i]:
        r, s = boundary_conditions[i]['Robin']
        integrals_R_a.append(r*u*v*ds(i))
        integrals_R_L.append(r*s*v*ds(i))

## Define functions
u = TrialFunction(V)
v = TestFunction(V)
f = Constant(0)
g = Constant(0)
a = dot(grad(u), grad(v))*dx + sum(integrals_R_a)
L = f*v*dx - sum(integrals_N) + sum(integrals_R_L)

## Solve system
u = Function(V)
solve(a==L, u, bcs)

## Save solution to file (VTK format)
vtkfile = File('channel.pvd')
vtkfile << u
plot(u)
```

Chapter 5

Characterization of Cell Membrane Permeability *In Vitro* Part II: Computational Model of Electroporation-Mediated Membrane Transport

Daniel C. Sweeney[a*], Temple A. Douglas[a], and Rafael V. Davalos[a]

[a] Department of Biomedical Engineering and Mechanics, Virginia Tech, Blacksburg, VA, USA

* Corresponding author

Author Contributions

DCS and TAD conceived of and performed the simulations in this work and wrote and edited the manuscript. and RVD edited the manuscript.

Manuscript in review

5.1 Introduction

An intact cell membrane normally provides a barrier to most molecular transport into and out of a cell. Electroporation (EP) is a biophysical process in which brief, yet intense, electrical pulses disrupt bilayer membranes to enhance the flow of molecules. The electrically-motivated build-up of charged molecules at the water-lipid interface raises the transmembrane potential (TMP) [68, 71, 109, 190]. When the TMP reaches threshold values of 0.2-1.0 V, EP spontaneously occurs as polar molecules are inserted through the membrane [14]. Simulations of molecular systems including phospholipids, water, and other small molecule solutes have shown that nano-scale pore formation occurs on the order of picoseconds to nanoseconds [67, 70].

When applied to cell membranes, EP-mediated generation of pores enables solutes to better flow into and out of the cell. In the seconds to hours following EP, these pores can reseal to again inhibit molecular transport [89, 261]. The formation of pores is typically modeled using the asymptotic Smoluchowski model (ASM), which enables the calculation of the dynamic pore density on a membrane [168]. This model considers the surface tension, pore tension, electrical energy, and steric hindrance of the membrane as lipid molecules reorganize into pores approximately 0.8 nm in radius [72]. The ASM agrees with experimental results [102] and has been widely implemented in EP models [79, 80, 111, 182, 184]. However, the ASM relies on the exponential of the squared TMP and therefore requires small time steps to numerically resolve. Furthermore, application of the TMP over a simulated cell with sufficient resolution to capture the spatiotemporal dynamics of EP is computationally intensive and functionally inhibits calibration with experimental data.

The translation of the ASM to an effective permeability has been used to couple the generation of membrane pores with the electric flux continuity [144] and drift-diffusion equations [262]. Measurements of the electric current through the cell membrane decreases from 30-260 to 0 pA over 10-500 ms following *in vitro* EP treatment [103]. Experimental data have also shown the rate at which exclusion dyes enter a cell after EP decreases over 190-289 s following [85] from initial permeabilities from 8.57×10^{-12} m/s for a 20 μs pulse at 300 kV/m [89] asl well as from 1.3×10^{-8} m/s for a 1 ms pulse at 400 kV/m (in the accompanying paper). These permeability measurements are more readily compared to computational models through the abstraction of aggregate membrane pores to a net membrane porosity [152, 161, 241, 263].

Due to the large discrepancy in time scales between electric current and molecular uptake measurements, models of membrane porosity often include three to four stages in which an electroporated membrane can exist [12, 85, 153]. In these schemes, an intact membrane is modeled as having a minimal permeability. When the TMP reaches the EP threshold, the membrane becomes sufficiently permeable to conduct small ionic currents. At this stage, the membrane still inhibits the transport of larger molecules, such as exclusion dyes. As its porosity increases, especially during EP schemes comprised of longer pulses (0.1-1.0 ms), larger polyions and other small molecule solutes are able the cross the cell membrane [85, 89]. The net porosity of the cell membrane is modeled as a linear combination of these porosity stages weighted by the fraction of the membrane in each stage, with a dynamical system representing the flow of the membrane through each available stage.

Once porous, membranes shunt ionic currents along the charge gradient, decreasing the TMP [72, 111]. This charging to the EP threshold, followed by the rapid formation of membrane pores, results in a characteristic sharp peak in the evolution of the TMP over time [103]. Lumped parameter resistive-capacitive circuit models have been used to model the ionic currents through each pore stage [72, 140, 264, 265]. The parallel flow of ionic currents through the fraction of the membrane in each porosity stage is driven by an applied electric field, modeled as a source voltage in series with a Thevenin equivalent resistance that models the resistance of the buffer surrounding the cell.

In order to investigate EP-facilitated membrane permeability within a theoretical framework, we developed a cell membrane circuit model coupled with a dual-porosity model and simple diffusion. We calibrated our model using experimental data reported in the accompanying paper (Chapter 4), including pulse durations of 1-1000 μs, electric field strengths of 170-400 kV/m, and three buffer compositions: phosphate buffered saline (PBS), serum-free DMEM/F-12 cell culture medium (SFDF), and a low-conductivity 4-(2-hydroxyethyl)-1-piperazineethanesulfonic acid buffer (HEPES). Analysis of this model indicates that it is asymptotically stable following the removal of the applied electric field (i.e. during pore resealing). Model parameters and variables were normalized, which reduced the parameter space to six parameters. Five of these parameters were fixed based on existing literature and the sixth, the forward transition rate between the low-porosity stage and the high-porosity stage, was fit to quantitative experimental data (Chapter 4). Our results indicate that buffer composition plays a critical role in EP-mediated membrane porosity.

We extend our model to examine its implications for multi-pulse EP schemes. These results indicate that the relaxation of the high- to low-porosity stage is slow and results in a relatively long-lived membrane fraction in the high-porosity stage, compared to the fraction in the low-porosity stage. We show that the difference in relaxation time scales gives rise to a membrane permeability increase proportional to the square root of the pulse number. Finally, we demonstrate that the difference in relaxation times between the high- and low-conductivity stages which explains the negligible impact of delays of less than 100 ms between consecutive pulses. The small parameter space and conclusions of our model are consistent with existing literature and serve as a robust link between experimental observations and theoretical models. While the scope of the present work focuses on the biophysical mechanisms governing EP, we acknowledge that it has direct applications to optimizing clinical techniques using EP processes, including electrochemotherapy. Robust linkages between theoretical and experimental results are critical to improving clinical EP technology. Our model provides a simple, concise methodology exploring these connections in greater depth.

5.2 Materials and Methods

We develop the following system of equations to describe EP and subsequent molecular transport into a single idealized, spherical cell immersed in an aqueous buffer

$$\frac{dN}{d\tau} = \alpha U^2 - \delta U^2 N - \beta N + \eta M, \tag{5.1}$$

$$\frac{dM}{d\tau} = \delta U^2 N - \eta M, \tag{5.2}$$

$$\frac{dX}{d\tau} = \xi M(1-X), \tag{5.3}$$

$$\frac{dU}{d\tau} = U_s - U\big(1+\gamma(N+M)\big), \tag{5.4}$$

where $N \in [0,1]$, $M \in [0,1]$, $X \in [0,1]$ and U and time τ are the result of normalization according to

$$N := \frac{N_m}{N_0}, \quad M := \frac{M_m}{M_0}, \quad U := \frac{U_m}{U_0}, \quad X := \frac{X_m}{X_0}, \quad \tau := \frac{t}{\tau_{RC}}. \tag{5.5}$$

N is fraction of the membrane area and N_0 the maximum area of the cell membrane that is conductive of small ions yet restricts the entry of larger molecules. M is the fraction of the membrane area and M_0 is

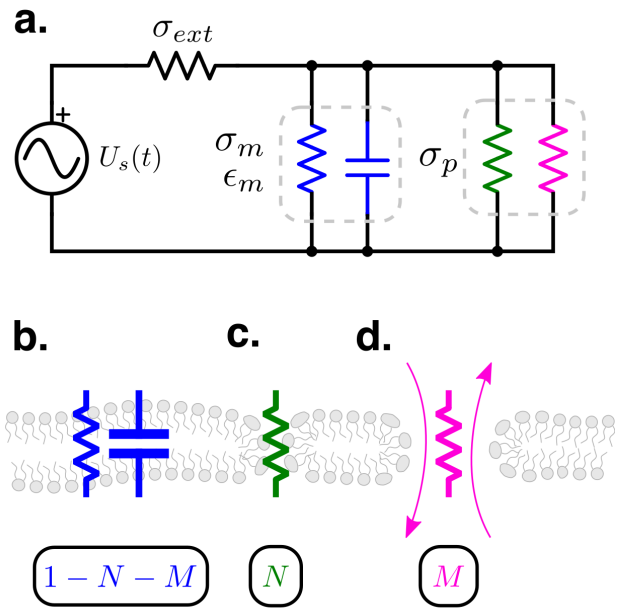

Figure 5.1: EP Model diagram. (a) Electrical schematic representation of the cell membrane charging including the extracellular conductivity σ_{ext} to model the electric current incident to the cell membrane. The conductivity of the cell membrane is given by the parallel conductivities of the naive membrane and porous membrane weighted by the membrane fraction in each stage. (b) The naive membrane contributes a conductivity and permittivity to the electrical model. (c) The N membrane fraction contributes to the permeabilized conductivity of ionic currents σ_p but does not permit the transport of larger solutes. (d) The M membrane fraction contributes to σ_p and permits diffusive transport of solute X. Note that the membrane dielectric constant was considered constant across each membrane fraction and in time.

the maximum area of the cell membrane that permits the entry of larger solutes, such as propidium. X is the intracellular concentration of a solute, such as propidium, and X_0 is its extracellular concentration. U is the TMP, U_0 is the electroporation threshold voltage, $\tau_{RC} = \varepsilon_m/\sigma_m$ is the RC time constant of the cell membrane, and σ_m and ε_m are the conductivity and permittivity of a naive cell membrane, respectively.

Equation 5.1 describes the fractional poration of the cell membrane generated by transmembrane potential U. α is the rate at which N is generated. The second term describes the transition from the N porosity stage to the M porosity stage that occurs at rate δ and is motivated by the presence the transmembrane potential U. The third term in equation 5.1 describes the transition from the N stage back to a naive membrane stage with rate constant β. The fourth term describes the M to N transition that occurs at rate η. Within this scheme, the membrane fraction in the M stage cannot exist without passing through the N stage during generation and relaxation.

With the duration of the applied electric field thousands-fold shorter than the interval between the control measurement and the first post-treatment measurement in the experimental data (Chapter 4), we assume that the molecular flux into the cell interior is purely diffusive. A Hagen-Poiseuille model of mass transport through a porous membrane was used to develop equation 5.3, where ξ is the normalized permeability coefficient of the M porosity stage. Flow through a porous membrane is given according to equation 5.3 with the permeability coefficient is given by $\xi = 3H(\lambda_M)D_\infty\tau_{RC}/(rh)$ [161, 266], where D_∞ is the free diffusion coefficient of solute X in an aqueous environment, h is the membrane thickness, r is the cell radius, and $H(\lambda_M)$ is the hindrance factor. This approximation assumes that $H(\lambda_0) << H(\lambda_M)$ and $H(\lambda_N) << H(\lambda_M)$ where λ is the ratio of the solute radius to the pore radius. This formulation also assumes that the porosity of the cell membrane is uniformly distributed across the cell membrane and that flow into the cell occurs in the radial direction only. Modeling pores as cylinders, the hindrance factor $H(\lambda) \in [0,1]$ is evaluated using a formula corrected for small porosities [160, 161, 267]. Assuming $\lambda_M \approx 0.62$ and $H(\lambda_M) = 1.3 \times 10^{-2}$, ξ is defined as $\xi = 3H(\lambda_M)D_\infty\tau_{RC}/rh = 5 \times 10^{-4}$. With *a priori* knowledge of the molecular radius of solute X, ξ can be estimated from these calculations as well as from experimental measurements [85, 89].

Equation 5.4 is derived from a circuit model of an electroporated cell membrane [265] (Appendix A). The value of time constant τ_{RC} is both well-known for single cells ($\tau_{RC} = 1 \times 10^{-6}$ s). γ is also well-defined, as both the conductivity of a naive membrane σ_m and the conductivity of a completely porous membrane σ_p have been experimentally measured [103] and estimated to be $\gamma = 1 \times 10^6$.

5.3 Results

5.3.1 Parameter Fitting

Equations 5.1 - 5.4 were implemented in Python 3.6 using the LSODA algorithm [268] with the `odeint()` function in the Scipy (0.18.1) module [269]. The solver was initialized with the initial conditions $N(0) = 0$, $M(0) = 0$, $X(0) = 0$, and $U(0) = 0$. A stability analysis revealed that the model is asymptotically stable following the removal of the applied electric field (Appendix B). Experimental time-series data from single cell experiments were used to calibrate the model (Chapter 4). Within this dataset, the observed average

molecular uptake was calculated from experimental data prior to electric field exposure and each minute for 30 min following treatment to obtain 31 total observations for each electric field strength and pulse duration combination. The mean and variance were calculated for each measurement. In order to estimate δ for all treatments for each buffer composition, the Nelder-Mead method was implemented using the `minimize()` function in the LmFit (0.9.7) module to minimize the sum of square residuals given by

$$SSR = \frac{1}{T}\sum_{i}^{T}\left(\frac{X_{model}(t_i) - X_{data}(t_i)}{X_{data}(t_i)}\right)^2, \tag{5.6}$$

where $X_{model}(t_i)$ and $X_{data}(t_i)$ are the model and data points for X, respectively, at time t_i ($T = 31$). Simulations were plotted over the experimental data and show good agreement visually, with the maximum $max(SSR_{PBS}) = 0.025$, $max(SSR_{SFDF}) = 0.0070$, and $max(SSR_{HEPES}) = 0.0066$ (Fig. 5.2). Notably, the N to M generation rates δ were similar for cells immersed in PBS and SFDF, but were consistently three- to five-fold larger for cells immersed in HEPES buffer.

Table 5.1: Model parameters

Parameter	Value	Description	Reference
α	2.0×10^{-6}	N formation rate	[82]
β	4.0×10^{-8}	N relaxation rate	[103, 168, 261, 270]
γ	1.0×10^{6}	relative naive membrane resistance	[103, 265, 270, 271]
η	4.0×10^{-9}	M relaxation rate	[85, 89]
ξ	5.0×10^{-4}	permeability coefficient	[85, 89, 161]
λ_M	0.63	solute radius / pore radius	[161]
τ_{RC}	1.0	RC time constant (μs)	[103, 226, 272, 273]
D_∞	0.5×10^{-9}	Solute diffusivity X (m^2/s)	[136]
h	5.0	membrane thickness (nm)	[274, 275]
r	7.5	cell radius (μm)	Chapter 4
σ_{PBS}	1.01	PBS conductivity (S/m)	Chapter 4
σ_{SFDF}	0.93	SFDF conductivity (S/m)	Chapter 4
σ_{HEPES}	0.08	HEPES conductivity (S/m)	Chapter 4

5.3.2 HEPES Buffer Increases Membrane Permeability

Experimental data from three different buffer compositions indicate that cells immersed in the HEPES buffer during EP experienced a larger molecular uptake following the application of the 100 μs pulse than the cells immersed in PBS or SFDF. With a 1000 μs pulse, the ultimate molecular uptake was similar for each of the

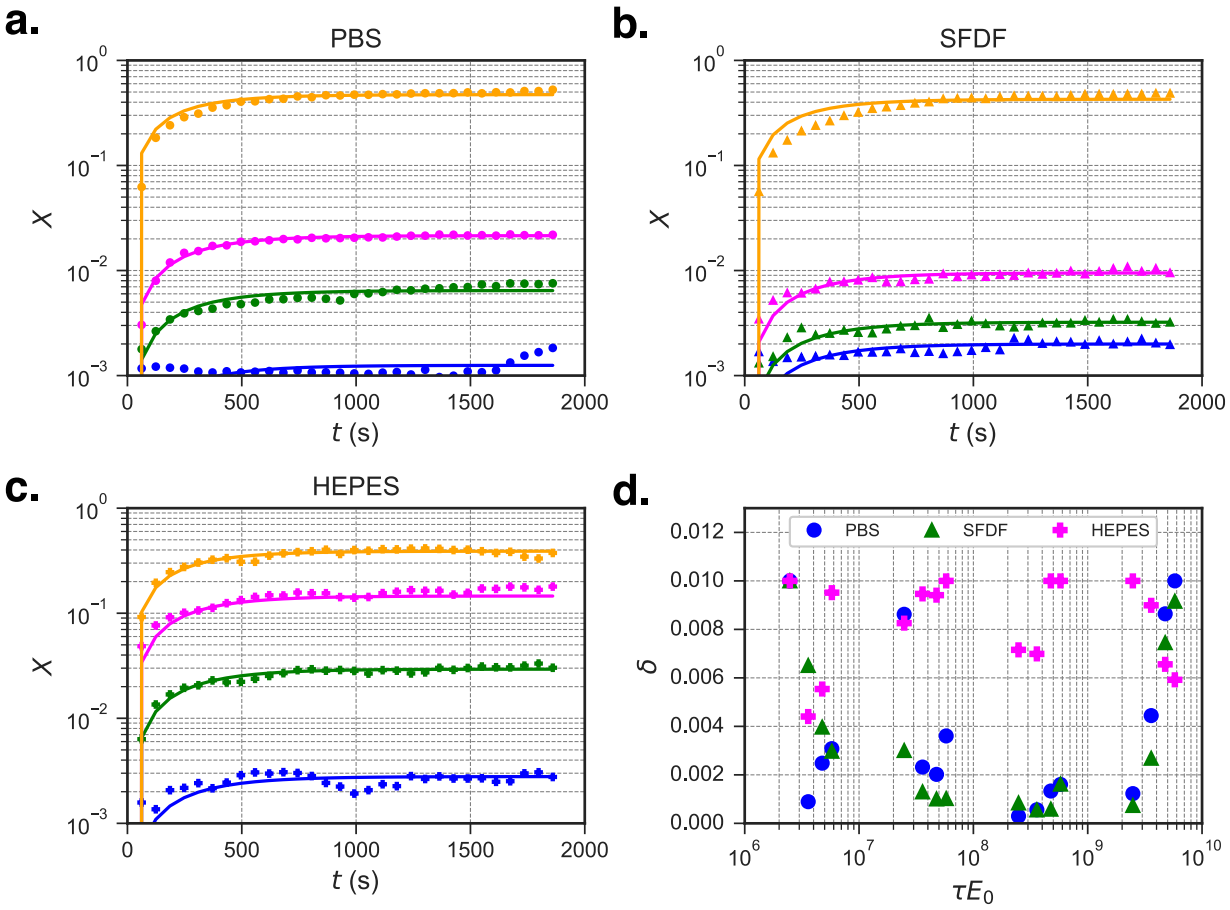

Figure 5.2: The two-stage model recapitulates experimental averages of molecular uptake. Representative parameter fits are shown for X for cells exposed to a 100 μs pulse in (a) PBS, (b) SFDF, and (c) HEPES. Equations 5.1 - 5.4 were fit to time series datasets from cells in three buffer compositions (PBS, SFDF, and HEPES), four pulse durations (1, 10, 100, and 1000 μs), and four electric field strengths: 170 (blue), 250 (green), 320 (magenta), and 400 kV/m (orange). Fitting was performed using the Nelder-Mead method to minimize equation 5.6 by varying δ. (d) The best fit δ is shown as a product of electric field strength E_0 and normalized pulse duration $\tau = \sigma_m t/\varepsilon_m$ for all 48 treatment combinations.

electric field strengths experimentally examined, but the time-to-saturation decreased with increasing field strength (Chapter 4). Even though the HEPES buffer has a lower conductivity than the PBS or SFDF by an order of magnitude, δ for the cells in the HEPES buffer is two orders of magnitude larger than for the cells in PBS and SFDF buffers, which are themselves similar (Table 5.1). This more rapid transition rate from the N membrane stage to the M membrane stage results in a larger accumulation M that contributes to a rapid increase in X over the responses evoked by the other buffers (Fig. 5.2). Generally, in each of the primary variables (N, M, X, and U), several characteristic features emerge. For N, the rising edge of the waveform

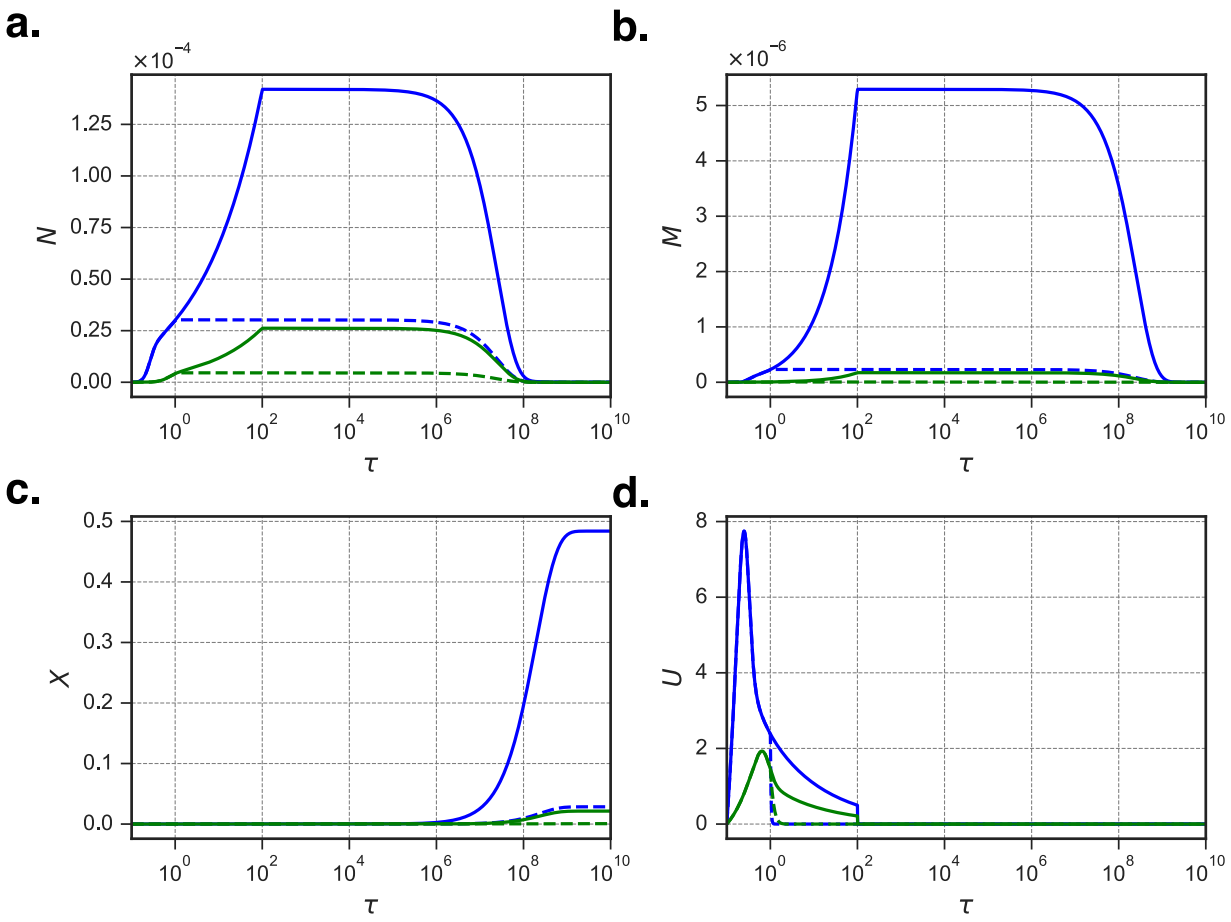

Figure 5.3: Evolution of membrane porosities N and M and the resultant molecular uptake X following an increase in the transmembrane potential U. In each plot, solid lines indicate an applied electric field $t_p = 10$ μs and dashed lines indicate $t_p = 1$ μs. Blue lines indicate a PBS buffer solution and green lines indicate a HEPES buffer. (a) An intact membrane enters a stage conductive of small ions N over time driven by a transmembrane potential $U > 1$. (b) M develops from N, dependent on U, and allows larger molecules to pass through the cell membrane. (c) The intracellular concentration of solute X increases as it enters the cell through the membrane porosity stage M. (d) The transmembrane potential U, driven by a large external electric field, reaches an initial maximum until the membrane begins to shunt ionic currents as N and M increase.

appears biphasic: an initial rapid increase is followed by a more gradual increase until a plateau is reached (Fig. 5.3a). The first phase is where U is the largest. The second phase occurs when the membrane begins to shunt small ionic currents that rapidly decrease U, and slows the increase in N. This progression occurs for cells in each buffer examined in this study, but the cells in HEPES experience a larger N for both the 1 and 10 μs pulses than the cells in PBS experienced at 10 μs.

For M (Fig. 5.3a), a similar biphasic response exists but is more stratified between the 1 and 10 μs pulse

durations for the cells in the HEPES buffer. Interestingly, the 1 μs pulse generated an M for cells in the HEPES buffer similar to that generated by the 10 μs pulse for the cells in PBS. The result of this stratification is apparent in X (Fig. 5.3c). The membrane permeability ($P_m = \xi Mh$) is directly impacted by the M membrane stage and consequently, X depends on both the extracellular-intracellular concentration gradient $(1-X)$ and M. However, while the concentration gradient could limit the molecular uptake as it decreases, $(1-X) > 0.30$ for even the largest pulse strengths and durations examined here. Therefore it is assumed that the changes in M are largely responsible for the molecular uptake observed.

Finally, U experiences a large characteristic increase within 0.5τ to 2τ that is followed by a sharp decline as N and M increase and begin conducting significant ionic currents. For the cells in the HEPES buffer, U achieves a larger magnitude (three- to five-fold) faster than the cells in PBS or SFDF (Fig. 5.3d). This is a surprising result as SFDF and PBS are higher-conductivity buffers than HEPES, and would be expected to conduct more current and allow the cell membrane to charge more rapidly.

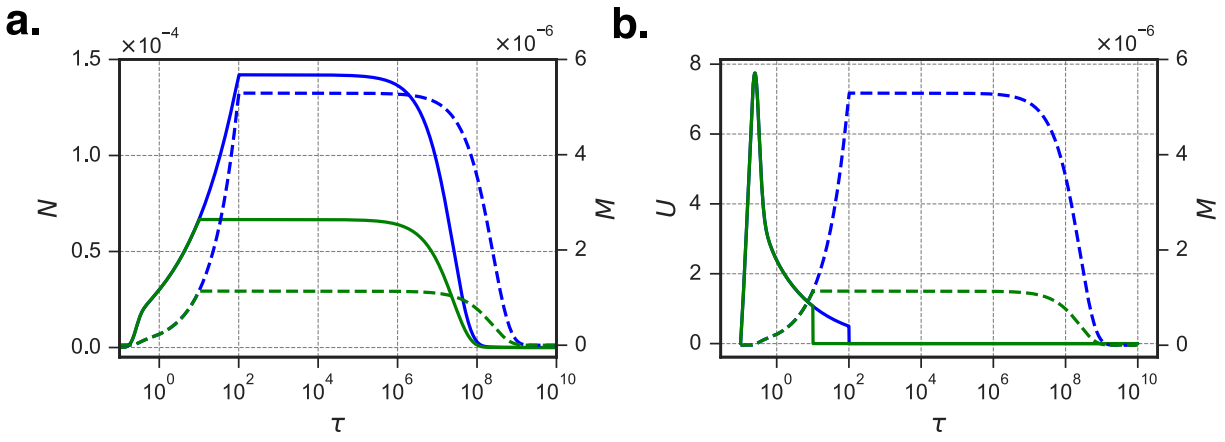

Figure 5.4: The membrane fraction in the M stage persists for longer than the N stage and U. Pulses with durations of 10 (green) and 100 μs (blue) were simulated using $\delta = 1 \times 10^{-3}$. (*a*) A lag exists between when the N stage (*solid lines*) is fully relaxed to 0 and while the M stage (*dashed lines*) persists. (*b*) The transmembrane potential U (*solid lines*) drives the generation of the M stage (*dashed lines*). M plateaus as U goes to 0 upon removal of U_s.

5.3.3 The High-Conductivity Membrane Fraction is Slow to Relax

Prior experimental data have shown that U is highly dynamic during the application of an electric field, but quickly returns to its ground state following the removal of U_s (Fig. 5.3d). However, it is clear that molecular transport across the membrane continues for minutes to hours afterward (Fig. 5.2a-c). This discrepancy between the electrical and transport time scales is motivation to explore the mechanism producing a long-lived M stage membrane fraction. As a large U generates an initial increase in N, a small M begins to develop (Fig. 5.4a). M increases until the removal of U_s, at which point the plateau of M coincides with the return of U to its ground state (Fig. 5.4b). Both M and N persist near their plateau for approximately $10^6\tau$, at which point N begins to relax to the ground state it reaches at $10^8\tau$. However, while N relaxes, M persists until $10^9\tau$. Because the membrane fraction in the M stage is approximately two orders of magnitude smaller than in the N stage, the relaxation of M to N results in a large decrease in the low-conductivity, yet larger, portion of the membrane while the membrane overall continues to be permeable to solutes. This slow relaxation of the M stage is responsible for the difference in time scales between the rapid electrical charging and the relatively slow uptake of solutes in the minutes following EP.

5.3.4 Consecutive Pulses Diminish Permeabilization Efficiency

While multi-pulse experiments can confound observations of membrane dynamics due to the complex cellular response, EP schemes often rely on a series of pulses, rather than a single continuous pulse, to limit Joule heating [16, 276]. $\delta = 1.0 \times 10^{-3}$ was fixed within the range for the PBS buffer, which is commonly used experimentally. Alternating polarity pulses were simulated as ideal square waveforms from 1 to 1000 μs (Fig. 5.5). The inter-pulse delay t_d between the start of the falling edge of one pulse and the start of the rising edge of the following pulse has been implicated in governing cell permeability and death induced by electroporation protocols [217, 219, 277, 278]. In order determine the role of t_d in the induced permeability P_m, simulations were performed using two consecutive pulses at 400 kV/m and varying the delay between the two phases, shown by example for 10 μs pulses (Fig. 5.5a). The induced permeability was evaluated at the beginning of the falling edge of the second pulse for $t_d \in [10^{-6}, 10^{-1}]$ and it was found that t_d within this range does not appreciably affect membrane permeability for 1, 10, 100, and 1000 μs pulses (Fig. 5.5b).

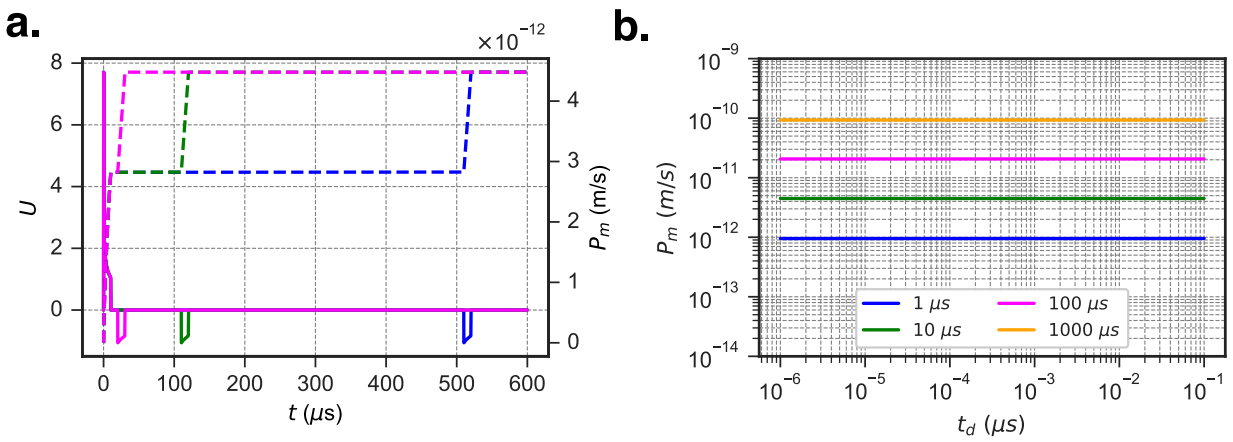

Figure 5.5: Inter-pulse delays of less than 1 ms negligibly impact membrane permeability, while increasing pulse number n and duration t_p increases membrane permeability. (a) The transmembrane potential U response to consecutive, a delay t_d of 1, 100, and 500 μs pulses between opposite polarity pulses 10 μs are shown as solid magenta, green, and blue lines, respectively. The membrane permeability P_m given in m/s is shown as a dotted line corresponding to each waveform. In each case, the membrane permeability increases to approximately the same value at 1 ms following the rising edge of the first pulse in the applied electric field. Pulses are shown with an external electric field of $E_0 = 400$ kV/m. (b) Two consecutive, opposite polarity pulses inter pulse delays of 1-10^5 μs to for pulses with durations t_p of 1, 10, 100, and 1000 μs retain a constant permeability at 1 ms following application of the stimulating electric field. $\delta = 1.0 \times 10^{-3}$ was fixed for both figures.

The impact of the number of consecutive pulses n has been reported as an important factor in membrane conductance changes resulting from electroporation [94, 109, 140]. We refer to the measurement of the effect of the number of pulses on the cell's permeability as the permeabilization efficiency $\Delta P_m(n_i)$ defined as

$$\Delta P_m(n_i) = \frac{P_m(t_i) - P_m((n_{i-1})t_d + n_i t_p)}{P_m(t_i)}, \tag{5.7}$$

where t_i is the time at the start of the i^{th}pulse in a series containing n pulses of duration t_p. Simulations were performed using pulses generated by an external electric field with an amplitude of 400 kV/m and varying the pulse number from 1 to 1000 pulses with durations of 1 to 100 μs. P_m was found to increase proportional to $\sqrt{n}$ for each consecutive pulse delivered (Fig. 5.6a). The central implication of this relationship is that knowing the permeability P_a induced by a single electrical pulse $n_a = 1$ for one PEF waveform a, the number of pulses required to generate and equivalent permeability induced by a second treatment, treatment b, may

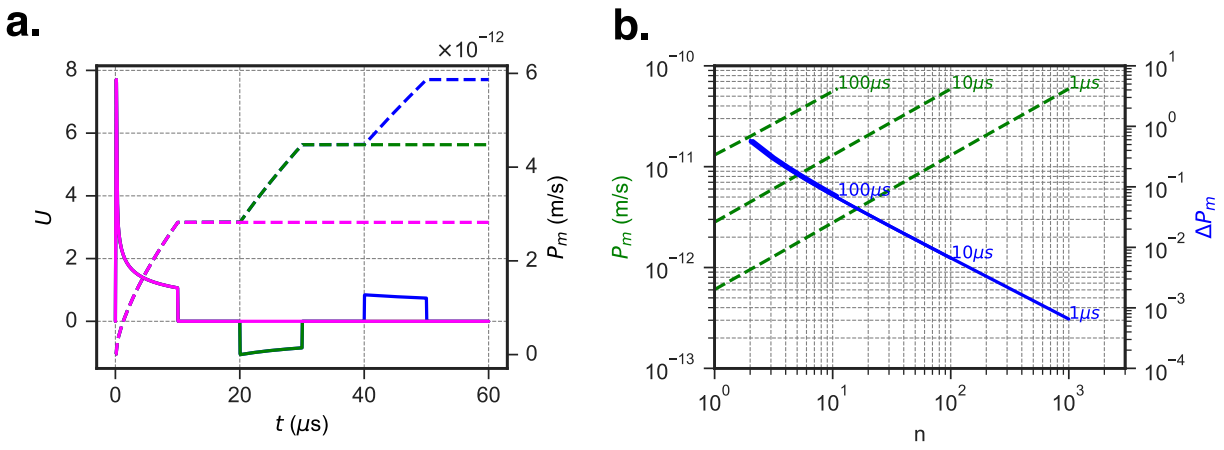

Figure 5.6: Permeabilization efficiency decreases for each consecutive pulse delivered in a given series. (*a*) Alternating polarity pulses increase the transmembrane potential U and generate increasing membrane permeabilities P_m. U is driven by an electric field of $E_0 = 400$ kV/m comprising one, two, or three pulses, shown in magenta, green, and blue, respectively. P_m increases with each consecutive pulse, denoted by the magenta, green, and blue dotted lines identifying the corresponding transmembrane potential. (*b*) The increase in P_m upon removal of the last pulse in a train of n alternating-polarity pulses is shown as green dotted lines for 1, 10, and 100 μs long pulse durations t_p with a 1 μs delay t_d between consecutive pulses. The fractional increase in membrane permeability ΔP_m between the falling edge of two such pulses decreases linearly with $\sqrt{n}$, shown as a blue solid line. $\delta = 1.0 \times 10^{-3}$ was fixed for both figures.

be calculated by

$$\log\left(\frac{n_b}{n_a}\right) = \frac{P_a - P_b}{2}, \tag{5.8}$$

where n_a and n_b are the numbers of alternating polarity pulses in treatment a and b, respectively, and P_a and P_b are the permeabilities after the first pulse of each treatment using constant duration pulses (Fig. 5.6b).

5.4 Discussion

In the proposed model, normalization of the governing equations contains only six parameters: $\{\alpha, \beta, \delta, \eta, \gamma, \xi\}$ (Table 5.1). γ, ξ, and η are the most readily measurable parameters and have been well-characterized and estimated in previous literature [89, 94, 103], while α and β were fixed based on previous estimates [89, 91, 98, 261]. Therefore, we varied δ to calibrate our model to the experimental dataset. Fitting our

model in this way indicated a three- to five-fold difference in the δ for cells treated in the HEPES buffer, over the cells treated in SFDF or PBS (Fig. 5.2). These data indicate that the composition of the HEPES buffer impacts the rate at which M is generated following EP, which is counterintuitive when considering the model in terms of circuit theory. The HEPES buffer has an electrical conductivity 10-fold lower than PBS and SFDF, and should result in a smaller U_s, using a circuit theory approximation. Biochemically, there are two components in the HEPES buffer—HEPES (10 mM) and sucrose (250 mM)—that differentiate this buffer from PBS and SFDF (Chapter 4). HEPES buffers are commonly used for *in vitro* EP studies as they maintain cellular viability without the presence of calcium [30, 279, 280], and the common use of HEPES buffers may suggest that this buffer does not affect cellular EP. Additionally, cells immersed in iso-osmotic sucrose-containing buffers of similar osmolarity, even in the absence of HEPES, have been shown to uptake more propidium than cells in buffers without sucrose [149].

While the impact of HEPES buffers on EP appears to be negligible, there is evidence that the inclusion of sucrose affects cells as they are permeabilized. Sucrose is excluded from electroporated membranes [91] and has been shown to result in the formation of blebs due to the influx of extracellular water through membrane pores [119]. Within the context of these results, the large δ our model predicts for the sucrose-containing HEPES buffer and the influx of water may assist in the widening of membrane pores. The membrane fraction in the low-conductivity N stage could widen into the M stage to more rapidly shunt the flow of water along the osmotic pressure gradient and into the cell. In addition to the widening of pores, the osmotic pressure gradient could also deliver solutes, such as propidium, into the cell more rapidly. Both of these effects may explain the increased δ for cells in HEPES, but more investigation is required to further characterize this mechanism.

The flow of propidium and other solvents into the cell through the cell membrane following EP is the result of both electrophoretic drift and diffusion along concentration gradients. However, the flow of propidium into an electroporated cell following the removal of the applied electric field is largely due to diffusion across pores in the cell membrane [281, 282]. Here, the pore population is divided into two subpopulations, N and M, which are treated in aggregate based upon whether the pores permit propidium transport. Previous reports have suggested subdividing the induced membrane porosity into diffusive and electrically conductive portions [129, 153, 241, 283], but these models have typically relied on the incorporation of interface condi-

tions in continuum models. In our model, the dimensionality of the problem is collapsed through symmetry to yield average porosities for the whole membrane, rather than addressing the generation, relaxation, and interconversion of individual pores (Fig. 5.1). Furthermore, removing this spatial dependance allows our model to be solved using standard ODE solvers, enabling the simplified spatial system to be readily incorporated as a material property into larger systems [284]. In the present model, this reduced dimensionality was achieved through the use of dynamic porosities N and M [106, 153, 241, 285] rather than more conventional pore numbers [13, 286, 287, 288]. The transport through the M stage then facilitates hindered diffusion of propidium into the cell and is represented as an average over the whole cell, rather than at each individual pore, giving rise to a dual-porosity model of the cell membrane [161].

While our two-stage model is calibrated with single-pulse propidium uptake data, further datasets should be considered in future work. However, it can be examined for qualitative consistency with previous reports. The two-stage model can also be easily extended from a single pulse to a series of alternating polarity (Fig. 5.6). Due to the slow relaxation rate (η) of the M stage (Fig. 5.4), two consecutive pulses separated by $\leq$100 ms allow a negligible M to N relaxation prior to the start of a second pulse. The membrane conductance, which most significantly depends on N, is highly dynamic compared to the membrane permeability to solutes, which depends on M (Fig. 5.6a). This is consistent with the relatively rapid recovery of the naive membrane conductance observed in patch-clamp experiments [103]. However, the long-lived M stage results in a P_m that is relatively independent of t_d (Fig. 5.6b). Furthermore P_m, at the removal of each consecutive pulse, increases with $\sqrt{n}$ for up to one thousand 1-10 μs pulses, regardless of the pulse duration (t_p). Our model suggests that two disparate series with different pulse durations and inter-pulse delays generate equivalent permeabilities if the number of pulses in each series satisfies equation 5.8, suggesting a dose-dependent response [289]. Together, these observations are consistent with previous experimental reports using series of long pulses of alternating polarity pulses [94].

The repetition rate (i.e. $1/(t_p + t_d)$) has been observed to impact the uptake of propidium. Repetition rates of 1-10 Hz induce greater permeabilization than pulses delivered more rapidly [277]. Delays of 1 and 4 μs have also been shown to produce relatively similar permeabilities, with longer pulses of equivalent total duration producing even larger permeabilities [94]. In our model, the permeability is dependent only on the membrane fraction in the M stage, which is a small fraction of the total porous area ($M+N$). The preceding

N stage is formed more quickly and relaxes more rapidly than the M stage, which damps the effects of rapid changes in U on M. This damping effect becomes evident when the inter-pulse delay is sufficiently small to allow partial or complete relaxation of the N stage prior to the initiation of the subsequent pulse. Only when a longer pulse is applied can N transition to M and substantially contribute to the membrane's permeability. Furthermore, at longer pulse durations (on the order of several seconds) the membrane fraction in the M stage begins to relax. If the cell membrane in the M stage is allowed to partially relax between pulses, a lower average permeability is obtained over the course of the EP treatment. To design optimal EP protocols, pulse durations must be long enough to induce the largest membrane fraction in the M stage while preventing its relaxation.

5.5 Conclusion

Here, we develop and calibrate a computational model of small molecule transport into cells using only six parameters. We calibrate our model using experimental data of propidium uptake following EP. When extended to multiple bipolar pulses, our model corroborates previous experimental reports and suggests a relationship that defines the pulse number required to obtain equivalent molecular uptake between disparate EP schemes. This model is useful for designing novel pulse schemes and connecting cell-level processes to tissue-level processes with a similar mechanism of action.

5.6 Appendix A: Derivation of Circuit Model

Enforcing current continuity across the membrane gives

$$(\sigma_{mem}\mathbf{E})\cdot\mathbf{n}\big|_{\Gamma} - \varepsilon_m\frac{\partial\mathbf{E}}{\partial t} = 0, \tag{5.9}$$

where $\mathbf{E}$ is the electric field in the source-free membrane interior, ε_m is the permittivity of the cell membrane Γ. The radial component of the electric field has the form $E_r = E_0[(A+Br^{-3})\cos\phi]$ [65]. Let σ_{mem} be the membrane conductivity, σ_{int} be the conductivity of the cell interior, and σ_{ext} be the extracellular conductivity.

The electric current I through the membrane surface of a spherical cell with outer radius r, membrane thickness h, and permittivity ε_m is given by

$$I = -\frac{\pi^2 r^2 (6r-1)}{2h}\left[\sigma_{mem} E_0 - \varepsilon_m \frac{\partial E_0}{\partial t}\right], \tag{5.10}$$

where $A = -1/(2h)$, and $B = 3r^4/h$ for $h << r$, $\sigma_{mem} << \sigma_{int}$, and $\sigma_{mem} << \sigma_{ext}$. By definition, the radially defined electric field is $E_0 = -du/dr$. This allows the electric current between the inside of the cell and the outside of the cell to be integrated to yield

$$\varepsilon_m \frac{\partial U_m}{\partial t} = \sigma_{ext} h E_0 - \sigma_{mem} U_m, \tag{5.11}$$

where $U_m = u_{int} - u_{ext}$, and for a spherical conductor, $I = 4\pi r(r-h)\sigma_{ext} E_0$ where $r >> h$. Two paths were considered for the transmembrane conduction current: through the naive membrane fraction $1-M-N$ and through porous fraction $M+N$ such that $\sigma_{mem} = \sigma_m(1-M-N) + \sigma_p(M+N)$, where σ_{mem} is the effective ionic conductance of the cell membrane, σ_m is the conductance of the naive membrane fraction, and σ_p is the conductance of the porous fraction. Splitting the conductance in this manner yields,

$$\frac{\partial U_m}{\partial \tau} = U_s - U\big(1 + \gamma(M+N)\big), \tag{5.12}$$

where U_m is the unnormalized TMP, $\tau_{RC} = \varepsilon/\sigma_m$, $U = U_m/U_0$, $U_s = \tau_{RC}\sigma_{ext} h E_0/(U_0\varepsilon)$, $\gamma = (\sigma_p - \sigma_m)/\sigma_m$, and σ_{ext} is the conductivity of the external buffer.

5.7 Appendix B: Steady State Analysis

In order to determine the model's steady states, the time derivatives in equations 5.1 - 5.4 were set to zero. Furthermore, because U_s is delivered as a pulse, conditions at the time after its removal are considered as

the initial conditions for a source-free system. This yields the linear system

$$0 = \alpha U^2 - \delta U^2 N - \beta N + \eta M, \tag{5.13}$$

$$0 = \delta U^2 N - \eta M, \tag{5.14}$$

$$0 = \xi M(1-X), \tag{5.15}$$

$$0 = -U\big(1+\gamma(N+M)\big). \tag{5.16}$$

Six possible steady states arise from this system, but the domain constraints $M \geq 0$ and $N \geq 0$ only permit two steady states that reflect the reality

$$(N_1, M_1, X_1, U_1) = (0,0,0,0), \tag{5.17}$$

$$(N_2, M_2, X_2, U_2) = (0,0,1,0). \tag{5.18}$$

To determine the stability of these steady states, all the eigenvalues of the Jacobian must have negative real parts. The Jacobian of equations 5.1 - 5.4 with $U_s = 0$ is

$$J = \begin{bmatrix} -\delta U^2 - \beta & \eta & 0 & 2U(\alpha - \delta N) \\ \delta U^2 & -\eta & 0 & 2\delta UN \\ 0 & \xi(1-X) & -\xi M & 0 \\ -\gamma U & -\gamma U & 0 & -\gamma(N+M) - 1 \end{bmatrix}. \tag{5.19}$$

The eigenvalues are given at steady state s by $det(J|_s - \hat{\lambda} I) = 0$ where $\hat{\lambda}$ are the eigenvalues and I is the identity matrix. This yields the same characteristic equations for both steady states with eigenvalues of $\hat{\lambda} \in \{-1, 0, -\beta, -\eta\}$. $\hat{\lambda} = 0$ arises from equation 5.15, which contains the only appearance of X and its first derivative and has no bearing on any of the other equations in the model. Because this coupling of M to X is unidirectional, equation 5.15 and derivatives with respect to X were removed from J. $\hat{\lambda}$ was recalculated and yielded $\hat{\lambda} \in \{-1, -\beta, -\eta\}$. Because all of the real parts of the eigenvalues are negative, the system coupling N, M, and U is asymptotically stable.

5.8 Appendix C: ODE Simulation Code

The following code fits the dynamical system model of single-cell electroporation in the preceding chapter to experimental data generated in Chapter 4. For each medium (PBS, SFDF, and HEPES), for each position within the chamber corresponding to a different electric field strength (1:170 kV/m, 2:250 kV/m; 3:320 kV/m, 4:400 kV/m) and each pulse duration (1, 10, 100, and 1000 μs), a data file containing mean fluorescence intensity values listed at each time point for each cell is read into the script and converted to a concentration using the proportionality constant (`CON`). The applied electric field is converted into a source transmembrane potential and each parameter in the model is defined. The model is fit to the experimental data using a Nelder-Mead method implemented in the `minimize` function. The fit parameters stored after each iteration are then saved as a CSV file (`paramterFits.csv`).

```
import pickle, os, time, datetime, lmfit
import numpy as np
from lmfit import Parameters, minimize
from scipy.integrate import odeint

## Constant relating pixel value to concentration
CON = (2**16-1)/695.37*(1/668.3964*1e3*1e-6)

## Open data file
def openFile(dirname, pos, pulse, params, CONSTANT=CON,
             extension='.csv', return_raw=False, medium='PBS',
               ↪ X0=30e-6):
    t = []
    C = []
    # start_time = time.time()
    for i in os.listdir(dirname):
        test1 = extension in i and 'pos%s_'%pos in i
        test2 = 'pulse%s.'%pulse in i and medium in i
        if test1 and test2:
            with open(dirname + '/' + i) as fline:
                for line in fline:
                    if line[0] != 'c':
                        xd = [CONSTANT*np.float(i) for i in
                          ↪ line.split(',')[1:-1]]
                        C.append(xd)
    Cm = np.median(C, axis=0)
    Cm = np.subtract(Cm, Cm[0])
    Cm = np.divide(Cm, X0)
```

```
27
28      Cs = np.std(C, axis=0)/np.sqrt(len(C))
29      Cs = np.divide(Cs, X0)
30      t = np.linspace(0, 60*len(Cm), len(Cm)) #time in microseconds
31      if return_raw:
32          return [t, Cm, Cs]
33      else:
34          return[t, Cm, Cs]
35
36  ## ODE model
37  def odeModel(state, t, params, waveform=None):
38      N = state[0]
39      M = state[1]
40      U = state[2]
41      X = state[3]
42      alpha = params['alpha'].value
43      beta = params['beta'].value
44      delta = params['delta'].value
45      eta = params['eta'].value
46      gamma = params['gamma'].value
47      xi = params['xi'].value
48      tau = params['tau'].value
49      if waveform == None:
50          tp = params['tp'].value
51          if t < tp:
52              U0 = params['U0'].value
53          else:
54              U0 = 0
55      elif waveform == 'bipolar':
56          tp = params['tp'].value
57          delay = params['delay'].value
58          time_resid = np.mod(t, tp+delay)
59          total_num = params['pulse_no'].value
60          num = int(t/(tp+delay))
61          if is_odd(num) and num < total_num:
62              if time_resid < tp:
63                  U0 = -1*params['U0'].value
64              else:
65                  U0 = 0
66          elif not is_odd(num) and num < total_num:
67              if time_resid < tp:
68                  U0 = params['U0'].value
69              else:
70                  U0 = 0
71          else:
72              U0 = 0
73      eq1 = alpha*(1-N-M)*(U**2) - beta*N - delta*N*U**2 + eta*M
74      eq2 = delta*N*U**2 - eta*M
```

```
    eq3 = U0 - (gamma*(N+M) + 1)*U/tau
    eq4 = xi*M*(1-X)
    return [eq1, eq2, eq3, eq4]

## ODE solver
def solveODE(time, params, state0, waveform=None):
    params['tp'].value = params['tp'].value
    t = time
    sol = odeint(odeModel, state0, t, args=(params, waveform),
                 mxstep=int(1e6), h0=1e-9, atol=1e-9, rtol=1e-9)
    return sol

## Calculate residual
def residual(params, state0, pulse, pos, obs_data, V0):
    resid = []
    s = []
    data = obs_data
    params['tp'].value = pulse*1e-6
    params['U0'].value = V0[pos-1]
    t = data[0]
    sol = odeint(odeModel, state0, t, args=(params,), mxstep=int(1e6),
                           h0=1e-12,
                           atol=1e-9, rtol=1e-9)
    resid = abs(sol[:,-1]-data[1])
    s = data[-1]
    params['SSR'].value = np.sum(np.multiply(resid,
                resid))/sum(np.multiply(data[1],
                  ↪ data[1]))/len(data[1])
    return resid, s

## Dump parameter fits to output file
def prettyDump(paramsets, filename):
    f = open(filename, 'w')
    f.write(','.join([i for i in paramsets[0].keys()])+'\n')
    for j in paramsets:
        f.write(','.join([str(j[i].value) for i in j.keys()])+'\n')
    f.close()
    return False

## Simulation constants
R = 7.5e-6
eps0 = 8.85e-12
eps = 12*eps0
Uep = 0.258
h = 5e-9
sigma_e = 1;
E0 = [170e3, 250e3, 320e3, 400e3]

```

```
## Initial Condition
state0 = [0, 0, 0, 0]
filename = os.curdir + '/dataFit'

## Buffer types
MED = ['PBS', 'SFDF', 'HEPES']
conductivities = {'PBS':1.01,
                  'SFDF':0.93,
                  'HEPES':0.08}

## Loop over buffer types
for medium in MED:
    V0 = np.multiply(E0, conductivities[medium]*h/(eps*Uep))
    pulse = [1, 10, 100, 1000]
    pos = [1, 2, 3, 4]
    start_time = time.time()
    params0 = Parameters()

    ## Define parameter space for simulation
    params0.add('alpha', value=1, vary=False)
    params0.add('beta', value=4e-2, vary=False)
    params0.add('delta', value=5e1, min=5e-1, max=5e2) #adjust height
    params0.add('eta', value=4e-3, min=1e-4, max=1e-1) #adjust height
    params0.add('gamma', value=1e5, vary=False)
    params0.add('xi', value=5e2, vary=False)
    params0.add('tau', value=1e-6, vary=False)
    params0.add('tp', value=pulse[-1], vary=False) # solve in
      ↪ microseconds
    params0.add('U0', value=V0[-1], vary=False)#
    params0.add('SSR', value=0)
    params0.add('conductivity', value=conductivities[medium],
      ↪ vary=False)
    paramsets = []

    ## Loop over pulse durations
    for i in pulse:

        ## Loop over pulse strengths
        for j in pos:
            print("\n[+] Optimizing initial
              ↪ parameters...(Nelder-Mead)")
            params = params0
            params['U0'].value = V0[j-1]
            params['tp'].value = i
            data = openFile(filename, j, i, params, medium=medium)
            mi = minimize(residual, params,
                    args=(state0, i, j, data, V0), method='nelder')
            paramsets.append(mi.params)
```

```
167
168 ## Store output file with parameter fits
169 prettyDump(paramsets, 'parameterFits.csv'%medium)
```

Chapter 6

Discontinuous Galerkin Model of Cellular Electroporation

Daniel C. Sweeney[a*] and Rafael V. Davalos[a*]

[a] Department of Biomedical Engineering and Mechanics, Virginia Tech, Blacksburg, VA, USA

* Corresponding author

Author Contributions

DCS designed and performed the experimental portion of this work, analyzed the results, and wrote and edited the manuscript. RVD conceived of the research and edited the manuscript.

Manuscript in review

6.1 Introduction

Electroporation is a biophysical process in which an applied electric field motivates the rearrangement of the constituent phospholipids of a bilayer membrane to form metastable pore-like structures [12, 102, 107]. The formation of these electropores results in a large increase membrane permeability to plasmids and small molecules, such as drugs and fluorescent tracers [14, 146, 204]. Chemotherapeutics in particular are able to more readily pass through the membranes of electroporated cells, increasing their efficacy when delivered alongside electroporation treatments [35]. These electrochemotherapies have combined electroporation with bleomycin [200], cisplatin [290, 291], and most recently calcium [32] to successfully treat tumors. If the applied electric field is sufficiently strong and applied over enough time, electroporation may also be used directly as an effective tumor ablation modality [16]. These irreversible electroporation treatments have been successfully used to locally treat tumors in the liver [292], prostate [293], and brain [17].

Mechanistically, electroporation relies on the generation of nano-scale pores that permit the flow of solute molecules between the aqueous interior and exterior of a cell. Pore formation has been modeled using the asymptotic Smoluchowski model (ASM), which considers the process similar to a nucleation event [75, 168]. Pores are assumed to appear with an initial sub-nanometer radius and then expand based on steric hindrance, electrical energy, surface tension of the membrane, and the line tension of the pore itself [13]. Computational studies of the evolution of pores radii identify at least two populations of pores generated by electroporation [110, 111, 161], with some models considering three of four [283]. The first subpopulation is characterized by a 0.8 nm radius. The second subpopulation has a characteristic radius of 10 to 30 nm and are fewer in number than the first [102, 111]. Dynamical system models of pore formation have been implemented on the cell membrane to reconcile these observations and mitigate computational complexity [153, 183] (Chapter 5). In these models, the transitions from naive membrane to small pore and from small pore to large pore are characterized in aggregate by forward and reverse rate constants which significantly decreases the computational cost over tracking each pore individually.

Pores are generated simultaneously with electrodiffusive processes that vary the local ion concentrations around the cell. The electrical conductivities of the intracellular and extracellular spaces are much greater than their permittivities to the degree that these domains are often considered ohmic [82, 144]. Electrical flux continuity couples the intracellular and extracellular potential and concentration fields across the thin, semi-

permeable, dielectric membrane. As pores are formed, they shunt ionic currents through the membrane, which decreases the transmembrane potential (TMP) [263, 294]. These ionic fluxes are also subject to both electrical drift and diffusion [262, 295].

Finite element and finite volume methods have been implemented to spatially discretize the solution domain in drift-diffusion problems involving charged particles in and around a cell during electroporation [144, 262]. In such schemes, two major domains are considered: the intracellular space and the extracellular space. Finite element methods rely on a mesh which subdivides the whole domain into an ensemble of coupled smaller domains over which the governing equations are applied. The membrane interface between these two domains is considered negligibly thin and couples these two domains using Robin boundary conditions [82, 296]. One particular class of finite element methods, called discontinuous Galerkin finite element methods, is particularly useful for handling flux jumps across thin interfaces. These methods introduce additional degrees of freedom to penalize differences between the solution values on element facets that that share an interface [297, 298]. In the symmetric interior penalty discontinuous Galerkin (SIPDG) formulation, penalty terms and terms to make the assembled system symmetric are added [299]. At the expense of additional degrees of freedom, these methods directly account for flux jumps between interfacial elements within the formulation itself. In addition, discontinuous Galerkin finite element methods methods are able to be implemented using parallel solvers, enabling them to be readily integrated into high performance computing schemes.

Here, we report the development of a two-dimensional axisymmetric model of electroporation on a single fitted mesh using the SIPDG method. To our knowledge, this is the first model to integrate ASM-based pore formation with a two-stage permeability scheme and the drift-diffusion of charged solutes using a SIPDG finite element method. The results of our model are in strong agreement with previous modeling efforts and experimental reports. Our SIPDG model of the biophysical mechanisms motivating electroporation will enable future computational investigations.

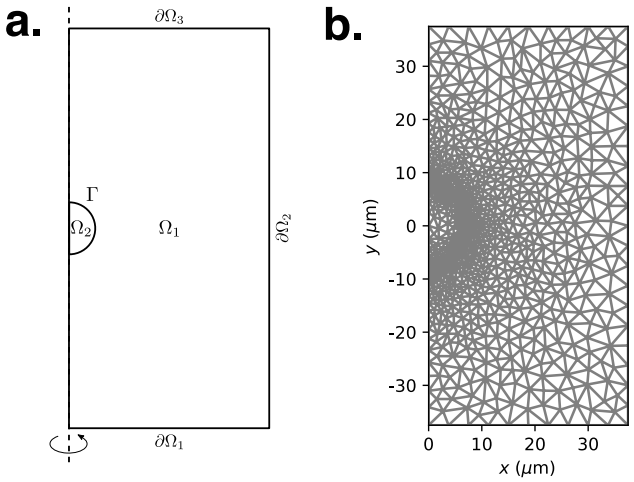

Figure 6.1: A cell was modeled as a 2D axisymmetric sphere. (a) Diagram of the model geometry where the left side of the geometry is collinear with the axis of symmetry. (b) The 75 μm $\times$ 37.5 μm triangular mesh included 1612 elements that range in diameter from 5.0×10^{-6} μm to 6.7×10^{-7} μm.

6.2 Methods

6.2.1 Drift-Diffusion Model

Computational models of electroporation often consider an idealized spherical cell modeled as a thin dielectric boundary Γ separating an external conductive domain (Ω_1) from an internal conductive domain (Ω_2) such that $\Omega_1 \cup \Omega_2 = \Omega$ (Fig. 6.1a). The boundaries of the global domain $\partial\Omega$ are either Neumann non-conducting boundaries or Dirichlet boundaries to which electric potentials or solute concentrations are assigned. The drift-diffusion component of a boundary value problem modeling single-cell electroporation involves the solution of the transient Nernst-Planck equation

$$\frac{\partial c_i}{\partial t} - \nabla \cdot \mathbf{J} = 0, \tag{6.1}$$

on Ω where $\mathbf{J} = D_i \nabla c_i + \mu_i c_i \nabla u$, D_i is the diffusion coefficient of solute i with charge number z_i at concentration c_i, and u is the electric potential field. μ_i is the electrical mobility of solute i and is given by the Einstein relation $\mu_i = D_i F z_i/(RT)$ where F is Faraday's constant, R is the universal gas constant, and T is the ambient temperature. A Dirichlet boundary condition is imposed on $\partial\Omega_2$ by $c_i|_{\partial\Omega_2} = c_D$. On $\partial\Omega_1$ and $\partial\Omega_3$, no-flux Neumann boundary conditions were imposed ($\mathbf{J} \cdot \mathbf{n}|_{\partial\Omega_1} = \mathbf{J} \cdot \mathbf{n}|_{\partial\Omega_1} = 0$). The initial condition was set to $c_i|_{\Omega_1} = c_D$ and $c_i|_{\Omega_2} = 0.0$.

The mass transport flux jump interfacial condition on Γ is described by a membrane permeability to solute i

(P_i)

$$\{\mathbf{J}\}\big|_{\Gamma} = P_i[[c_i]], \tag{6.2}$$

where the $[[\cdot]]$ and $\{\cdot\}$ are operators defined on the facets of elements for an arbitrary function φ

$$[[\varphi]] := \varphi^{+}\mathbf{n}^{+} + \varphi^{-}\mathbf{n}^{-}, \tag{6.3}$$

$$\{\varphi\} := \frac{1}{2}(\varphi^{+} + \varphi^{-}). \tag{6.4}$$

Membrane permeability to solute i (P_i) was modeled under the assumptions of electrodiffusive transport

$$P_i = \frac{D_i}{h}\left(\frac{Pe}{e^{Pe}-1}\right)(\pi r_0^2 HN + \chi_M M) \tag{6.5}$$

where H is the hindrance factor [161], χ_M is the effective relative permeability of the M-stage membrane, and N is the surface pore density of pores.

The discontinuous Galerkin formulation is developed by allowing the mass flux to be discontinuous between adjacent elements on their shared interface. We build on the work of [298, 299, 300] and apply the SIPDG method on each element $k \in T$ where T is a subdivision of Ω of k elements, which yields

$$\begin{aligned}
\sum_{k\in T}\int_T v\left(\frac{\partial c_i}{\partial t}\right)dx + \sum_{k\in T}\int_{T_k}\nabla v\cdot\mathbf{J}\,dx \\
- \sum_{k\in T}\int_{\partial T_k\setminus\Gamma}\{\mathbf{J}\}\cdot[[v]]\,ds - \sum_{k\in T}\int_{\partial T_k\setminus\Gamma_k}\{\nabla v\}\cdot[[c_i]]\,ds \\
+ \sum_{k\in T}\int_{\partial T_k\setminus\Gamma_k}\frac{\alpha}{h_k}[[c_i]]\cdot[[v]]\,ds - \sum_{k\in\partial\Omega_D}\int_{\partial\Omega_k}\mathbf{J}\cdot v\mathbf{n}\,ds \\
+ \sum_{k\in\partial\Omega_D}\int_{\partial\Omega_k}\frac{\alpha}{h_k}v(c_i-c_D)\,ds - \sum_{k\in\partial\Omega_D}\int_{\partial\Omega_k}v(c_i-c_D)\,ds \\
+ \sum_{k\in\Gamma}\int_{\Gamma_k}P_i[[c_i]]\cdot[[v]]\,ds = 0,
\end{aligned} \tag{6.6}$$

where v is a test function, h_k is the circumradius of element k and α is any sufficiently large positive function.

The propagation of an applied electric field is given by the Poisson equation

$$-\nabla \cdot (\sigma \nabla u) = 0, \tag{6.7}$$

where σ is the conductivity. However, as the extracellular (Ω_1) and intracellular (Ω_2) domains are considered purely ohmic, the source term is only considered on the membrane facets (Γ). The Dirichlet boundary conditions generate the applied electric field and are imposed on $\partial\Omega_1$ and $\partial\Omega_3$ by $u|_{\partial\Omega_1} = -u|_{\partial\Omega_3} = E_0 l_0/2$ where l_0 is the vertical length of the axisymmetric computational domain ($l_0 = 75$ μm). On $\partial\Omega_2$, a no-flux boundary was imposed ($-\sigma\nabla u \cdot \mathbf{n}|_{\partial\Omega_2} = 0$). The initial condition was set to $u = 0.0$. The interfacial electrical flux condition on Γ describes displacement and ionic conduction currents through the dielectric membrane

$$\{\sigma_i \nabla u_i\}\big|_\Gamma = \left(\frac{\varepsilon_m}{h}\right)\left(\frac{\partial [[u]]}{\partial t}\right) + \frac{\sigma_m}{h}([[u]] + u_{rest}) + G_i[[u]], \tag{6.8}$$

where ε_m is the permittivity of the cell membrane, h is the membrane thickness u_0 is the resting membrane potential, σ_m is the naive membrane conductivity, and G_i is the ionic conduction current through electropores. The formulation of G_i is similar to P_i

$$G_i = \frac{2\pi r_0^2 \sigma_{eff} N}{\pi r_0 + 2h} \tag{6.9}$$

where $\sigma_{eff} = (\sigma_{ext} - \sigma_{int})/\log(\sigma_{ext}/\sigma_{int})$, $\log(\cdot)$ is the natural logarithm, σ_{ext} is the conductivity of the extracellular space (Ω_1), and σ_{int} is the conductivity of the intracellular space (Ω_2).

The SIPDG formulation for u is similar to the mass transport formulation and is given by

$$\sum_{k\in T}\int_{T_k}\nabla w\cdot\sigma\nabla u\,dx-\sum_{k\in T}\int_{\partial T_k\setminus\Gamma}\{\sigma\nabla u\}\cdot[[w]]\,ds-\sum_{k\in T}\int_{\partial T_k\setminus\Gamma_k}\{\nabla w\}\cdot\sigma[[u]]\,ds$$
$$+\sum_{k\in T}\int_{\partial T_k\setminus\Gamma_k}\frac{\alpha}{h_k}[[u]]\cdot[[w]]\,ds-\sum_{k\in\partial\Omega_D}\int_{\partial\Omega_k}\sigma\nabla u\cdot w\mathbf{n}\,ds$$
$$+\sum_{k\in\partial\Omega_D}\int_{\partial\Omega_k}\frac{\alpha}{h_k}w(u-u_0)\,ds-\sum_{k\in\partial\Omega_D}\int_{\partial\Omega_k}w(u-u_0)\,ds$$
$$+\sum_{k\in\Gamma}\int_{\Gamma_k}\frac{\varepsilon_m}{h}[[w]]\cdot\left(\frac{\partial[[u]]}{\partial t}\right)ds+\sum_{k\in\Gamma}\int_{\Gamma_k}\frac{\sigma_m}{h}[[w]]\cdot([[u]]+u_{rest})\,ds$$
$$+\sum_{k\in\Gamma}\int_{\Gamma_k}G_i[[w]]\cdot[[u]]\,ds,=0. \quad (6.10)$$

where w is a test function. Further details are given in Appendix A.

Parameter	Value	Units	Description	Reference
α	10		Stabilization parameter	
ε_0	8.9×10^{-12}	F/m	Vacuum permittivity	
F	9.6×10^{4}	C/mol	Faraday constant	
R	8.3	J/mol·K	Universal gas constant	
T	300	K	Ambient temperature	
E_0	1.0	MV/m	Applied electric field strength	
z_i	+2		Propidium charge number	[136]
D_i	0.5×10^{-9}	m^2/s	Propidium diffusion coefficient	[136]
σ_{ext}	1.0	S/m	Extracellular conductivity	Chapter 4
ε_m	$8.0\varepsilon_0$		Membrane permittivity	[301, 302]
σ_m	1.0×10^{-8}	S/m	Naive membrane conductance	[82, 302]
σ_{int}	0.3	S/m	Intracellular conductivity	[303]
ρ	10	μm	Cell radius	[81, 304]
h	5.0	nm	Membrane thickness	[82, 305]
r_0	0.8	nm	N-stage pore radius	[102, 111]
r_L	10	nm	M-stage pore radius	[111]
a	1.0×10^{9}	m^{-2}/s	Pore creation rate	[82]
N_{eq}	1.5×10^{9}	m^{-2}	Equilibrium pore density	[82]
k_0	1.0×10^{8}	1/s	M formation rate	[103]
k_m	4.0×10^{-3}	1/s	M recovery rate	[85, 103]
u_{th}	260	mV	Electroporation threshold voltage	[82, 103]
u_{rest}	70	mV	Electroporation threshold voltage	[60, 306]
λ_M	0.63		Solute radius / pore radius	[161]
k_n	1.0×10^{5}	M	Michaelis constant	
χ_M	1.0×10^{4}		M fraction area	

Table 6.1: Parameters for discontinuous Galerkin finite element model of electroporation

6.2.2 Pore Generation and Secondary Membrane Permeability

The generation of electropores is modeled using the ASM

$$\frac{\partial N}{\partial t} = a e^{([[u]]/u_{th})^2}\left(1 - \frac{N}{N_{eq} e^{-q([[u]]/u_{th})^2}}\right), \tag{6.11}$$

where a is the pore formation rate, u_{th} is the electroporation threshold, N_{eq} is the equilibrium pore density, and q is a fitting constant. Radical oxygen species are generated during electroporation and have been shown to damage the cell membrane [307, 308], suggesting the existence of a secondary transport mechanism. Hence, a sensitized membrane fraction (M) was introduced into the model. M formation occurs with a maximum rate k_0 and has a dependence on the pore population density. The growing surface concentrations pores increasingly contributes to the disruption of the naive membrane, modeled as

$$\frac{\partial M}{\partial t} = \frac{k_0 N(1-M)}{k_n + N} - k_m M \tag{6.12}$$

where k_n corresponds to the N at which the half-maximum M formation rate is achieved and k_m is the recovery rate of the sensitized membrane fraction.

6.2.3 Implementation

Computations were performed using the FEniCS (v2017.2) FE framework [309] in Python (v3.6.3). The 2D axisymmetric geometry was generated in GMSH (v3.0.1) and included the element with the smallest ratio of major to minor circumradius of 0.66 and the element with the largest ratio of 1.0 (Fig. 6.1). An implicit backward Euler scheme was used to solve equation 6.6 for c_i and equation 6.10 for u. The computational electroporation model proceeded using an implicit time stepping scheme for temporal discretization and a SIPDG method for spatial discretization. Solution of equations 6.6 and 6.10 was performed using the potential field (u), pore (N) and solute distributions (c_i) from the previous time step. The pore surface density following this update was calculated on Γ using an implicit midpoint scheme. Masking the facets on Γ was necessary to the computational scheme because of the interface and Dirichlet boundary conditions are enforced as interior penalties on the boundary facets ($\partial\Omega$) as described (Appendix A). This was done prior

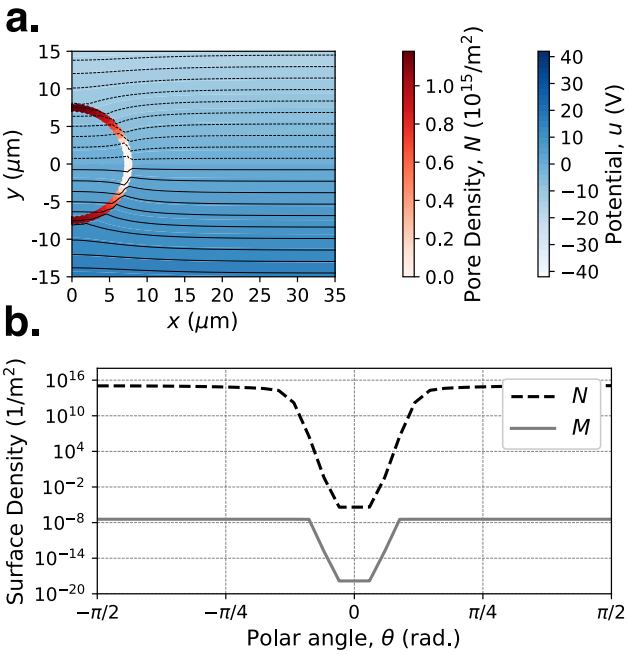

Figure 6.2: The transmembrane potential ($[[u]]|_\Gamma$) drives the formation of pores and sensitized membrane. (*a*) The transmembrane potential is shown following a single 1 μs pulse. (*b*) The surface pore density N and sensitized membrane fraction M are shown as functions of the polar angle θ along the cell membrane Γ.

to the N update by multiplying $[[u]]$ by a 0-order piecewise constant masking function defined as unity on the elements bordering Γ and 0 everywhere else. These updated values were then used to repeat the process for the next time step. Simulations were performed both on a MacBook Pro (Mid 2012) with a 2.5 GHz Intel i5 processor and 16 GB of RAM. Data visualization and post-processing were performed in both Matplotlib (v2.2.1) and ParaView (5.4.0).

6.3 Results

An electric field around the model cell was applied at $t = 0$. The cell locally distorts the electric field as it develops due to its low conductivity membrane (Fig. 6.2). As the TMP ($|[[u]]|_\Gamma$) increases, pores are generated along the cell membrane where $[[u]]|_\Gamma > u_{th}$. This variation in conductance results in a deviation of the model from the Schwan model [310] (Fig. 6.3).

Once formed, these pores disrupt the membrane leading to secondary membrane permeabilization (M), which allows tracer molecules, such as propidium, to enter the cell. Once pore formation occurs, TMP sigmoid flattens at the extreme anodic and cathodic poles (Fig. 6.3). This nonlinearity is caused by ionic currents through pores shunting larger currents to inhibit TMP increases. Our model predicts that for a 1.0 MV/m electric field, the TMP will reach a maximum much larger than the electroporation threshold

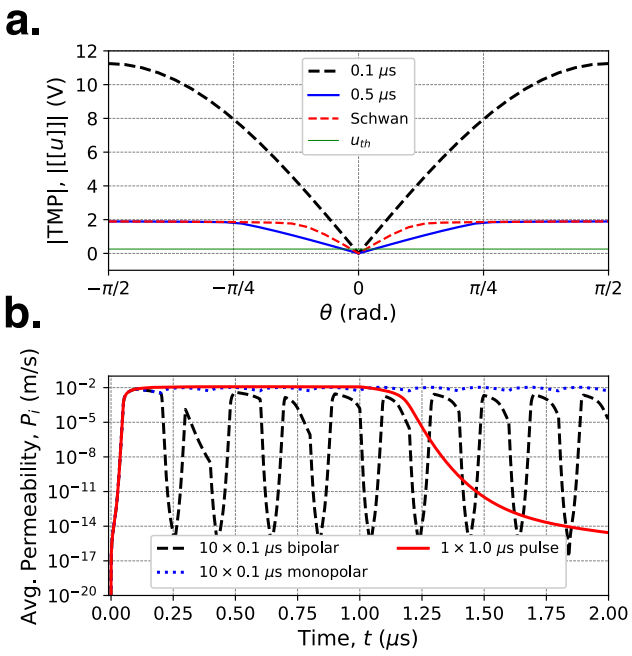

Figure 6.3: The transmembrane potential (TMP) deviates from the ideal, non-electroporated behavior due to membrane permeabilization. (*a*) The absolute value of the TMP ($|[[u]]|$) by seven-fold at the cell poles from the idealized behavior predicted by the Schwan equation. (*b*) TMP deviates as the membrane permeability increases during PEF application. The permeability reaches a relatively constant plateau for a long pulse and 0.1 μs monopolar pulses, but varies considerably with bipolar pulses.

(u_{th}) after 1 μs (Fig. 6.3a). Further, our model shows that a monopolar pulse train can induce an average permeability for the whole membrane similar to that generated by a contiguous pulse (Fig. 6.3b). In order to investigate the effects of periodic pulsed electric fields, multiple idealized square pulses were simulated through varying the Dirichlet boundary conditions for u on $\partial\Omega_1$ and $\partial\Omega_3$. Monopolar and bipolar pulses with 0.1 μs durations were applied with 0.1 μs delays between consecutive pulses of opposite polarities in addition to a 1 μs pulse. Each treatment had an equivalent energized time. The solute flux across the cell membrane was observed to be asymmetric for the single 1 μs pulse and the ten 0.1 μs monopolar pulse treatments (Fig. 6.4a). However, by alternating the polarity of the 0.1 μs pulses (bipolar), this asymmetry was greatly diminished at the cost of an overall decrease in c_i uptake. The 1 μs contiguous pulse produced the largest increase in intracellular c_i, followed by the monopolar, then bipolar pulses (Fig. 6.4b). This enhancement becomes increasingly evident as additional pulses are delivered. However, as the reversal of the boundary conditions discharges the TMP in a bipolar pulse train, the average membrane permeability oscillates around a significantly lower value, and the advantage of dispersing the pulses in the treatment train is lost.

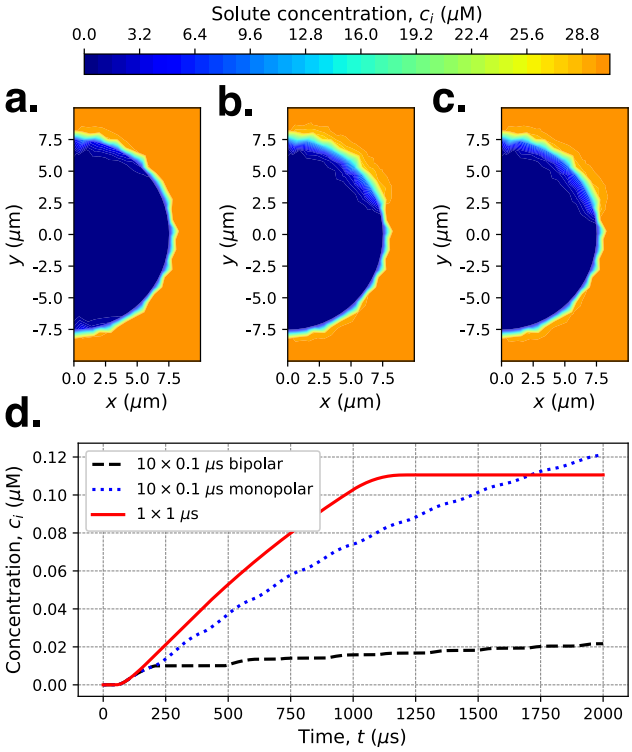

Figure 6.4: Long pulses and monopolar trains of pulses induce greater molecular uptake than bipolar pulses. (*a*) A train of ten 0.1 μs bipolar electrical pulses (0.1 μs inter-pulse delay) induces a more symmetric solute uptake than (*b*) a train of ten 0.1 μs bipolar electrical pulses or (*c*) a single continuous 1 μs pulse. (d) The average intracellular solute concentration c_i is approximately eight-fold greater for the monopolar pulse train and the long single pulse than the bipolar pulse train.

6.4 Discussion

The computational results presented here are in good agreement with previous experimental and computational efforts. For example, the membrane permeabilities predicted by our SIPDG model are consistent with previous observations, 6.7×10^{-9} to 1.3×10^{-8} m/s for electric field strengths of 200 to 400 kV/m and pulse durations of 20 to 1000 μs [89] (Chapter 5). Our model predicts an average permeability of 4.5×10^{-7} m/s is produced by a 1 μs pulse at 1.0 MV/m, which is larger than what has been experimentally observed, but of a similar order of magnitude. However, it is noted that these data are observed in the minutes following application of the electrical pulse and the initial large permeability will most likely decrease prior to the time of the first experimental observations (Chapter 5).

While the average permeability plausibly reflects experimental measurements, the resealing rate of the membrane observed experimentally is not at present faithfully recapitulated by the SIPDG model using the ASM to model pore formation. Experimental reports of pore resealing rates on the order of several hundred seconds [85, 89, 102, 103, 118] while the ASM predicts that pores relax on the order of tens to hundreds of nanoseconds [13]. Several hypotheses have been proposed to explain this discrepancy including long-lived pores and membrane oxidation. According to the long-lived pore hypothesis, a small fraction of the total

pore population is maintained in the membrane following removal of the applied electric field [110]. This subpopulation enables the membrane to remain largely permeable in the minutes to hours following electroporation [85, 89, 94, 146, 147, 294] (Chapter 5). Alternatively, the membrane oxidation hypothesis posits that while electropores may form, they rapidly reseal and a secondary oxidation mechanism is responsible for the sustained permeability following electroporation. Lipid oxidation has been experimentally shown to affect membrane permeability [307, 311, 312, 313], though the mechanisms themselves are still opaque. The reaction scheme we implement for pore expansion is general at present and more data will be needed to characterize prolonged cellular permeability following electroporation.

Multi-pulse PEF schemes are typically implemented in order to perform electroporation while mitigating thermal damage [132, 314]. However, the impact of consecutive pulses and the delays between them confounds direct experimental observation. Computational models, such as our SIPDG model, are particularly well-suited to examine membrane electrodynamics at these time scales. Our simulations indicate that there exists a large difference in the membrane permeability induced by trains of monopolar pulse and trains of bipolar pulses with equivalent energized times. Monopolar pulses polarize the membrane in the same orientation with each consecutive pulse. When the TMP is not allowed sufficient time to discharge completely between two consecutive pulses, the electropores from the previous pulse provide a larger baseline for the generation and expansion of new pores, rather than starting from a naive or oppositely-polarized membrane state. Because bipolar electroporation schemes must discharge the membrane before repolarizing it in the opposite direction, monopolar pulses elicit a much larger permeability (Fig. 6.4).

The present SIPDG model provides an elegant method for handling the flux jumps arising from the cell membrane during electroporation while maintaining consistency with previous computational efforts and experimental reports. Discontinuous Galerkin finite element models of membrane charging by an external electric field [298] and of mass transport through semipermeable membranes [299] have also been implemented. A variety of methods have also been used to model cellular electroporation. A finite volume method has been implemented to solve a model of charged particle drift-diffusion during electroporation [144]. A transport lattice model involving discrete electrical components has been implemented to model membrane charging and pore formation [296]. Similar work using enriched finite difference schemes have been implemented using heuristic two-state pore formation models, though not considering biophysical mechanisms

[184]. The membrane interface has been enriched with flux discontinuities to explicitly enforce membrane charging, pore formation, and charged particle drift-diffusion. These methods consider the intracellular and extracellular domains continuous [183]. However, finite element methods comprise the most widely implemented frameworks for electroporation model development [153, 182, 262].

Computationally, the present model builds on these efforts to implement a SIPDG model of electroporation that includes the nonlinear ASM to account for pore formation. Finite element methods are especially suited for handling complex geometries and boundary conditions in multiple dimensions [50, 109]. In addition to mesh refinement, higher-order shape functions may be used to refine a solution. Computational domains are also readily extended from one to two to three dimensions with few changes required by solver algorithms, allowing for the development of robust application code. One particular benefit to using discontinuous Galerkin finite element methods is their potential to be solved in parallel on high performance computing clusters [309]. By only requiring local support for each element, the assembly and the solution of the system may be distributed over many computational nodes rather than formulated as a serial process [298]. The flexibility of the SIPDG method enables biophysical processes such as membrane pore formation and radial pore expansion to be easily manipulated through the addition or deletion of integrals in the finite element formulation. Here, we have designed our SIPDG model to be readily extended to such schemes in future models, though the implementation itself is outside the scope of the present work.

6.5 Conclusion

Here, we report the development of a model of electroporation based on the symmetric interior penalty discontinuous Galerkin finite element method. We demonstrate that our model predicts membrane permeabilities consistent with previous computational models and experimental data. Our model predicts that an assisted discharge mechanism is responsible for the difference in monopolar and bipolar PEF schemes with equivalent energized times. The SIPDG model we develop will be critical to future computational investigations into long-lived membrane permeability and is readily extensible for use on high performance computing clusters.

Appendix A: Derivation of SIPDG Model Formulation

Finite element schemes utilize the weak form of a boundary value problem to express the true solution as a linear combination of basis vectors over the solution domain. Here, this philosophy remains unchanged. We multiply equation 6.1 by a test function v and integrate over the domain Ω

$$\int_{\Omega} v\left(\frac{\partial c_i}{\partial t}\right) dx - \int_{\Omega} v(\nabla \cdot \mathbf{J})\, dx = 0. \tag{6.13}$$

By the product rule and divergence theorem, the continuous Galerkin (CG) formulation is obtained

$$\int_{\Omega} v\left(\frac{\partial c_i}{\partial t}\right) dx + \int_{\Omega} \nabla v \cdot \mathbf{J}\, dx - \int_{\partial\Omega} \mathbf{J} \cdot v\mathbf{n}\, ds = 0, \tag{6.14}$$

provided the flux and potential continuity on shared element facets is strongly enforced. Allowing the molecular flux to be discontinuous between adjacent elements, the discontinuous Galerkin (DG) formulation is developed. We split the integrals from the CG formulation then evaluate them on each element $k \in T$ where T is a subdivision of Ω of k elements such that

$$\sum_{k\in T} \int_{T} v\left(\frac{\partial c_i}{\partial t}\right) dx + \sum_{k\in T} \int_{T_k} \nabla v \cdot \mathbf{J}\, dx - \sum_{k\in T} \int_{\partial T_k} \mathbf{J} \cdot v\mathbf{n}\, ds = 0. \tag{6.15}$$

On the edge of each element in a DG formulation, two separate integrals are be evaluated, namely

$$\int_{\partial T_k} (\mathbf{J}^{+}) \cdot v^{+}\mathbf{n}^{+}\, ds + \int_{\partial T_k} (\mathbf{J}^{-}) \cdot v^{-}\mathbf{n}^{-}\, ds = \int_{\partial T_k} \{\mathbf{J}\} \cdot [[v]]\, ds, \tag{6.16}$$

where $+$ and $-$ are indicators of the direction of approach to the colocated facets of adjacent elements. These integrals are rewritten using the discontinuous operators defined previously (equations 6.3 and 6.4). The mass transport flux jump condition is enforced over $\Gamma_k \in \partial T_k$ by substitution

$$-\int_{\Gamma_k} \{\mathbf{J}\} \cdot [[v]]\, ds = \int_{\Gamma_k} P_i [[c_i]] \cdot [[v]]\, ds. \tag{6.17}$$

In order to make the DG formulation positive definite we introduce terms on the remaining interior facets to penalize flux jumps

$$\sum_{k\in T}\int_{\partial T_k\setminus\Gamma_k}\frac{\alpha}{h_k}[[c_i]]\cdot[[v]]ds=0, \tag{6.18}$$

where h_k is the circumradius of element k and holds for any real positive function α. We introduce a second term to make the formulation symmetric

$$-\sum_{k\in T}\int_{\partial T_k\setminus\Gamma_k}\{\nabla v\}\cdot[[c_i]]ds=0, \tag{6.19}$$

under the assumption of a sufficiently smooth v. The penalty and the symmetry terms enable the global Dirichlet boundary conditions to be enforced through the addition of penalty integrals on $\partial\Omega_D$

$$\sum_{k\in\partial\Omega_D}\int_{\partial\Omega_k}\frac{\alpha}{h_k}v(c_i-c_D)\,ds-\sum_{k\in\partial\Omega_D}\int_{\partial\Omega_k}v(c_i-c_D)\,ds. \tag{6.20}$$

Neumann boundary conditions are applied through the addition of the standard term

$$-\sum_{k\in\partial\Omega_N}\int_{\partial\Omega_k}\mathbf{J}\cdot v\mathbf{n}\,ds, \tag{6.21}$$

though this term is ultimately zero in the present formulation. Therefore, the SIPDG method [315] formulation for the electrodiffusion of charged molecules is given by

$$\begin{aligned}\sum_{k\in T}\int_T v\left(\frac{\partial c_i}{\partial t}\right)dx+\sum_{k\in T}\int_{T_k}\nabla v\cdot\mathbf{J}\,dx&\\ -\sum_{k\in T}\int_{\partial T_k\setminus\Gamma}\{\mathbf{J}\}\cdot[[v]]\,ds-\sum_{k\in T}\int_{\partial T_k\setminus\Gamma_k}\{\nabla v\}\cdot[[c_i]]\,ds&\\ +\sum_{k\in T}\int_{\partial T_k\setminus\Gamma_k}\frac{\alpha}{h_k}[[c_i]]\cdot[[v]]\,ds-\sum_{k\in\partial\Omega_D}\int_{\partial\Omega_k}\mathbf{J}\cdot v\mathbf{n}\,ds&\\ +\sum_{k\in\partial\Omega_D}\int_{\partial\Omega_k}\frac{\alpha}{h_k}v(c_i-c_D)\,ds-\sum_{k\in\partial\Omega_D}\int_{\partial\Omega_k}v(c_i-c_D)\,ds&\\ +\sum_{k\in\Gamma}\int_{\Gamma_k}P_i[[c_i]]\cdot[[v]]\,ds=0.&\end{aligned} \tag{6.22}$$

We proceed in a similar manner for the development of the Poisson equation. Multiplying by the test

function w and integrating over Ω yields

$$-\int_{\Omega} w\nabla\cdot(\sigma\nabla u)\,dx = 0. \tag{6.23}$$

Applying the product rule followed by the divergence theorem yields

$$-\int_{\Omega}(\nabla w\cdot\sigma\nabla u)dx+\int_{\partial\Omega}(w\sigma\nabla u\cdot\mathbf{n})ds = 0. \tag{6.24}$$

We generate the DG formulation similar to before, including the additions of the symmetry, penalty, and boundary terms,

$$\begin{aligned}\sum_{k\in T}\int_{T_k}\nabla w\cdot\sigma\nabla u\,dx-\sum_{k\in T}\int_{\partial T_k\setminus\Gamma}\{\sigma\nabla u\}\cdot[[w]]\,ds-\sum_{k\in T}\int_{\partial T_k\setminus\Gamma_k}\{\nabla w\}\cdot\sigma[[u]]\,ds\\ +\sum_{k\in T}\int_{\partial T_k\setminus\Gamma_k}\frac{\alpha}{h_k}[[u]]\cdot[[w]]\,ds-\sum_{k\in\partial\Omega_D}\int_{\partial\Omega_k}\sigma\nabla u\cdot w\mathbf{n}\,ds\\ +\sum_{k\in\partial\Omega_D}\int_{\partial\Omega_k}\frac{\alpha}{h_k}w(u-u_0)\,ds-\sum_{k\in\partial\Omega_D}\int_{\partial\Omega_k}w(u-u_0)\,ds\\ +\sum_{k\in\Gamma}\int_{\Gamma_k}\frac{\varepsilon_m}{h}[[w]]\cdot\left(\frac{\partial[[u]]}{\partial t}\right)ds+\sum_{k\in\Gamma}\int_{\Gamma_k}\frac{\sigma_m}{h}[[w]]\cdot([[u]]+u_{rest})\,ds\\ +\sum_{k\in\Gamma}\int_{\Gamma_k}G_i[[w]]\cdot[[u]]\,ds,=0.\end{aligned} \tag{6.25}$$

Appendix B: Derivation of Permeability Interface Condition

Using the quasi-static assumption for a dilute solute and assuming a homogenous electric field across the cell membrane

$$c\frac{Pe_i}{h}+\mathbf{J}\cdot\mathbf{n} = D_i\frac{\partial c}{\partial r} \tag{6.26}$$

where the Peclét number is defined as $Pe_i = z_iF[[u]]/(RT)$. Integrating by separation of variables yields

$$\mathbf{J}\cdot\mathbf{n} = \left(\frac{Pe_iD_i[[c_i]]}{h(1-e^{-Pe_i})}\right) \tag{6.27}$$

where $\{\mathbf{J}\cdot\mathbf{n}\}$ is the approximates the flux between two elements in the DG formulation by the average normal flux along the collinear facets on Γ. This flux only occurs through the pores (N) and the sensitized membrane (M) and is considered through the a factor representing the membrane area susceptible to molecular flux

$$\mathbf{J}\cdot\mathbf{n} = \left(\frac{Pe_i D_i[[c_i]]}{h(1-e^{-Pe_i})}\right)\left(\pi r_0^2 H_{N_i} N + \chi_M M\right), \tag{6.28}$$

where χ_M is the relative permeability increase for the sensitized membrane fraction M.

6.6 SIPDG Simulation Code

The following code is a two-dimensional axisymmetric simulation of a single, idealized cell undergoing electroporation and is implemented using a symmetric interior penalty discontinuous Galerkin finite element method. The solution is performed directly on a mesh generated in GMSH (`modelCell_axisymm2D.xml`) using discontinuous quadratic ($p = 2$) Lagrange shape functions on triangular elements. Each component of the model is implemented as a function defined at the beginning of the script using the FEniCS finite element framework. The spatial results are saved to HDF5 (`.h5`) file format and the list of solution times is pickled for easy post processing.

```
from fenics import *
import numpy as np
import pickle

class InitialConditions(Expression):
    def __init__(self, subdomains, c_in, c_out, **kwargs):
        self.subdomains = subdomains
        self.c_in = c_in
        self.c_out = c_out

    def eval_cell(self, values, x, cell):
        if self.subdomains[cell.index] == 7: # inside circle
            values[0] = self.c_in
        elif self.subdomains[cell.index] == 8: # outside circle
            values[0] = self.c_out

class Conductivity(Expression):
```

```
    def __init__(self, subdomains, sigma_in, sigma_out, **kwargs):
        self.subdomains = subdomains
        self.sigma_in = sigma_in
        self.sigma_out = sigma_out

    def eval_cell(self, values, x, cell):
        if self.subdomains[cell.index] == 7:  # inside circle
            values[0] = self.sigma_in
        elif self.subdomains[cell.index] == 8: # outside circle
            values[0] = self.sigma_out

def hindrance(i):
    kappa = 1
    kappa += 9./8.*i*np.log(i)
    kappa += -1.56034*i
    kappa += 0.528155*i**2
    kappa += 1.91521*i**3
    kappa += -2.81903*i**4
    kappa += 0.2707884*i**5
    kappa += 1.10115*i**6
    kappa += -0.435933*i**7
    return kappa

def pores_midpoint(N, u, dt,
                   a=1.0e9, q=2.46, Neq=1.5e9, uth=0.258):
    Na = avg(N)
    U = abs(jump(u)/uth)
    ap = a*exp(U*U)
    b = Neq*exp(q*U*U)
    return (2*ap*b*dt + 2*b*Na - ap*dt*Na)/(2*b + ap*dt)

def memory_implicit(u, N, M, dt,
                    kn=1.0e5, km=4.0e-3, vmax=1.0e8):
    Ma = avg(M)
    Na = avg(N)
    U = abs(jump(u))
    Mnew = dt*(vmax*Na/(kn+Na)*(1-Ma) - km*Ma) + Ma
    return Mnew

def permeability(N, u, M,
                 hm=5e-9, rp1=0.8e-9, rp2=15.0e-9,
                 Di=0.5e-9, R=8.314, T=298.0, F=9.6e4, zp=2.0,
                  ↪ pm=1.0e4):
     # hindrance for rs/rp = 0.6
    Ma = avg(M)
    Na = avg(N)
    p1 = Constant(hindrance(0.52e-9/rp1)*np.pi*rp1**2)
    return Constant(Di/hm)*(p1*avg(N) + pm*avg(M))
```

```
65
66  def conduction(N, hm=5e-9, sigma_out=1.0, sigma_in=0.3, rp1=0.8e-9):
67      sigma_eff = (sigma_out - sigma_in)/np.log(sigma_out/sigma_in)
68      jp1 = 2*np.pi*rp1**2*sigma_eff/(np.pi*rp1+2*hm)
69      return jp1*avg(N)
70
71  def TMP(u, u0, Gi, dt, hm=5e-9, g0=2e-8,
72          eps0=8.85e-12, eps_r=8.0, urest=-0.07):
73      Jmem = eps_r*eps0/hm*(jump(u,n) - jump(u0,n))/dt # Displacement
        ↪ current
74      Jmem += g0/hm*(jump(u,n)+Constant(urest)*n('+')) # Naive
        ↪ conduction current
75      Jmem += Gi*jump(u,n) # Pore conduction current
76      return Jmem
77
78  def relError(c1, c2):
79      M = assemble((c1 - c2)**2*r*dx(degree=10))
80      M0 = assemble(c2**2*r*dx(degree=10))
81      if M0 == 0:
82          return 0.0
83      else:
84          return sqrt(M / M0)
85
86  if __name__ == '__main__':
87      ofilename = 'modelCell_axisymm2D.xml'
88      mesh = Mesh(ofilename)
89      subdomains = MeshFunction("size_t", mesh,
90                      "%s_physical_region.xml"%ofilename.split('.')[0])
91      boundaries = MeshFunction("size_t", mesh,
92                      "%s_facet_region.xml"%ofilename.split('.')[0])
93
94      ofile_cp = 'Simulation Results/axisymCell_%s_t.h5'%'cp'
95      ofile_u = 'Simulation Results/axisymCell_%s_t.h5'%'u'
96      ofile_N = 'Simulation Results/axisymCell_%s_t.h5'%'N'
97      ofile_M = 'Simulation Results/axisymCell_%s_t.h5'%'M'
98      hfile_cp = HDF5File(mesh.mpi_comm(), ofile_cp, "w")
99      hfile_u = HDF5File(mesh.mpi_comm(), ofile_u, "w")
100     hfile_N = HDF5File(mesh.mpi_comm(), ofile_N, "w")
101     hfile_M = HDF5File(mesh.mpi_comm(), ofile_M, "w")
102
103     alpha = 10.0
104     gamma = alpha
105     f = Constant(0.0)
106
107     cD = 30e-6
108     Di = 0.5e-9
109     zp = 2.0
110     R = 8.314
```

```
    F = 9.6e4
    T = 298.0
    Pe = F*zp/(R*T)

    A1 = Constant(Di)
    A2 = Constant(Di*F*zp/(R*T))

    tend = 1.0e-6
    t = 0.0
    times = []

    DG2_elem = FiniteElement('DG', mesh.ufl_cell(), 2)

    # Function space for concentration
    V_c = FunctionSpace(mesh, DG2_elem)

    #Function space for potential
    V_phi = FunctionSpace(mesh, DG2_elem)

    #Define mixed function space
    W_elem = MixedElement([DG2_elem, DG2_elem])
    W = FunctionSpace(mesh, W_elem)

    #Define trial functions
    u = Function(W)
    c, phi = split(u)

    #Defining test functions
    (v_c, v_phi) = TestFunctions(W)

    # Previous solution
    ## Note: in a 7.5 um radius cell, 9.4e-13 M is 1 molecule/cell
    phi0 = interpolate(Constant(0.0), V_phi)
    sigma = interpolate(Conductivity(subdomains,
                                     0.3, 1.0, degree=0), V_phi)
    c0 = interpolate(InitialConditions(subdomains,
                                       1.0e-13, cD, degree=0), V_c)

    Vs = FunctionSpace(mesh, 'DG', 0)
    v0 = TestFunction(Vs)
    mask_fxn = project(Constant(1.0), Vs)
    membrane_mask = Function(Vs,
                             assemble(mask_fxn('-')*avg(v0)*dS(1)))

    ds = Measure('ds', subdomain_data=boundaries)
    dS = Measure('dS', subdomain_data=boundaries)
    dx = Measure('dx', subdomain_data=subdomains)
    r = Expression('x[0]', degree=1) # axisymmetric integration
```

```
    n = FacetNormal(mesh)
    h = CellDiameter(mesh)
    h_avg = (h('+') + h('-'))/2

    N0 = Function(Vs)
    M0 = Function(Vs)

    N = Function(Vs)
    M = Function(Vs)

    times.append(t)
    hfile_u.write(phi0, '/initial')
    hfile_cp.write(c0, '/initial')
    hfile_N.write(N0, '/initial')
    hfile_M.write(M0, '/initial')

    counter = 0
    scheme = [1.0, 0.0, -1.0, 0.0]
    interval = 1.0e-6
    voltage = 40.0
    VOLT = Constant(0.0)
    err = 0.0
    Utol = 1.0e-9

    for ind, polarity in enumerate(scheme):
        VOLT.assign(polarity*voltage)
        tend = interval*(ind+1)
        dt = Constant(1.0e-9)
        gauss = lambda w_, u_, TMP_: \
                dot(grad(w_), sigma*grad(u_))*r*dx \
                - dot(jump(w_,n), avg(sigma*grad(u_)))*r*dS(0) \
                - dot(avg(sigma*grad(w_)), jump(u_,n))*r*dS(0) \
                + alpha/h_avg*dot(jump(u_,n), jump(w_,n))*r*dS(0) \
                + dot(jump(w_,n), TMP_)*r*dS(1) \
                - dot(sigma*grad(w_), (u_ - VOLT)*n)*r*ds(4) \
                - dot(w_*n, sigma*grad(u_))*r*ds(4) \
                + (gamma/h)*w_*(u_ - VOLT)*r*ds(4) \
                - dot(sigma*grad(w_), (u_ + VOLT)*n)*r*ds(6) \
                - dot(w_*n, sigma*grad(u_))*r*ds(6) \
                + (gamma/h)*w_*(u_ + VOLT)*r*ds(6)

        nernst = lambda vv_, ci_, ci0_, uu_, Pi_, dt_: \
                (1/dt_)*(ci_-ci0_)*vv_*r*dx \
                + dot(grad(vv_), A1*grad(ci_)+A2*ci_*grad(uu_))*r*dx \
                - dot(jump(vv_,n),
                    avg(A1*grad(ci_)+A2*ci_*grad(uu_)))*r*dS(0) \
                - dot(avg(A1*grad(vv_)), jump(ci_,n))*r*dS(0) \
                + alpha/h_avg*dot(jump(vv_,n), jump(ci_,n))*r*dS(0) \
```

```
            + Pi_*dot(jump(ci_,n), jump(vv_,n))*r*dS(1) \
            - dot(A1*grad(vv_), (ci_ - cD)*n)*r*ds(5) \
            - dot(vv_*n, A1*grad(ci_))*r*ds(5) \
            + (gamma/h)*vv_*(ci_ - cD)*r*ds(5) \
            - dot(vv_*n, A1*grad(ci_)+A2*ci_*grad(uu_))*r*ds(4) \
            - dot(vv_*n, A1*grad(ci_)+A2*ci_*grad(uu_))*r*ds(6)

    while (t<tend):

        F = nernst(v_c, c, c0, phi, permeability(N0,
                phi, M0, zp=zp), dt) \
            + gauss(v_phi, phi, TMP(phi, phi0,
                conduction(N0), dt))

        # Solve using default parameters
        solve(F == 0, u, [])

        # Store solutions at current timestep
        times.append(t)

        # Update function values
        (cs, phis) = u.split(True)
        err = relError(c0, cs)

        # Implicit pore step
        N.assign(Function(Vs,
                assemble(pores_midpoint(N0,
                        phis, dt)*avg(v0)*r*dS(1))))

        M.assign(Function(Vs,
                 assemble(memory_implicit(phis,
                         N0, M0, dt)*avg(v0)*r*dS(1))))

        phi0.assign(phis)
        c0.assign(cs)
        N0.assign(N)
        M0.assign(M)

        hfile_u.write(phi0.vector(),
            "/values_{}".format(len(times)-1))
        hfile_cp.write(c0.vector(),
            "/values_{}".format(len(times)-1))
        hfile_N.write(N.vector(),
            "/values_{}".format(len(times)-1))
        hfile_M.write(M.vector(),
            "/values_{}".format(len(times)-1))

        # Time stepping
```

```
            CFL = 1.0e-4
            U = abs(phi0(0, 7.5e-6 + Utol)-phi0(0, 7.5e-6  - Utol))
            dx2 = mesh.hmin()**2
            dt.assign(CFL*dx2/(2*Di*np.max([1.0,abs(Pe)*U])))
            t += dt.values()[0] # increment time step

    # Store times
    pickle.dump(times, open('Simulation Results/times.pickle', 'wb'))
```

Chapter 7

Conclusion

7.1 Introduction

Electroporation is a complex phenomenon that has shown great promise both as a tumor ablation modality and as a adjuvant therapy. Fundamentally, the mechanisms belying electroporation rely on the permeabilization of cell membranes through the restructuring of the phospholipid bilayer. This restructuring results in an enhanced permeability to small molecules, including chemotherapy drugs and tracer molecules that are unable to cross an intact cell membrane. Quantitative measurements of fluorescent tracers, such as propidium ions, as they enter the cell provide a real-time method of directly evaluating membrane permeability.

The goal of this dissertation was to characterize the permeability of mammalian cells following electroporation *in vitro*. Experimental measurements of membrane permeability were taken using quantitive fluorescence microscopy and enabled the effects of vastly different electroporation schemes to be directly compared. This method is general and applicable to any treatment condition that manipulates the cell membrane. Experimental data from these studies were used to calibrate models of electroporation-mediated mass transport. These models enable the direct comparison between measurable experimental data and the computational models for both validation and calibration. The framework I have developed for investigating membrane permeability serves as a platform for future work bridging the gap between experimental results and computational models. The work presented here is critical to more thoroughly understanding the

biophysical processes involved in cellular electroporation.

7.2 Summary of Results

In Chapter 3, propidium ions were used to characterize the spatiotemporal evolution of membrane permeability following the application of clinically relevant electrical waveforms. Data were gathered from micrographs of cells immersed in a low-conductivity buffer containing propidium. Trains of monopolar electrical pulses, similar to those used for irreversible electroporation applications, were shown to induce a significantly larger membrane permeability than high-frequency bipolar pulses. However high-frequency bipolar electric fields generated more symmetric uptake profiles between the anodic and cathodic membrane poles. A method for calculating the net membrane permeability was also demonstrated using time series micrographs. It was shown that the membrane permeability exhibits a sharp decrease in the seconds following the removal of the appleid electric field, but plateaus at a non-zero value in the minutes immediately following treatment.

The methodologies refined in Chapter 4, build upon those developed in Chapter 3. Propidium ions were observed entering into cells to calculate the net permeability for the whole cell. The fluorescence intensity of nucleic acid-bound propidium was calibrated in order to determine the intracellular concentration of bound propidium. Molecular uptake was evaluated in the minutes following electroporation with single-pulse electric fields with durations of 1, 10, 100, and 1000 μs and strengths of 170 to 400 kV/m with the maximum net diffusive permeability across all treatments reaching 1.3×10^{-8} m/s. It was demonstrated that a population of cells is heterogenous in its electroporation-mediated uptake response, especially near the strength-duration threshold for electroporation.

Together, these results comprise the development of a method of measuring membrane permeability to fluorescent tracer molecules following electroporation based on time series fluorescence micrographs. This technique is a fundamental improvement over relative intensity measurements as it provides quantitative data critical to calibrating computational models of cellular electroporation. Furthermore, such data can be used to compare dramatically different electroporation schemes with unequal applied energies, such as the difference apparent in clinical irreversible electroporation and high-frequency irreversible electroporation

therapies.

In Chapter 5, the quantitative measurements of membrane permeability from Chapter 4 are used to calibrate a dynamical system model of molecular uptake following electroporation. This model comprises two porosity stages that modulate the membrane permeability to small molecules. The model itself focuses on the cell as a unit entity and therefore serves as a bridge between the quantitative single-cell measurements in Chapter 4 and the evaluation of other computational models, including the spatiotemporal model developed in Chapter 6. Calibration with the experimental data indicates that buffer composition is an important parameter in electroporation-induced membrane permeability. The model considers pore formation on the cell membrane, the evolution of the electric field within the vicinity of the cell, and the flux of charged particles during and following electroporation. This scheme is able to directly account for the flux jump across a thin structure, such as the cell membrane, across which a discontinuous flux exists. This model is able to account for the asymmetric molecular uptake patterns observed in Chapter 3 and shows that ionic fluxes through membrane pores inhibit the growth of the transmembrane potential beyond 2- to 5-fold larger than the electroporation threshold.

Extending the model to multi-pulse electroporation schemes reveals that the per-pulse permeability increase occurs proportional to the square root of the pulse number for sufficiently short pulse durations and inter-pulse delays. Additionally, the model predicts that while the inter-pulse delay impacts membrane conductance, it has very little impact on membrane permeability for inter-pulse delays shorter than 0.1 s. This model is readily calibrated with single-cell experimental observations and sufficiently flexible for refinement as new data becomes available.

From a computational perspective, the dynamical system model of electroporation sacrifices spatial resolution for the ability to be easily calibrated using experimental data. This model serves as an intermediate between complex three-dimensional models of cellular electroporation, such as the DG model in Chapter 6, and experimental uptake data, such as in Chapters 3 and 4. The DG model is developed for future implementation on a high-performance computing cluster, which could make comparison with experimental data more feasible using parallel solvers than with more conventional serial solution strategies.

7.3 Future Work

The work presented in this dissertation is focused on the relationship between experimental and computational data and bridging the communication gap between the two approaches. The analytical tools I have developed enable the investigation of several research questions that were previously difficult to address. In particular, pore formation, relaxation, and expansion are all process that have not been directly observed experimentally but are the basis of many current computational paradigms. Pore relaxation occurs rapidly within the model in Chapter 6 and results in rapidly-decreasing membrane permeability following removal of the applied electric field. However, experimental evidence in Chapters 3 and 4 demonstrates that the membrane remains permeable for minutes to hours following electroporation. These results suggest that secondary mechanisms influence post-PEF membrane permeability and must therefore be experimentally investigated to produce a more complete understanding of the electroporation process.

The quantitative fluorescence microscopy techniques used in Chapters 3 and 4 will be critical to the investigation of the role of other membrane permeabilization methodologies, such as mechanical deformation or oxidation, in electroporation-based technologies and therapies. The dynamical system model in Chapter 5 provides a framework to evaluated the complex interactions between pore-forming mechanisms and these secondary mechanisms. The model in Chapter 6 is able to provide a method to identify potential mechanisms and inform the experimental investigations and is directly comparable with the dynamical system model. This synergistic feedback between computational and experimental investigations is important to optimizing electroporation technology for future applications.

One of the critical technologies that enables experimental studies of electroporation is the high-voltage pulsed power instrumentation required to form the requisite PEFs. This equipment is often expensive and limited in its design to a specific waveform parameter space, including limitations in polarity, power, and bandwidth. Especially down to pulse durations of 1 μs or less, the instrumentation required for experimental investigations is often custom designed and built at a non-trivial expense. The design and manufacture of a custom-built solid-state Marx topology pulse generator has been an ongoing progress over the past several years in collaboration with Suyashree Bhonsle, Natalie White, and Yajun Zhao. The present prototype design is built from commercial, off-the-shelf parts and includes a laptop-based user interface with a control system that allows for greater flexibility than commercial pulse generators. This generator will

enable greater flexibility in the electric field waveforms used during *in vitro* electroporation experiments as well enable synchronization with microscopy systems that was not otherwise possible with the available equipment.

7.4 Conclusion

In this dissertation, I have described a fundamental experimental research method for calculating the net cell membrane permeability using calibrated time series fluorescence micrographs. These data have enabled the quantitative characterization of cell membrane permeability using equipment ubiquitous in microbiology laboratories. This technique has enabled the development and calibration of theoretical models that inform experimental design and technological development. The methodologies and results discussed provide a framework for improving the relationship between computational and experimental results in the field of electroporation, and more broadly, membrane permeability.

7.5 Additional Peer-Reviewed Work

This dissertation references other peer-reviewed material that has been published by the author:

- **DC Sweeney**, RE Neal III, RV Davalos. *Multi-scale biophysical principles in clinical irreversible electroporation*. Irreversible Electroporation in Clinical Practice. Ed. R Meijerink, HJ Scheffer, G Narayanan. Springer International Publishing. 2018.
- TA Douglas, J Cemazar, N Balani, **DC Sweeney**, EM Schmelz, RV Davalos. *A feasibility study for enrichment of highly-aggressive cancer subpopulations by their biophysical properties via dielectrophoresis enhanced with synergistic fluid flow*. Electrophoresis. (27 Mar 2017).
- T Murovec, **DC Sweeney**, E Latouche, RV Davalos, C Brosseau. *Modeling of Transmembrane Potential in Realistic Multicellular Structures before Electroporation*. Biophysical Journal. 111(10), pp.2286-2295, (2016).

- SP Bhonsle, CB Arena, **DC Sweeney**, RV Davalos. *Mitigation of impedance changes due to electroporation therapy using bursts of high-frequency bipolar pulses*. Biomed. Eng. Online 14(3). (2015).

Bibliography

[1] Matej Kranjc, Franci Bajd, Igor Sersa, Eung Je Woo, and Damijan Miklavcic. Ex Vivo and In Silico Feasibility Study of Monitoring Electric Field Distribution in Tissue during Electroporation Based Treatments. PLoS ONE, 7(9):3–10, 2012.

[2] Dun Liu, Lijun Wang, Zhigang Wang, and Alfred Cuschieri. Magnetoporation and magnetolysis of cancer cells via carbon nanotubes induced by rotating magnetic fields. Nano Letters, 12(10):5117–5121, 2012.

[3] Vitalij Novickij, Audrius Grainys, Egl Lastauskien, Ruta Kananaviciute, Dovil Pamedytyt, Lilija Kalediene, Jurij Novickij, and Damijan Miklavčič. Pulsed Electromagnetic Field Assisted in vitro Electroporation: A Pilot Study. Scientific Reports, 6(September):33537, 2016.

[4] Vitalij Novickij, Janja Dermol, Audrius Grainys, Matej Kranjc, and Damijan Miklavčič. Membrane permeabilization of mammalian cells using bursts of high magnetic field pulses. PeerJ, 5:e3267, 2017.

[5] Michael Forde and Pat Ridgely. Implantable cardiac pacemakers. Medical Devices and Systems, The Biomed Eng handbook, 3rd edn. CRC Press, Taylor and Francis Group, Boca Raton, FL, 2006.

[6] DM Andrade, D Zumsteg, C Hamani, M Hodaie, S Sarkissian, AM Lozano, and RA Wennberg. Long-term follow-up of patients with thalamic deep brain stimulation for epilepsy. Neurology, 66(10):1571–1573, 2006.

[7] Paul Boon, Kristl Vonck, Veerle De Herdt, Annelies Van Dycke, Maarten Goethals, Lut Goossens, Michel Van Zandijcke, Tim De Smedt, Isabelle Dewaele, Rik Achten, et al. Deep brain stimulation in patients with refractory temporal lobe epilepsy. Epilepsia, 48(8):1551–1560, 2007.

[8] Andrew B Schwartz, X Tracy Cui, Douglas J Weber, and Daniel W Moran. Brain-controlled interfaces: movement restoration with neural prosthetics. Neuron, 52(1):205–220, 2006.

[9] Jessica Cunningham, Veronica Estrella, Mark Lloyd, Robert Gillies, B Roy Frieden, and Robert Gatenby. Intracellular electric field and pH optimize protein localization and movement. PloS one, 7(5):e36894, jan 2012.

[10] JA Dykens and AK Stout. Assessment of mitochondrial membrane potential in situ using single potentiometric dyes and a novel fluorescence resonance energy transfer technique. Methods in Cell Biology, 65, 2001.

[11] J Plášek, A Vojtíšková, and J Houštěk. Flow-cytometric monitoring of mitochondrial depolarisation: from fluorescence intensities to millivolts. Journal of Photochemistry and Photobiology B: Biology, 78(2):99–108, 2005.

[12] I.G. Abidor, V.B. Arakelyan, L.V. Chernomordik, Yu.A. Chizmadzhev, V.F. Pastushenko, and M.R. Tarasevich. 246 - Electric breakdown of bilayer lipid membranes I. The main experimental facts and their qualitative discussion. Bioelectrochemistry and Bioenergetics, 6(1):37–52, 1979.

[13] John C. Neu, Kyle C. Smith, and Wanda Krassowska. Electrical energy required to form large conducting pores. Bioelectrochemistry, 60(1-2):107–114, 2003.

[14] M. Tarek. Membrane electroporation: a molecular dynamics simulation. Biophysical Journal,

88(6):4045–53, Jun 2005.

[15] Christelle Rosazza, Sasa Haberl Meglic, Andreas Zumbusch, Marie-Pierre Rols, and Damijan Miklavcic. Gene Electrotransfer: A Mechanistic Perspective. Current gene therapy, 16(2):98–129, 2016.

[16] R. V. Davalos, L. M. Mir, and B. Rubinsky. Tissue ablation with irreversible electroporation. Annals of Biomedical Engineering, 33(2):223–231, Feb 2005.

[17] Paulo A Garcia, John H Rossmeisl, John Robertson, Thomas L Ellis, and Rafael V Davalos. Pilot study of irreversible electroporation for intracranial surgery. Conference proceedings : ... Annual International Conference of the IEEE Engineering in Medicine and Biology Society. IEEE Engineering in Medicine and Biology Society. Annual Conference, 2009:6513–6, jan 2009.

[18] Paulo A Garcia, John H Rossmeisl, Robert E Neal, Thomas L Ellis, John D Olson, Natalia Henao-Guerrero, John Robertson, and Rafael V Davalos. Intracranial nonthermal irreversible electroporation: in vivo analysis. The Journal of membrane biology, 236(1):127–36, jul 2010.

[19] John H Jr Rossmeisl, Paulo A Garcia, John L Roberston, Thomas L Ellis, and Rafael V Davalos. Science Pathology of non-thermal irreversible electroporation (N-TIRE) -induced ablation of the canine brain. Journal of Veterinary Science, 14(May 2012):433–440, 2013.

[20] R. E. Neal, J. H. Rossmeisl, V. D'Alfonso, J. L. Robertson, P. a. Garcia, S. Elankumaran, and R. V. Davalos. In vitro and numerical support for combinatorial irreversible electroporation and electrochemotherapy glioma treatment. Annals of Biomedical Engineering, 42(3):475–487, 2014.

[21] Hanne Falk, Susanne Lambaa, Helle Hjorth Johannesen, Gitte Wooler, Alessandro Venzo, and Julie Gehl. Electrochemotherapy and calcium electroporation inducing a systemic immune response with local and distant remission of tumors in a patient with malignant melanoma a case report. Acta Oncologica, 0(0):1–6, 2017.

[22] Suyashree Bhonsle, Mohammad Bonakdar, Robert E. Neal, Charles Aardema, John L. Robertson, Jonathon Howarth, Helen Kavnoudias, Kenneth R. Thomson, S. Nahum Goldberg, and Rafael V. Davalos. Characterization of Irreversible Electroporation Ablation with a Validated Perfused Organ Model. Journal of Vascular and Interventional Radiology, pages 1–12, 2016.

[23] Marleen C A M Melenhorst, Hester J. Scheffer, Laurien G P H Vroomen, Geert Kazemier, M. Petrousjka van den Tol, and Martijn R. Meijerink. Percutaneous Irreversible Electroporation of Unresectable Hilar Cholangiocarcinoma (Klatskin Tumor): A Case Report. CardioVascular and Interventional Radiology, 39(1):117–121, 2016.

[24] Maciej Pech, Andreas Janitzky, Johann Jacob Wendler, Christof Strang, Simon Blaschke, Oliver Dudeck, Jens Ricke, and Uwe-Bernd Liehr. Irreversible electroporation of renal cell carcinoma: a first-in-man phase I clinical study. Cardiovascular and interventional radiology, 34(1):132–8, feb 2011.

[25] Anabel José, Luciano Sobrevals, Antoni Ivorra, and Cristina Fillat. Irreversible electroporation shows efficacy against pancreatic carcinoma without systemic toxicity in mouse models. Cancer letters, 317(1):16–23, apr 2012.

[26] Kevin P Charpentier, Farrah Wolf, Lelia Noble, Brody Winn, Murray Resnick, and Damian E Dupuy. Irreversible electroporation of the pancreas in swine: a pilot study. HPB : the official journal of the International Hepato Pancreato Biliary Association, 12(5):348–51, jun 2010.

[27] Anabel José, Luciano Sobrevals, Antoni Ivorra, and Cristina Fillat. Irreversible electroporation shows efficacy against pancreatic carcinoma without systemic toxicity in mouse models. Cancer letters, 317(1):16–23, apr 2012.

[28] Mary Phillips, Hanush Krishnan, Narayan Raju, and Boris Rubinsky. Tissue ablation by a synergistic combination of electroporation and electrolysis delivered by a single pulse. Annals of biomedical engineering, 2016, 2016.

[29] P. Marsanic, A. Mellano, A. Sottile, and M. De Simone. Irreversible electroporation as treatment

of locally advanced and as margin accentuation in borderline resectable pancreatic adenocarcinoma. Medical & Biological Engineering & Computing, 2017.

[30] S. K. Frandsen, H. Gissel, P. Hojman, J. Eriksen, and J. Gehl. Calcium electroporation in three cell lines: a comparison of bleomycin and calcium, calcium compounds, and pulsing conditions. Biochimica et Biophysica Acta - General Subjects, 1840(3):1204–1208, 2014.

[31] E. L. Hansen, E. B. Sozer, S. Romeo, S. K. Frandsen, P. T. Vernier, and J. Gehl. Dose-dependent ATP depletion and cancer cell death following calcium electroporation, relative effect of calcium concentration and electric field strength. PLoS ONE, 10(4):1–12, 2015.

[32] S. K. Frandsen, H. Gissel, P. Hojman, T. Tramm, J. Eriksen, and J. Gehl. Direct therapeutic applications of calcium electroporation to effectively induce tumor necrosis. Cancer Research, 72(6):1336–1341, 2012.

[33] Yoshihide Tsujimoto. Apoptosis and necrosis: intracellular ATP level as a determinant for cell death modes. Cell death and differentiation, 4(6):429–434, 1997.

[34] E Neumann, M Schaefer-Ridder, Y Wang, and P H Hofschneider. Gene transfer into mouse lyoma cells by electroporation in high electric fields. The EMBO journal, 1(7):841–845, 1982.

[35] R. Heller, M. Jaroszeski, A. Atkin, D. Moradpour, R. Gilbert, J. Wands, and C. Nicolau. In vivo gene electroinjection and expression in rat liver. FEBS letters, 389(3):225–228, 1996.

[36] Takeshi Suzuki, Bo-Chul Shin, Keiko Fujikura, Toshiyuki Matsuzaki, and Kuniaki Takata. Direct gene transfer into rat liver cells by in vivo electroporation. FEBS Letters, 425(3):436–440, 1998.

[37] L M Mir, L F Glass, G Sersa, J Teissié, C Domenge, D Miklavcic, M J Jaroszeski, S Orlowski, D S Reintgen, Z Rudolf, M Belehradek, R Gilbert, M P Rols, J Belehradek, J M Bachaud, R DeConti, B Stabuc, M Cemazar, P Coninx, and R Heller. Effective treatment of cutaneous and subcutaneous malignant tumours by electrochemotherapy. British journal of cancer, 77(12):2336–42, 1998.

[38] Manuela Cappelletti, Immacolata Zampaglione, Gabriella Rizzuto, Gennaro Ciliberto, Nicola La Monica, and Elena Fattori. Gene electro-transfer improves transduction by modifying the fate of intramuscular DNA. Journal of Gene Medicine, 5(4):324–332, 2003.

[39] Immacolata Zampaglione, Mirko Arcuri, Manuela Cappelletti, Gennaro Ciliberto, Gemma Perretta, Alfredo Nicosia, Nicola La Monica, and Elena Fattori. In vivo DNA gene electro-transfer: a systematic analysis of different electrical parameters. The journal of gene medicine, 7(11):1475–81, 2005.

[40] Adil I. Daud, Ronald C. DeConti, Stephanie Andrews, Patricia Urbas, Adam I. Riker, Vernon K. Sondak, Pamela N. Munster, Daniel M. Sullivan, Kenneth E. Ugen, Jane L. Messina, and Richard Heller. Phase I trial of interleukin-12 plasmid electroporation in patients with metastatic melanoma. Journal of Clinical Oncology, 26(36):5896–5903, 2008.

[41] Muriel Golzio, Justin Teissié, and Marie Pierre Rols. Cell synchronization effect on mammalian cell permeabilization and gene delivery by electric field. Biochimica et Biophysica Acta - Biomembranes, 1563(1-2):23–28, 2002.

[42] M. F. Bureau, J. Gehl, V. Deleuze, L. M. Mir, and D. Scherman. Importance of association between permeabilization and electrophoretic forces for intramuscular DNA electrotransfer. Biochimica et Biophysica Acta - General Subjects, 1474(3):353–359, 2000.

[43] Maša Kandušer, Damijan Miklavčič, and Mojca Pavlin. Mechanisms involved in gene electrotransfer using high- and low-voltage pulses - An in vitro study. Bioelectrochemistry, 74(2):265–271, 2009.

[44] G. Sersa, M. Cemazar, and D. Miklavčič. Antitumor effectiveness of electrochemotherapy with cis-diamminedichloroplatinum(II) in mice. Cancer Research, 55(15):3450–3455, 1995.

[45] Anita Gothelf, Lluis M Mir, and Julie Gehl. Electrochemotherapy: results of cancer treatment using enhanced delivery of bleomycin by electroporation. Cancer Treatment Reviews, 29(5):371–387, oct 2003.

[46] Birgit Agerholm-Larsen, Helle K. Iversen, Per Ibsen, Jakob M. Moller, Faisal Mahmood, Kurt Svarre

Jensen, and Julie Gehl. Preclinical validation of electrochemotherapy as an effective treatment for brain tumors. Cancer Research, 71(11):3753–3762, 2011.

[47] I Edhemovich, E Brecelj, A Ivanecz, G Gasljevic, M Marolt Music, T Jarm, B Kos, M Mosnjak, M Cemazar, D Miklavčič, S Potrc, E Gadzijev, and G Sersa. Electrochemotherapy of Colorectal Liver Metastases-Trial Update. IFMBE Proceedings, 53(Wc 2015):243–246, 2016.

[48] C Cabula, L G Campana, G Grilz, S Galuppo, R Bussone, L De Meo, A Bonadies, P Curatolo, M De Laurentiis, M Renne, S Valpione, T Fabrizio, N Solari, M Guida, A Santoriello, M D'Aiuto, and R Agresti. Electrochemotherapy in the Treatment of Cutaneous Metastases from Breast Cancer: A Multicenter Cohort Analysis. Annals of surgical oncology, pages 442–450, 2015.

[49] T. Kotnik, A. Maček-Lebar, D. Miklavčič, and L. M. Mir. Evaluation of cell membrane electropermeabilization by means of a nonpermeant cytotoxic agent. Biotechniques, 28(5):921–926, 2000.

[50] G. Pucihar, T. Kotnik, B. Valič, and D. Miklavčič. Numerical determination of transmembrane voltage induced on irregularly shaped cells. Annals of Biomedical Engineering, 34(4):642–652, 2006.

[51] Saša Haberl and Mojca Pavlin. Use of Collagen Gel as a Three-Dimensional In Vitro Model to Study Electropermeabilization and Gene Electrotransfer. The Journal of Membrane Biology, 236(1):87–95, 2010.

[52] C. B. Arena, R. L. Mahajan, M. N. Rylander, and R. V. Davalos. Towards the development of latent heat storage electrodes for electroporation-based therapies. Applied Physics Letters, 101(2012), 2012.

[53] Jill W. Ivey, Eduardo L. Latouche, Michael B. Sano, John H. Rossmeisl, Rafael V. Davalos, and Scott S. Verbridge. Targeted cellular ablation based on the morphology of malignant cells. Scientific Reports, 5:17157, 2015.

[54] Andraž Polak, Daniel Bonhenry, François Dehez, Peter Kramar, Damijan Miklavčič, and Mounir Tarek. On the electroporation thresholds of lipid bilayers: molecular dynamics simulation investigations. The Journal of membrane biology, 246(11):843–50, nov 2013.

[55] M Laura Fernandez, Guillermo Marshall, Francesc Sague, and Ramon Reigada. Structural and Kinetic Molecular Dynamics Study of Electroporation in Cholesterol-Containing Bilayers. Journal of Physical Chemistry B, 114:6855–6865, 2010.

[56] LF Jaffe. Electrophoresis along cell membranes. Nature, 265, 1977.

[57] S McLaughlin and M M Poo. The role of electro-osmosis in the electric-field-induced movement of charged macromolecules on the surfaces of cells. Biophysical journal, 34(1):85–93, apr 1981.

[58] Paul J Canatella, Joan F Karr, John A Petros, and Mark R Prausnitz. Quantitative Study of Electroporation-Mediated Molecular Uptake and Cell Viability. Biophysical Journal, 80(2):755–764, 2001.

[59] L. Rems and D. Miklavčič. Tutorial: electroporation of cells in complex materials and tissue. Journal of Applied Physics, 119(20):201101, 2016.

[60] AL Hodgkin, AF Huxley, and B Katz. Measurement of Current-Voltage Relations in the Membrane of the Giant Axion of Loligo. Current, 116:424–448, 1952.

[61] Herman P Schwan. Electrical Properties of Tissue and Cell Suspensions. In Advances in biological and medical physics, volume 5, page 147. Academic Press, New York, 1957.

[62] Tadej Kotnik, Damijan Miklavčič, and Tomaž Slivnik. Time course of transmembrane voltage induced by time-varying electric fields - A method for theoretical analysis and its application. Bioelectrochemistry and Bioenergetics, 45(1):3–16, 1998.

[63] B Valic, M Golzio, M Pavlin, A Schatz, C Faurie, B Gabriel, J Teissie, M P Rols, and D Miklavcic. Effect of electric field induced transmembrane potential on spheroidal cells: theory and experiment. Eur Biophys J, 32(6):519–528, 2003.

[64] K.C. Smith, T.R. Gowrishankar, a.T. Esser, D.a. Stewart, and J.C. Weaver. The Spatially Distributed Dynamic Transmembrane Voltage of Cells and Organelles due to 10 ns Pulses: Meshed Transport

Networks. IEEE Transactions on Plasma Science, 34(4):1394–1404, aug 2006.
[65] Tadej Kotnik, Gorazd Pucihar, and Damijan Miklavčič. Induced transmembrane voltage and its correlation with electroporation- mediated molecular transport. Journal of Membrane Biology, 236(1):3–13, 2010.
[66] S J Marrink, F Jähnig, and H J Berendsen. Proton transport across transient single-file water pores in a lipid membrane studied by molecular dynamics simulations. Biophysical journal, 71(August):632–647, 1996.
[67] D. P. Tieleman, S. J. Marrink, and H. J. C. Berendsen. A computer perspective of membranes: molecular dynamics studies of lipid bilayer systems. Biochimica et Biophysica Acta - Reviews on Biomembranes, 1331(3):235–270, 1997.
[68] Hari Leontiadou, Alan E Mark, and Siewert J Marrink. Molecular dynamics simulations of Hydrophilic Pores in Lipid Bilayers. Biophysical Journal, 86(April):2156–2164, 2004.
[69] D. Peter Tieleman, Hari Leontiadou, Alan E. Mark, and Siewert J. Marrink. Simulation of pore formation in lipid bilayers by mechanical stress and electric fields. Journal of the American Chemical Society, 125(21):6382–6383, 2003.
[70] Peter Kramar, Lucie Delemotte, Alenka Maček Lebar, Malgorzata Kotulska, Mounir Tarek, and Damijan Miklavčič. Molecular-level characterization of lipid membrane electroporation using linearly rising current. The Journal of membrane biology, 245(10):651–9, oct 2012.
[71] Lucie Delemotte and Mounir Tarek. Molecular dynamics simulations of lipid membrane electroporation. The Journal of membrane biology, 245(9):531–43, sep 2012.
[72] K A DeBruin and W Krassowska. Modeling electroporation in a single cell. I. Effects Of field strength and rest potential. Biophysical journal, 77(3):1213–24, sep 1999.
[73] R. W. Glaser, S. L. Leikin, L. V. Chernomordik, V. F. Pastushenko, and A. I. Sokirko. Reversible electrical breakdown of lipid bilayers: formation and evolution of pores. Biochimica et biophysica acta, 940:275–287, 1988.
[74] V F Pastushenko, Y U a Chizmadzhev, and V B Arakelyan. 247 - Electric Breakdown of Bilayer Lipid Membranes II . Calculation of the Membrane Lifetime in the Steady-State Diffusion Approximation. Biochemistry and Bioenergetics, 6:53–62, 1979.
[75] Kyle C Smith, John C Neu, and Wanda Krassowska. Model of creation and evolution of stable electropores for DNA delivery. Biophysical journal, 86(5):2813–2826, 2004.
[76] Q Hu, R P Joshi, and K H Schoenbach. Simulations of nanopore formation and phosphatidylserine externalization in lipid membranes subjected to a high-intensity , ultrashort electric pulse. Physical Review E, 72:1–10, 2005.
[77] Bennett L. Ibey, Dustin G. Mixon, Jason a. Payne, Angela Bowman, Karl Sickendick, Gerald J. Wilmink, W. Patrick Roach, and Andrei G. Pakhomov. Plasma membrane permeabilization by trains of ultrashort electric pulses. Bioelectrochemistry, 79(1):114–121, 2010.
[78] Andrew L. Frelinger, Anja J. Gerrits, Allen L. Garner, Andrew S. Torres, Antonio Caiafa, Christine A. Morton, Michelle A. Berny-Lang, Sabrina L. Carmichael, V. Bogdan Neculaes, and Alan D. Michelson. Modification of Pulsed Electric Field Conditions Results in Distinct Activation Profiles of Platelet-Rich Plasma. Plos One, 11(8):e0160933, 2016.
[79] J. Li and H. Lin. The current-voltage relation for electropores with conductivity gradients. Biomicrofluidics, 4(1):1–17, 2010.
[80] Miao Yu and Hao Lin. Quantification of propidium iodide delivery with millisecond electric pulses: A model study. arXiv preprint arXiv:1401.6954, (arXiv preprint arXiv:1401.6954):1–23, 2014.
[81] M. M. Sadik, J. Li, J. W. Shan, D. I. Shreiber, and H. Lin. Quantification of propidium iodide delivery using millisecond electric pulses: experiments. Biochimica et Biophysica Acta - Biomembranes, 1828(4):1322–1328, 2013.
[82] Wanda Krassowska and Petar D Filev. Modeling electroporation in a single cell. Biophysical journal,

92(2):404–417, 2007.

[83] Alexander Golberg and Boris Rubinsky. Mass Transfer Phenomena in Electroporation. Elsevier Inc., 2013.

[84] Reuben Son, Thiruvallur Gowrishankar, Kyle Smith, and James Weaver. Modeling a conventional electroporation pulse train:Decreased pore number, cumulative calcium transportand an example of electrosensitization. IEEE Transactions on Biomedical Engineering, 9294(c):1–1, 2015.

[85] Marie-Pierre Rols and Justin Teissié. Electropermeabilization of mammalian cells: Quantitative Analysis of the phenomenon. Biophysical Journal, 58(5):1089–1098, 1990.

[86] M P Rols and J Teissie. Modulation of electrically induced permeabilization and fusion of Chinese hamster ovary cells by osmotic pressure. Biochemistry, 29(19):4561–4567, 1990.

[87] M P Rols and J Teissié. Electropermeabilization of mammalian cells to macromolecules: control by pulse duration. Biophysical Journal, 75(3):1415–1423, 1998.

[88] M Golzio, M P Rols, and J Teissié. In vitro and in vivo electric field-mediated permeabilization, gene transfer, and expression. Methods (San Diego, Calif.), 33(2):126–35, jun 2004.

[89] R. Shirakashi, V.L. Sukhorukov, I. Tanasawa, and U. Zimmermann. Measurement of the permeability and resealing time constant of the electroporated mammalian cell membranes. International Journal of Heat and Mass Transfer, 47(21):4517–4524, 2004.

[90] A. M. Bowman, O. M. Nesin, O. N. Pakhomova, and A. G. Pakhomov. Analysis of plasma membrane integrity by fluorescent detection of Tl(+) uptake. Journal of Membrane Biology, 236(1):15–26, 2010.

[91] Kazuhiko Jr Kinosita and Tian Yow Tsong. Formation and resealing of pores of controlled sizes in human erythrocyte membrane. Nature, 268(4), 1977.

[92] Jeffrey C. Mohr, Juan J. De Pablo, and Sean P. Palecek. Electroporation of human embryonic stem cells: Small and macromolecule loading and DNA transfection. Biotechnology Progress, 22(3):825–834, 2006.

[93] O. N. Pakhomova, B. W. Gregory, V. A. Khorokhorina, A. M. Bowman, S. Xiao, and A. G. Pakhomov. Electroporation-induced electrosensitization. PLoS ONE, 6(2):36–38, 2011.

[94] Daniel C. Sweeney, Matej Reberšek, Janja Dermol, Lea Rems, Damijan Miklavčič, and Rafael V. Davalos. Quantification of cell membrane permeability induced by monopolar and high frequency bipolar bursts of electrical pulses. Biochimica et Biophysica Acta (BBA) - Biomembranes, 1858:2689–2698, 2016.

[95] C. Virginio, A. Mackenzie, R. A. North, and A. Surprenant. Kinetics of cell lysis, dye uptake and permeability changes in cells expressing the rat P2X7 receptor. Journal of Physiology, 519(2):335–346, 1999.

[96] Stephen J. Beebe, P. M. Fox, L. J. Rec, K. Somers, Robert H. Stark, and Karl H. Schoenbach. Nanosecond pulsed electric field (nsPEF) effects on cells and tissues: Apoptosis induction and tumor growth inhibition. IEEE Transactions on Plasma Science, 30(1 II):286–292, 2002.

[97] KH Schoenbach, Barbara Hargrave, RP Joshi, JF Kolb, R Nuccitelli, C Osgood, A Pakhomov, M Stacey, RJ Swanson, JA White, Shu Xiao, and Jue Zhang. Bioelectric effects of intense nanosecond pulses. Dielectrics and Electrical ..., 14(5):1088–1109, 2007.

[98] Yasir Demiryurek, Masoud Nickaeen, Mingde Zheng, Miao Yu, Jeffrey D. Zahn, David I. Shreiber, Hao Lin, and Jerry W. Shan. Transport, resealing, and re-poration dynamics of two-pulse electroporation-mediated molecular delivery. Biochimica et Biophysica Acta - Biomembranes, 1848(8):1706–1714, 2015.

[99] Hsiang-Yu Wang and Chang Lu. Microfluidic electroporation for delivery of small molecules and genes into cells using a common DC power supply. Biotechnology and bioengineering, 100(3):579–86, jun 2008.

[100] M. Bonakdar, E. M. Wasson, Y. W. Lee, and R. V. Davalos. Electroporation of brain endothelial cells on chip toward permeabilizing the blood-brain barrier. Biophysical Journal, 110(2):503–513, 2016.

[101] Alan S Verkman. Solute and macromolecule diffusion in cellular aqueous compartments. Trends in Biochemical Sciences, 27(1):27–33, 2002.
[102] D. C. Chang and T. S. Reese. Changes in membrane structure induced by electroporation as revealed by rapid-freezing electron microscopy. Biophysical Journal, 58(1):1–12, 1990.
[103] F Ryttsén, C Farre, C Brennan, S G Weber, K Nolkrantz, K Jardemark, D T Chiu, and O Orwar. Characterization of single-cell electroporation by using patch-clamp and fluorescence microscopy. Biophysical Journal, 79(4):1993–2001, Oct 2000.
[104] Jason T. Sengel and Mark I. Wallace. Imaging the dynamics of individual electropores. Proceedings of the National Academy of Sciences of the United States of America, 113(19):5281–5286, 2016.
[105] D Peter Tieleman. The molecular basis of electroporation. BMC Biochemistry, 12:1–12, 2004.
[106] M. Pavlin and D. Miklavčič. Theoretical and experimental analysis of conductivity, ion diffusion and molecular transport during cell electroporation - relation between short-lived and long-lived pores. Bioelectrochemistry, 74(1):38–46, 2008.
[107] K C Melikov, V A Frolov, A Shcherbakov, A V Samsonov, Y A Chizmadzhev, and L V Chernomordik. Voltage-induced nonconductive pre-pores and metastable single pores in unmodified planar lipid bilayer. Biophysical journal, 80(4):1829–1836, 2001.
[108] S. J. Marrink, E. Lindahl, O. Edholm, and A. E. Mark. Simulation of the spontaneous aggregation of phospholipids into bilayers [23]. Journal of the American Chemical Society, 123(35):8638–8639, 2001.
[109] Tomo Murovec, DanielC. Sweeney, Eduardo Latouche, RafaelV. Davalos, and Christian Brosseau. Modeling of Transmembrane Potential in Realistic Multicellular Structures before Electroporation. Biophysical Journal, 111(10):2286–2295, 2016.
[110] K. C. Smith, R. S. Son, T. R. Gowrishankar, and J. C. Weaver. Emergence of a large pore subpopulation during electroporating pulses. Bioelectrochemistry, 100:3–10, 2013.
[111] Reuben S Son, Kyle C Smith, Thiruvallur R Gowrishankar, P Thomas Vernier, and James C Weaver. Basic features of a cell electroporation model: illustrative behavior for two very different pulses. The Journal of membrane biology, 247(12):1209–1228, 2014.
[112] Donald C Chang and Thomas S Reese. Changes by revealed rapid-freezing microscopy. Biophysical Journal, 58(July 1990):1–12, 1988.
[113] Arthur E. Sowers and Michael R. Lieber. Electropore diameters, lifetimes, numbers, and locations in individual erythrocyte ghosts. FEBS Letters, 205(2):179–184, 1986.
[114] Alexander Pribush, Dan Meyerstein, and Naomi Meyerstein. Kinetics of erythrocyte swelling and membrane hole formation in hypotonic media. Biochimica et Biophysica Acta - Biomembranes, 1558(2):119–132, 2002.
[115] Nicolas Groulx, Francis Boudreault, Sergei N. Orlov, and Ryszard Grygorczyk. Membrane reserves and hypotonic cell swelling. Journal of Membrane Biology, 214(1-2):43–56, 2006.
[116] Olena M. Nesin, Olga N. Pakhomova, Shu Xiao, and Andrei G. Pakhomov. Manipulation of cell volume and membrane pore comparison following single cell permeabilization with 60- and 600-ns electric pulses. Biochimica et Biophysica Acta - Biomembranes, 1808(3):792–801, 2011.
[117] G. P. Tolstykh, G. L. Thompson, H. T. Beier, Z. A. Steelman, and B. L. Ibey. nsPEF-induced PIP2 depletion, PLC activity and actin cytoskeletal cortex remodeling are responsible for post-exposure cellular swelling and blebbing. Biochemistry and Biophysics Reports, 2016.
[118] Andrei G. Pakhomov, Rachael Shevin, Jody a White, Juergen F Kolb, Olga N Pakhomova, Ravindra P Joshi, and Karl H Schoenbach. Membrane permeabilization and cell damage by ultrashort electric field shocks. Archives of biochemistry and biophysics, 465(1):109–18, sep 2007.
[119] Mikhail A. Rassokhin and Andrei G. Pakhomov. Electric field exposure triggers and guides formation of pseudopod-like blebs in U937 monocytes. Journal of Membrane Biology, 245(9):521–529, 2012.
[120] O. N. Pakhomova, B. Gregory, I. Semenov, and A. G. Pakhomov. Calcium-mediated pore expan-

sion and cell death following nanoelectroporation. Biochimica et Biophysica Acta - Biomembranes, 1838(10):2547–2554, 2014.

[121] P. T. Vernier, Yinghua Sun, Laura Marcu, Cheryl M. Craft, and Martin A. Gundersen. Nanoelectropulse-Induced Phosphatidylserine Translocation. Biophysical Journal, 86(6):4040–4048, 2004.

[122] I. Goswami, S. Coutermarsh-Ott, R. G. Morrison, I. C. Allen, R. V. Davalos, S. S. Verbridge, and L. R. Bickford. Irreversible electroporation inhibits pro-cancer inflammatory signaling in triple negative breast cancer cells. Bioelectrochemistry, 113:42–50, 2017.

[123] E. Tekle, M. D. Wolfe, H. Oubrahim, and P. B. Chock. Phagocytic clearance of electric field induced 'apoptosis-mimetic' cells. Biochemical and Biophysical Research Communications, 376(2):256–260, 2008.

[124] Tadej Kotnik and Damijan Miklavcic. Theoretical evaluation of voltage inducement on internal membranes of biological cells exposed to electric fields. Biophysical journal, 90(2):480–91, jan 2006.

[125] Hui Ye, Marija Cotic, Eunji E Kang, Michael G Fehlings, and Peter L Carlen. Transmembrane potential induced on the internal organelle by a time-varying magnetic field: a model study. Journal of neuroengineering and rehabilitation, 7(12):12, 2010.

[126] Michael B. Sano, Christopher B. Arena, Matthew R. DeWitt, Dieter Saur, and Rafael V. Davalos. In-vitro bipolar nano- and microsecond electro-pulse bursts for irreversible electroporation therapies. Bioelectrochemistry, 100:69–79, 2014.

[127] S. J. Beebe, N. M. Sain, and W. Ren. Induction of cell death mechanisms and apoptosis by nanosecond pulsed electric fields (nsPEFs). Cells, 2(1):136–62, Jan 2013.

[128] Claudia Muratori, Andrei G. Pakhomov, Elena C. Gianulis, Sarah Damsbo Jensen, and Olga N. Pakhomova. The cytotoxic synergy of nanosecond electric pulses and low temperature leads to apoptosis. Scientific Reports, 6(October):36835, 2016.

[129] S. Kakorin, E. Redeker, and E. Neumann. Electroporative deformation of salt filled lipid vesicles. European Biophysics Journal, 27(1):43–53, 1998.

[130] Chilman Bae and Peter J Butler. Finite element analysis of microelectrotension of cell membranes. Biomech Model Mechanobiol, 7(5):379–386, 2008.

[131] Lane C. McConnell, Michael J. Miksis, and Petia M. Vlahovska. Continuum modeling of the electric-field-induced tension in deforming lipid vesicles. The Journal of Chemical Physics, 143(24):243132, 2015.

[132] RV Davalos, Boris Rubinsky, and LM Mir. Theoretical analysis of the thermal effects during in vivo tissue electroporation. Bioelectrochemistry, 61(1-2):99–107, oct 2003.

[133] Miao Yu, Wenchang Tan, and Hao Lin. A stochastic model for DNA translocation through an electropore. Biochimica et biophysica acta, 1818(11):2494–501, 2012.

[134] P Quaglino, C Mortera, S Osella-Abate, M Barberis, M Illengo, M Rissone, P Savoia, and M G Bernengo. Electrochemotherapy with intravenous bleomycin in the local treatment of skin melanoma metastases. Annals of surgical oncology, 15(8):2215–2222, 2008.

[135] Thiruvallur R Gowrishankar, Axel T Esser, Zlatko Vasilkoski, Kyle C Smith, and James C Weaver. Microdosimetry for conventional and supra-electroporation in cells with organelles. Biochemical and biophysical research communications, 341(4):1266–76, mar 2006.

[136] Kyle C. Smith and James C. Weaver. Transmembrane molecular transport during versus after extremely large, nanosecond electric pulses. Biochemical and Biophysical Research Communications, 412(1):8–12, 2011.

[137] Iurii Semenov, Christian Zemlin, Olga N Pakhomova, Shu Xiao, and Andrei G Pakhomov. Diffuse, non-polar electropermeabilization and reduced propidium uptake distinguish the effect of nanosecond electric pulses. Biochimica et Biophysica Acta (BBA)-Biomembranes, 1848(10):2118–2125, 2015.

[138] Andrei G. Pakhomov, Iurii Semenov, Shu Xiao, Olga N. Pakhomova, Betsy Gregory, Karl H. Schoen-

bach, Jody C. Ullery, Hope T. Beier, Sambasiva R. Rajulapati, and Bennett L. Ibey. Cancellation of cellular responses to nanoelectroporation by reversing the stimulus polarity. Cellular and Molecular Life Sciences, 71(22):4431–4441, 2014.

[139] Michael B. Sano, Richard E. Fan, and Lei Xing. Asymmetric Waveforms Decrease Lethal Thresholds in High Frequency Irreversible Electroporation Therapies. Scientific Reports, 7(January):40747, 2017.

[140] Suyashree P Bhonsle, Christopher B Arena, Daniel C Sweeney, and Rafael V Davalos. Mitigation of impedance changes due to electroporation therapy using bursts of high-frequency bipolar pulses. BioMedical Engineering OnLine, 14(Suppl 3):S3, 2015.

[141] Christopher B Arena, Michael B Sano, Marissa Nichole Rylander, and Rafael V Davalos. Theoretical considerations of tissue electroporation with high-frequency bipolar pulses. IEEE transactions on bio-medical engineering, 58(5):1474–82, may 2011.

[142] Eduardo L Latouche, Michael B Sano, Melvin F Lorenzo, Rafael V Davalos, and Robert CG Martin. Irreversible electroporation for the ablation of pancreatic malignancies: A patient-specific methodology. Journal of surgical oncology, 115(6):711–717, 2017.

[143] G Ya Wiederschain. The molecular probes handbook. a guide to fluorescent probes and labeling technologies. Biochemistry (Moscow), 76(11):1276–1276, 2011.

[144] Jianbo Li and Hao Lin. Numerical simulation of molecular uptake via electroporation. Bioelectrochemistry, 82(1):10–21, 2011.

[145] Iurii Semenov, Shu Xiao, and Andrei G Pakhomov. Primary pathways of intracellular Ca(2+) mobilization by nanosecond pulsed electric field. Biochimica et biophysica acta, 1828(3):981–9, 2013.

[146] S M Kennedy, Z Ji, J C Hedstrom, J H Booske, and S C Hagness. Quantification of electroporative uptake kinetics and electric field heterogeneity effects in cells. Biophysical Journal, 94(12):5018–5027, 2008.

[147] Stephen M. Kennedy, Erik J. Aiken, Kaytlyn A. Beres, Adam R. Hahn, Samantha J. Kamin, Susan C. Hagness, John H. Booske, and William L. Murphy. Cationic peptide exposure enhances pulsed-electric-field-mediated membrane disruption. PLoS ONE, 9(3), 2014.

[148] P. T. Vernier, M. J. Ziegler, Y. Sun, W. V. Chang, M. A. Gundersen, and D. P. Tieleman. Nanopore formation and phosphatidylserine externalization in a phospholipid bilayer at high transmembrane potential. Journal of the American Chemical Society, 128(19):6288–6289, 2006.

[149] Janja Dermol, Olga N. Pakhomova, Andrei G. Pakhomov, and Damijan Miklavčič. Cell Electrosensitization Exists Only in Certain Electroporation Buffers. Plos One, 11(7):e0159434, 2016.

[150] Caleb C Roth, Ronald A Barnes Jr, Bennett L Ibey, Hope T Beier, L Christopher Mimun, Saher M Maswadi, Mehdi Shadaram, and Randolph D Glickman. Characterization of pressure transients generated by nanosecond electrical pulse (nsep) exposure. Scientific reports, 5:1–15, 2015.

[151] Zachary A. Steelman, Gleb P. Tolstykh, Hope T. Beier, and Bennett L. Ibey. Cellular response to high pulse repetition rate nanosecond pulses varies with fluorescent marker identity. Biochemical and Biophysical Research Communications, pages 1–7, 2016.

[152] S Kakorin and E Neumann. Ionic conductivity of electroporated lipid bilayer membranes. Bioelectrochemistry., 56(1567-5394 JC - DN2):163–166, 2002.

[153] Damijan Miklavcic and Leila Towhidi. Numerical study of the electroporation pulse shape effect on molecular uptake of biological cells. Radiology and oncology, 44(1):34–41, mar 2010.

[154] Christian A. Combs. Fluorescence Microscopy: A Concise Guide to Current Imaging Methods. Curr Protoc Neurosci, 0(2):1–19, 2010.

[155] Klaus Suhling, M W French, and David Phillips. Time-resolved fluorescence microscopy. Photochem. Photobiol. Sci., 2005:13–22, 2005.

[156] G. Pucihar, T. Kotnik, D. Miklavčič, and J. Teissié. Kinetics of transmembrane transport of small molecules into electropermeabilized cells. Biophysical Journal, 95(6):2837–48, 2008.

[157] Nathan C Shaner, Paul A Steinbach, and Riger Y Tsien. A guide to choosing fluorescent proteins. Nature Methods, 2(12):905–909, 2005.
[158] J. C. Maxwell. A Dynamical Theory of the Electromagnetic Field. Philosophical Transactions of the Royal Society of London, 155(0):459–512, 1865.
[159] Herbert P Neff. Introductory Electromagnetics. John Wiley & Sons, Inc., 1991.
[160] J J L Higdon and G P Muldowney. Resistance functions for spherical particles , droplets and bubbles in cylindrical tubes. Journal of Fluid Mechanics, 298:193–210, 1995.
[161] Samo Mahnič-Kalamiza, Damijan Miklavčič, and Eugène Vorobiev. Dual-porosity model of solute diffusion in biological tissue modified by electroporation. Biochimica et Biophysica Acta - Biomembranes, 1838(7):1950–1966, 2014.
[162] D Kashchiev and D Exerowa. Bilayer lipid membrane permeation and rupture due to hole formation. Biochimica et biophysica acta, 732(1):133–145, 1983.
[163] S. Marcelja and N. Radic. Repulsion of interfaces due to boundary water. Chemical Physics Letters, 42(1):129–130, 1976.
[164] S. Marcelja. Structural Contribution to Solute-Solute Interaction. Croatica Chemica Acta, 49(2):347–358, 1977.
[165] V. F. Pastushenko, Yu. A. Chizjladzhev, and V. B. Arakelyan. 249 - Electric Breakdown of Bilayer Lipid Membranes IV. Consideration of the Kinetic Stage in the Case of the Single-Defect Membrane. Bioelectrochemistry and Bioenergetics, 104(6):71–79, 1979.
[166] Jacob N Israelachvili and Haakan Wennerstroem. Entropic forces between amphiphilic surfaces in liquids. The Journal of Physical Chemistry, 96(2):520–531, 1992.
[167] Tadej Kotnik, Feda Bobanovic, and Damijan Miklavcic. Applied electric fields-a theoretical analysis. Bioelectrochemistry and Bioenergetics, 43:285–291, 1997.
[168] John Neu and Wanda Krassowska. Asymptotic model of electroporation. Physical Review E, 59(3):3471–3482, 1999.
[169] Kevin T Powell and James C Weaver. Transient Aqueous Pores in Bilayer Membranes: A Statistical Theory. Bioelectrochemistry and Bioenergetics, 211:211–227, 1986.
[170] Jaka Čemažar, Temple A. Douglas, Eva M. Schmelz, and Rafael V. Davalos. Enhanced contactless dielectrophoresis enrichment and isolation platform via cell-scale microstructures. Biomicrofluidics, 10(1):014109, 2016.
[171] K A DeBruin and W Krassowska. Modeling electroporation in a single cell. II. Effects Of ionic concentrations. Biophysical journal, 77(3):1225–1233, 1999.
[172] R. Buchner, J. Barthel, and J. Stauber. The dielectric relaxation of water between 0C and 35C. Chemical Physics Letters, 306(1-2):57–63, 1999.
[173] Richard Buchner, Glenn T. Hefter, and Peter M. May. Dielectric Relaxation of Aqueous NaCl Solutions. The Journal of Physical Chemistry A, 103(1):1–9, 1999.
[174] Q Hu, RP Joshi, and A Beskok. Model study of electroporation effects on the dielectrophoretic response of spheroidal cells. Journal of Applied Physics, 106(2):024701, 2009.
[175] P R C Gascoyne, R Pethig, J P H Burt, and F F Becker. Membrane changes accompanying the induced differentiation of Friend murine erythroleukemia cells studies by dielectrophoresis. Biochimica et Biophysica Acta - Biomembranes, 1149(1):119–126, 1993.
[176] Ralph Hölzel and Ingolf Lamprecht. Dielectric properties of yeast cells as determined by electrorotation. Biochimica et Biophysica Acta (BBA) - Biomembranes, 1104(1):195–200, 1992.
[177] B A Afzelius. The ultrastructure of the nuclear membrane of the sea urchin oocyte as studied with the electron microscope. Experimental cell research, 8(1):147–158, 1955.
[178] K. Asami, Y. Takahashi, and S. Takashima. Dielectric properties of mouse lymphocytes and erythrocytes. BBA - Molecular Cell Research, 1010(1):49–55, 1989.
[179] Scott A. Freeman, Michele A. Wang, and James C. Weaver. Theory of electroporation of planar

bilayer membranes: predictions of the aqueous area, change in capacitance, and pore-pore separation. Biophysical journal, 67(1):42–56, 1994.

[180] James C. Weaver and Robert A. Mintzer. Decreased bilayer stability due to transmembrane potentials. Physics Letters A, 86(1):57–59, 1981.

[181] Thiruvallur R Gowrishankar and James C Weaver. An approach to electrical modeling of single and multiple cells. Proceedings of the National Academy of Sciences of the United States of America, 100:3203–3208, 2003.

[182] L. Towhidi, D. Khodadadi, N. Maimari, R. M. Pedrigi, H. Ip, Z. Kis, B. R. Kwak, T. W. Petrova, M. Delorenzi, and R. Krams. Comparison between direct and reverse electroporation of cells insitu: a simulation study. Physiological Reports, 4(6):e12673, 2016.

[183] M. Leguèbe, A. Silve, L. M. Mir, and C. Poignard. Conducting and permeable states of cell membrane submitted to high voltage pulses: mathematical and numerical studies validated by the experiments. Journal of Theoretical Biology, 360:83–94, 2014.

[184] M. Leguèbe, C. Poignard, and L. Weynans. A second-order cartesian method for the simulation of electropermeabilization cell models. Journal of Computational Physics, 292:114–140, 2015.

[185] Michael Leguèbe, Maria G Notarangelo, Monika Twarogowska, Roberto Natalini, and Clair Poignard. Mathematical model for transport of dna plasmids from the external medium up to the nucleus by electroporation. Mathematical biosciences, 285:1–13, 2017.

[186] Mojca Pavlin and Maša Kandušer. New insights into the mechanisms of gene electrotransfer–experimental and theoretical analysis. Scientific Reports, 5:9132, 2015.

[187] Bostjan Markelc, Eva Skvarca, Tanja Dolinsek, Veronika Prevodnik Kloboves, Andrej Coer, Gregor Sersa, and Maja Cemazar. Inhibitor of endocytosis impairs gene electrotransfer to mouse muscle in vivo. Bioelectrochemistry, 103:111–119, 2015.

[188] Stephane Orlowski, Jean Belehradey Jr, Claude Paoletti, and Lluis M. Mir. Transient Electropermeabilization. Biochemical pharmacology, 37(24):4727–4733, 1988.

[189] Gregor Sersa, Justin Teissie, Maja Cemazar, Emanuela Signori, Urska Kamensek, Guillermo Marshall, and Damijan Miklavcic. Electrochemotherapy of tumors as in situ vaccination boosted by immunogene electrotransfer. Cancer Immunology, Immunotherapy, 64(10):1315–1327, 2015.

[190] Matthew J. Ziegler and P. Thomas Vernier. Interface water dynamics and porating electric fields for phospholipid bilayers. Journal of Physical Chemistry B, 112(43):13588–13596, 2008.

[191] P. Thomas Vernier, Zachary A. Levine, and Martin A. Gundersen. Water bridges in electropermeabilized phospholipid bilayers. Proceedings of the IEEE, 101(2):494–504, 2013.

[192] T. John Lewis. A Model for Bilayer Membrane Electroporation Based on Resultant Electromechanical Stress. IEEE Transactions on Dielectrics and Electrical Insulation, 10(5):769–777, 2003.

[193] James C. Weaver and Yu.A. Chizmadzhev. Theory of electroporation: A review. Bioelectrochemistry and Bioenergetics, 41(2):135–160, dec 1996.

[194] J. Teissie, M. Golzio, and M.P. Rols. Mechanisms of cell membrane electropermeabilization: A minireview of our present (lack of ?) knowledge. Biochimica et Biophysica Acta (BBA) - General Subjects, 1724(3):270–280, 2005.

[195] Michael B. Sano, Christopher B. Arena, Katelyn R. Bittleman, Matthew R. DeWitt, Hyung J. Cho, Christopher S. Szot, Dieter Saur, James M. Cissell, John Robertson, Yong W. Lee, and Rafael V. Davalos. Bursts of Bipolar Microsecond Pulses Inhibit Tumor Growth. Scientific Reports, 5:14999, 2015.

[196] Robert E Neal, Ravi Singh, Heather C Hatcher, Nancy D Kock, Suzy V Torti, and Rafael V Davalos. Treatment of breast cancer through the application of irreversible electroporation using a novel minimally invasive single needle electrode. Breast cancer research and treatment, 123(1):295–301, aug 2010.

[197] B. Mali, T. Jarm, M. Snoj, G. Sersa, and D. Miklavcic. Antitumor effectiveness of electrochemother-

apy: A systematic review and meta-analysis. European Journal of Surgical Oncology, 39(1):4–16, 2013.

[198] Damijan Miklavčič, Barbara Mali, Bor Kos, Richard Heller, and Gregor Serša. Electrochemotherapy: from the drawing board into medical practice. Biomedical engineering online, 13(1):29, 2014.

[199] G. Serša, B. Štabuc, M. Čemažar, B. Jančar, D. Miklavčič, and Z. Rudolf. Electrochemotherapy with cisplatin: Potentiation of local cisplatin antitumour effectiveness by application of electric pulses in cancer patients. European Journal of Cancer, 34(8):1213–1218, 1998.

[200] L. Frank Glass, Neil A. Fenske, M. Jaroszeski, R. Perrott, David T. Harvey, Douglas S. Reintgen, and Richard Heller. Bleomycin-mediated electrochemotherapy of basal cell carcinoma. Journal of the American Academy of Dermatology, 34(1):82–86, 1996.

[201] Richard Heller, Mark J. Jaroszeski, L. Frank Glass, Jane L. Messina, David P. Rapaport, Ronald C. Deconti, Neil A. Fenske, Richard A. Gilbert, Lluis M. Mir, and Douglas S. Reintgen. Phase I/II trial for the treatment of cutaneous and subcutaneous tumors using electrochemotherapy. Cancer, 77(5):964–971, 1996.

[202] Richard Heller, Richard Gilbert, and Mark J. Jaroszeski. Clinical applications of electrochemotherapy. Advanced Drug Delivery Reviews, 35(1):119–129, 1999.

[203] Tina Stepišnik, Tomaž Jarm, Aleš Grošelj, Ibrahim Edhemović, Mihajlo okić, Arpad Ivanecz, Blaž Trotovšek, Erik Brecelj, Stojan Potrč, Maja Čemažar, Nebojša Glumac, Tjaša Pečnik, Biserka Verberič, Eldar Gadžijev, and Primož Strojan. Electrochemotherapy: an effective method for the treatment of tumors with a combination of chemotherapeutic agent and electric field. Zdravniški Vestnik, 85(1):41–55, 2016.

[204] Tai-Kin Wong and Eberhard Neumann. Electric field mediated gene transfer. Biochemical and Biophysical Research Communications, 107(2):584–587, 1982.

[205] L M Mir, M F Bureau, J Gehl, R Rangara, D Rouy, J M Caillaud, P Delaere, D Branellec, B Schwartz, and D Scherman. High-efficiency gene transfer into skeletal muscle mediated by electric pulses. Proceedings of the National Academy of Sciences of the United States of America, 96(8):4262–4267, 1999.

[206] F M André, J Gehl, G Sersa, V Préat, P Hojman, J Eriksen, M Golzio, M Cemazar, N Pavselj, M-P Rols, D Miklavcic, E Neumann, J Teissié, and L M Mir. Efficiency of high- and low-voltage pulse combinations for gene electrotransfer in muscle, liver, tumor, and skin. Human gene therapy, 19(11):1261–1271, 2008.

[207] A. C. Durieux, Régis Bonnefoy, Thierry Busso, and Damien Freyssenet. In vivo gene electrotransfer into skeletal muscle: Effects of plasmid DNA on the occurrence and extent of muscle damage. Journal of Gene Medicine, 6(7):809–816, 2004.

[208] Thomas L Ellis, Paulo A Garcia, John H Rossmeisl, Natalia Henao-Guerrero, John Robertson, and Rafael V Davalos. Nonthermal irreversible electroporation for intracranial surgical applications. Laboratory investigation. Journal of neurosurgery, 114(3):681–8, mar 2011.

[209] Hester J Scheffer, Marleen C a M Melenhorst, Aukje a J M van Tilborg, Karin Nielsen, Karin M van Nieuwkerk, Richard a de Vries, Petrousjka M P van den Tol, and Martijn R Meijerink. Percutaneous Irreversible Electroporation of a Large Centrally Located Hepatocellular Adenoma in a Woman with a Pregnancy Wish. Cardiovascular and interventional radiology, dec 2014.

[210] Kevin P. Charpentier, Farrah Wolf, Lelia Noble, Brody Winn, Murray Resnick, and Damian E. Dupuy. Irreversible electroporation of the liver and liver hilum in swine. Hpb, 13:168–173, 2011.

[211] W Cheung, H Kavnoudias, S Roberts, B Szkandera, W Kemp, and K R Thomson. Irreversible electroporation for unresectable hepatocellular carcinoma: initial experience and review of safety and outcomes. Technology in cancer research & treatment, 12(3):233–41, jun 2013.

[212] Eliel Ben-David, Liat Appelbaum, Jacob Sosna, Isaac Nissenbaum, and S. Nahum Goldberg. Characterization of irreversible electroporation ablation in in vivo porcine liver. American Journal of

Roentgenology, 198(1), 2012.

[213] David Kwon, Kelli McFarland, Vic Velanovich, and RCG Martin. Borderline and locally advanced pancreatic adenocarcinoma margin accentuation with intraoperative irreversible electroporation. Surgery, 156(4):910–22, oct 2014.

[214] Robert C. G. Martin, David Kwon, Sricharan Chalikonda, Marty Sellers, Eric Kotz, Charles Scoggins, Kelly M. McMasters, and Kevin Watkins. Treatment of 200 Locally Advanced (Stage III) Pancreatic Adenocarcinoma Patients With Irreversible Electroporation. Annals of Surgery, 262(3):486–494, 2015.

[215] Christopher B Arena, Michael B Sano, John H Rossmeisl, John L Caldwell, Paulo A Garcia, Marissa Nichole Rylander, and Rafael V Davalos. High-frequency irreversible electroporation (H-FIRE) for non-thermal ablation without muscle contraction. BME Online, 10(1):102, 2011.

[216] Bor Kos, Peter Voigt, Damijan Miklavcic, and Michael Moche. Careful treatment planning enables safe ablation of liver tumors adjacent to major blood vessels by percutaneous irreversible electroporation (IRE). Radiology and Oncology, 49(3):234–241, 2015.

[217] G. Pucihar, L. M. Mir, and D. Miklavčič. The effect of pulse repetition frequency on the uptake into electropermeabilized cells in vitro with possible applications in electrochemotherapy. Bioelectrochemistry, 57:167–172, 2002.

[218] Damijan Miklavčič, Gorazd Pucihar, Miran Pavlovec, Samo Ribarič, Marko Mali, Alenka Maček-Lebar, Marko Petkovšek, Janez Nastran, Simona Kranjc, Maja Čemažar, and Gregor Serša. The effect of high frequency electric pulses on muscle contractions and antitumor efficiency in vivo for a potential use in clinical electrochemotherapy. Bioelectrochemistry, 65(2):121–128, 2005.

[219] A Zupanic, S Ribaric, and D Miklavcic. Increasing the repetition frequency of electric pulse delivery reduces unpleasant sensations that occur in electrochemotherapy. Neoplasma, 54(3):246–50, jan 2007.

[220] Marija Marcan, Denis Pavliha, Bor Kos, Tadeja Forjanic, and Damijan Miklavcic. Web-based tool for visualization of electric field distribution in deep-seated body structures and for planning electroporation-based treatments. Biomedical engineering online, 14(Suppl 3):S4, 2015.

[221] Humberto Vega-Mercado, Olga Martín-Belloso, Bai-Lin Qin, Fu Jung Chang, M. Marcela Góngora-Nieto, Gustavo V. Barbosa-Cánovas, and Barry G. Swanson. Non-thermal food preservation: Pulsed electric fields. Trends in Food Science & Technology, 8(5):151–157, 1997.

[222] Seacheol Min, Gulsun Akdemir Evrendilek, and Howard Q. Zhang. Pulsed electric fields: Processing system, microbial and enzyme inhibition, and shelf life extension of foods. IEEE Transactions on Plasma Science, 35(1):59–73, 2007.

[223] Suyashree P Bhonsle, Christopher B Arena, and Rafael V Davalos. A Feasibility Study to Mitigate Tissue-Tumor Heterogeneity Using High Frequency Bipolar Electroporation Pulses. IFMBE Proceedings, 37:1140–1143, 2012.

[224] A. Maček-Lebar, N. A. Kopitar, K. Ihan, G. Sersa, and D. Miklavčič. Significance of treatment energy in cell electropermeabilization. Electro- and Magnetobiology, 17(2):255–262, 1998.

[225] Matej Rebersek, Matej Kranjc, Denis Pavliha, Tina Batista-Napotnik, Danilo Vrtacnik, Slavko Amon, Damijan Miklavcic, Matej Reberek, Matej Kranjc, Denis Pavliha, Tina Batista-Napotnik, Danilo Vrtanik, Slavko Amon, and Damijan Miklavi. Blumlein configuration for high-repetition-rate pulse generation of variable duration and polarity using synchronized switch control. IEEE transactions on bio-medical engineering, 56(11):2642–8, nov 2009.

[226] M Hibino, H Itoh, and K Kinosita. Time courses of cell electroporation as revealed by submicrosecond imaging of transmembrane potential. Biophysical journal, 64(6):1789–1800, 1993.

[227] T. Kotnik, G. Pucihar, M. Reberšek, D. Miklavčič, and L. M. Mir. Role of pulse shape in cell membrane electropermeabilization. Biochimica et Biophysica Acta - Biomembranes, 1614(2):193–200, 2003.

[228] Elena C Gianulis, Jimo Lee, Chunqi Jiang, Shu Xiao, Bennet L Ibey, and Andrei G Pakhomov. Electroporation of mammalian cells by nanosecond electric field oscillations and its inhibition by the electric field reversal. Scientific reports, 5(August):13818, 2015.

[229] Karl H. Schoenbach, Andrei G. Pakhomov, Iurii Semenov, Shu Xiao, Olga N. Pakhomova, and Bennett L. Ibey. Ion transport into cells exposed to monopolar and bipolar nanosecond pulses. Bioelectrochemistry, 103:44–51, 2014.

[230] J. Patrick Reilly, Vanda T. Freeman, and Willard D. Larkin. Sensory Effects of Transient Electrical StimulationEvaluation with a Neuroelectric Model. IEEE Transactions on Biomedical Engineering, BME-32(12):1001–1011, 1985.

[231] James R. Lepock. Cellular effects of hyperthermia: relevance to the minimum dose for thermal damage. International Journal of Hyperthermia, 19(3):252–266, 2003.

[232] A. Maček-Lebar and D. Miklavčič. Cell electropermeabilization to small molecules in vitro: control by pulse parameters. Radiology and Oncology, 35(3), 2001.

[233] C. Geuzaine and J. F. Remacle. Gmsh: A 3-d finite element mesh generator with built-in pre-and post-processing facilities. International Journal for Numerical Methods in Engineering, 79(11):1309–1331, 2009.

[234] M. Alnæs, J. Blechta, J. Hake, A. Johansson, B. Kehlet, A. Logg, C. Richardson, J. Ring, M. E. Rognes, and G. N. Wells. The fenics project version 1.5. Archive of Numerical Software, 3(100):9–23, 2015.

[235] M. Bonakdar, E. Latouche, R. Mahajan, and R. V. Davalos. The feasibility of a smart surgical probe for verification of IRE treatments using electrical impedance spectroscopy. IEEE Transactions on Biomedical Engineering, 9294(c):1–1, 2015.

[236] A. Fedorov, R. Beichel, J. Kalpathy-Cramer, J. Finet, J. C. Fillion-Robin, S. Pujol, C. Bauer, D. Jennings, F. Fennessy, M. Sonka, J. Buatti, S. Aylward, J. V. Miller, S. Pieper, and R. Kikinis. 3d slicer as an image computing platform for the quantitative imaging network. Magnetic Resonance Imaging, 30(9):1323–1341, 2012.

[237] P. Cignoni, M. Callieri, M. Corsini, M. Dellepiane, F. Ganovelli, and G. Ranzuglia. Meshlab: an open-source mesh processing tool. In Eurographics Italian Chapter Conference, volume 2008, pages 129–136, 2008.

[238] J. Schindelin, I. Arganda-Carreras, E. Frise, V. Kaynig, M. Longair, T. Pietzsch, S. Preibisch, C. Rueden, S. Saalfeld, B. Schmid, J. Y. Tinevez, D. J. White, V. Hartenstein, K. Eliceiri, P. Tomancak, and A. Cardona. Fiji: an open-source platform for biological-image analysis. Nature Methods, 9(7):676–682, 2012.

[239] A. E. Carpenter, T. R. Jones, M. R. Lamprecht, C. Clarke, I. H. Kang, O. Friman, D. A. Guertin, J. H. Chang, R. A. Lindquist, J. Moffat, P. Golland, and D. M. Sabatini. Cellprofiler: image analysis software for identifying and quantifying cell phenotypes. Genome biology, 7(10):R100, 2006.

[240] O. Seksek, J. Biwersi, and A. S. Verkman. Translational diffusion of macromolecule-sized solutes in cytoplasm and nucleus. Journal of Cell Biology, 138(1):131–142, 1997.

[241] E Neumann, K Toensing, S Kakorin, P Budde, and J Frey. Mechanism of electroporative dye uptake by mouse B cells. Biophysical journal, 74(1):98–108, 1998.

[242] G. L. Lukacs, P. Haggie, O. Seksek, D. Lechardeur, N. Freedman, and A. S. Verkman. Size-dependent DNA mobility in cytoplasm and nucleus. Journal of Biological Chemistry, 275(3):1625–1629, 2000.

[243] J. Deng, K. H. Schoenbach, E. S. Buescher, P. S. Hair, P. M. Fox, and S. J. Beebe. The effects of intense submicrosecond electrical pulses on cells. Biophysical journal, 84(4):2709–2714, 2003.

[244] A. S. Verkman. Membrane biology water permeability measurement in living cells and complex tissues. Journal of Membrane Biology, 173:73–87, 2000.

[245] V. Zarnitsyn, C. A. Rostad, and M. R. Prausnitz. Modeling transmembrane transport through cell membrane wounds created by acoustic cavitation. Biophysical Journal, 95(9):4124–4138, 2008.

[246] H. P. Kao and J. R. Abney. Determinants of the Translational Mobility of a Small Solute in Cell Cytoplasm. Journal of Cell Biology, 120(1):175–184, 1993.

[247] S. Bicknese, N. Periasamy, S. B. Shohet, and A. S. Verkman. Cytoplasmic viscosity near the cell plasma membrane: measurement by evanescent field frequency-domain microfluorimetry. Biophysical Journal, 65(3):1272–1282, 1993.

[248] G. Pucihar, J. Krmelj, M. Reberšek, T. B. Napotnik, and D. Miklavčič. Equivalent pulse parameters for electroporation. IEEE Transactions on Biomedical Engineering, 58(11):3279–3288, 2011.

[249] Aude Silve, Isabelle Leray, Clair Poignard, and Lluis M Mir. Impact of external medium conductivity on cell membrane electropermeabilization by microsecond and nanosecond electric pulses. Scientific Reports, 6(November 2015):19957, 2016.

[250] S. K. Frandsen, H. Gissel, P. Hojman, J. Eriksen, and J. Gehl. Calcium electroporation in three cell lines: a comparison of bleomycin and calcium, calcium compounds, and pulsing conditions. Biochimica et biophysica acta, 1840(3):1204–8, Mar 2014.

[251] A. D. Whetton and T. M. Dexter. Effect of haematopoietic cell growth factor on intracellular ATP levels. Nature, 303(5918):629–631, 1983.

[252] S. K. Calderwood, E. A. Bump, M. A. Stevenson, and G. M. Van Kersen, I .and Hahn. Investigation of adenylate energy charge, phosphorylation potential, and ATP concentration in cells stressed with starvation and heat. Journal of Cellular Physiology, 124(2):261–268, 1985.

[253] E. J. Fine, A. Miller, E. V. Quadros, J. M. Sequeira, and R. D. Feinman. Acetoacetate reduces growth and ATP concentration in cancer cell lines which over-express uncoupling protein 2. Cancer Cell International, 9:14, 2009.

[254] M. J. Poellmann and R. C. Lee. Repair and regeneration of the wounded cell membrane. Regenerative Engineering and Translational Medicine, 641(Mc 6035), 2017.

[255] R. C. Lee, D. Zhang, and J. Hannig. Biophysical injury mechanisms in electrical shock trauma. Annu. Rev. Biomed, 02:477–509, 2000.

[256] W. M. Arnold and U. Zimmermann. Dielectric properties of zwitterion solutions. Biochemical Society transactions, 21(4):475S, 1993.

[257] Z. Gagnon and H. C. Chang. Aligning fast alternating current electroosmotic flow fields and characteristic frequencies with dielectrophoretic traps to achieve rapid bacteria detection. Electrophoresis, 26(19):3725–3737, 2005.

[258] C. G. Malmberg and A. A. Maryott. Dielectric constants of aqueous solutions of dextrose and sucrose. Journal of Research of the National Bureau of Standards, 45(4):299, 1950.

[259] J. C. Weaver, R. S. Son, T. R. Gowrishankar, D. C. Sweeney, and R. V. Davalos. Methods for inducing electroporation and tissue ablation, June 10 2016. US Patent App. 15/179,310.

[260] S. Satkauskas, M. F. Bureau, M. Puc, A. Mahfoudi, D. Scherman, D. Miklavčič, and L. M. Mir. Mechanisms of in vivo DNA electrotransfer: respective contributions of cell electropermeabilization and DNA electrophoresis. Molecular Therapy, 5(2):133–140, 2002.

[261] G. Saulis, M. S. Venslauskas, and J. Naktinis. Kinetics of pore resealing in cell membranes after electroporation. Journal of Electroanalytical Chemistry, 321(1):1–13, 1991.

[262] Jeffrey L Moran, Naga Neehar Dingari, Paulo A Garcia, and Cullen R Buie. Bioelectrochemistry Numerical study of the effect of soft layer properties on bacterial electroporation. Bioelectrochemistry, 2017.

[263] G Saulis. Pore disappearance in a cell after electroporation: theoretical simulation and comparison with experiments. Biophysical journal, 73(3):1299–1309, 1997.

[264] RP Joshi, Qin Hu, and KH Schoenbach. Modeling studies of cell response to ultrashort, high-intensity electric fields-implications for intracellular manipulation. Plasma Science, IEEE ..., 32(4):1677–1686, 2004.

[265] Erick K. Moen, Bennett L. Ibey, Hope T. Beier, and Andrea M. Armani. Quantifying pulsed elec-

tric field-induced membrane nanoporation in single cells. Biochimica et Biophysica Acta (BBA) - Biomembranes, 1858(11):2795–2803, 2016.
[266] Witold K Subczynski and Larry E Hopwood. Is the Mammalian Cell Plasma Membrane a Barrier to Oxygen Transport ? Journal of General Physiology, 100(July):69–87, 1992.
[267] Panadda Dechadilok and William M Deen. Hindrance Factors for Diffusion and Convection in Pores. Ind. Eng. Chem. Res, 45:6953–6959, 2006.
[268] LR Petzold and AC Hindmarsh. Lsoda. Computing and Mathematics Research Division, I-316 Lawrence Livermore National Laboratory, Livermore, CA, 94550, 1997.
[269] E. Jones, T. Oliphant, P. Peterson, et al. SciPy: Open source scientific tools for Python, 2001–.
[270] Aviad Hai and Micha E Spira. On-chip electroporation , membrane repair dynamics and transient in-cell recordings by arrays of gold mushroom-shaped microelectrodes. Lab on a Chip, 12:2865–2873, 2012.
[271] L V Chernomordik, S I Sukharev, S V Popov, V F Pastushenko, a V Sokirko, I G Abidor, and Y a Chizmadzhev. The electrical breakdown of cell and lipid membranes: the similarity of phenomenologies. Biochimica et biophysica acta, 902:360–373, 1987.
[272] Bianca Flickinger, Thomas Berghöfer, Petra Hohenberger, Christian Eing, and Wolfgang Frey. Transmembrane potential measurements on plant cells using the voltage-sensitive dye ANNINE-6. Protoplasma, 247(1-2):3–12, nov 2010.
[273] Jody A. White, Uwe Pliquett, Peter F. Blackmore, Ravindra P. Joshi, Karl H. Schoenbach, and Juergen F. Kolb. Plasma membrane charging of Jurkat cells by nanosecond pulsed electric fields. European Biophysics Journal, 40(8):947–957, 2011.
[274] S Paula, a G Volkov, a N Van Hoek, T H Haines, and D W Deamer. Permeation of protons, potassium ions, and small polar molecules through phospholipid bilayers as a function of membrane thickness. Biophysical journal, 70(1):339–348, 1996.
[275] Volkmar Heinrich, Ken Ritchie, Narla Mohandas, and Evan Evans. Elastic Thickness Compressibilty of the Red Cell Membrane. Biophysical Journal, 81(3):1452–1463, 2001.
[276] Rafael V. Davalos, Suyashree Bhonsle, and Robert E. Neal. Implications and considerations of thermal effects when applying irreversible electroporation tissue ablation therapy. The Prostate, 1118(January):n/a–n/a, 2015.
[277] A. Silve, A. Guimerà Brunet, B. Al-Sakere, A. Ivorra, and L. M. Mir. Comparison of the effects of the repetition rate between microsecond and nanosecond pulses: Electropermeabilization-induced electro-desensitization? Biochimica et Biophysica Acta - General Subjects, 1840(7):2139–2151, 2014.
[278] Vitalij Novickij, Paulius Ruzgys, Audrius Grainys, and Š Saulius. Bioelectrochemistry High frequency electroporation efficiency is under control of membrane capacitive charging and voltage potential relaxation. Bioelectrochemistry, 119:92–97, 2018.
[279] Jody C. Cantu, Melissa Tarango, Hope T. Beier, and Bennett L. Ibey. The Biological Response Of Cells To Nanosecond Pulsed Electric Fields Is Dependent On Plasma Membrane Cholesterol. Biochimica et Biophysica Acta (BBA) - Biomembranes, 1858(11):2636–2646, 2016.
[280] Elisa M Wasson, Jill W Ivey, S Verbridge, and Rafael V Davalos. The Feasibility of Enhancing Susceptibility of Glioblastoma Cells to IRE Using a Calcium Adjuvant. Annals of Biomedical Engineering, 2017.
[281] D. C. Bartoletti, G. I. Harrison, and J. C. Weaver. The number of molecules taken up by electroporated cells: Quantitative determination. FEBS Letters, 256(1-2):4–10, 1989.
[282] Gorazd Pucihar. Kinetics of Transmembrane Transport of Small Molecules into Electromermeabilized Cells. Biophysical Journal, 0.3(February):165, 2010.
[283] T. Y. Tsong. On electroporation of cell membranes and some related phenomena. Biochemistry and Bioenergetics, 299:271–295, 1990.

[284] Damien Voyer, Aude Silve, Lluis M Mir, Riccardo Scorretti, and Clair Poignard. Dynamical Modeling of tissue electroporation. Bioelectrochemistry, 2017.

[285] T Y Tsong. Electroporation of cell membranes. Biophysical journal, 60(2):297–306, 1991.

[286] P R Danesi, E P Horwitz, G F Vandegrift, R Chiarizia, E P Horwitz, G F Vandegrift, and R Chiarizia Mass. Mass Transfer Rate through Liquid Membranes : Interfacial Chemical Reactions and Diffusion as Simultaneous Permeability Controlling Factors. Separation Science and Technology, 16(2):201–2011, 1981.

[287] I.P. Sugar and E. Neumann. Stochastic Model for Electric Field-Induced Membrane Pores. Biophysical Chemistry, 19:211–225, 1984.

[288] Maura Casciola, Marina A Kasimova, Lea Rems, Sara Zullino, Francesca Apollonio, and Mounir Tarek. Properties of lipid electropores I: Molecular dynamics simulations of stabilized pores by constant charge imbalance Properties of lipid electropores I: Molecular dynamics simulations of stabilized pores by constant charge imbalance. Bioelectrochemistry, 2016.

[289] Bennett L Ibey, Shu Xiao, Karl H Schoenbach, Michael R Murphy, and G Andrei. Plasma Membrane Permeabilization by 60- and 600-ns Electric Pulses Is Determined by the Absorbed Dose. Bioelectromagnetics, 30(2):92–99, 2009.

[290] Gregor Serša, Borut Štabuc, Maja Čemažar, Damijan Miklavčič, and Zvonimir Rudolf. Electrochemotherapy with cisplatin: clinical experience in malignant melanoma patients. Clinical Cancer Research, 6(3):863–867, 2000.

[291] Y Tamzali, L Borde, M P Rols, M Golzio, F Lyazrhi, and J Teissie. Successful treatment of equine sarcoids with cisplatin electrochemotherapy : A retrospective study of 48 cases. Equine Veterinary Journal, 44:214–220, 2012.

[292] Yang Guo, Yue Zhang, Rachel Klein, Grace M. Nijm, Alan V. Sahakian, Reed A. Omary, Guang-Yu Yu Yang, and Andrew C. Larson. Irreversible electroporation therapy in the liver: longitudinal efficacy studies in a rat model of hepatocellular carcinoma. Cancer research, 70(4):1555–63, feb 2010.

[293] Gary Onik, Paul Mikus, and Boris Rubinsky. Irreversible electroporation: implications for prostate ablation. Technology in cancer research & treatment, 6(4):295–300, aug 2007.

[294] M. R. Prausnitz, J. D. Corbett, Q. J. A. Gimm, D. E. Golan, R. Langer, and J. C. Weaver. Millisecond measurement of transport during and after an electroporation pulse. Biophysical Journal, 68(May):1864–1870, 1995.

[295] Andrey A. Gurtovenko and Ilpo Vattulainen. Pore formation coupled to ion transport through lipid membranes as induced by transmembrane ionic charge imbalance: Atomistic molecular dynamics study. Journal of the American Chemical Society, 127(50):17570–17571, 2005.

[296] Thiruvallur R. Gowrishankar, Kyle C. Smith, and James C. Weaver. Transport-Based Biophysical System Models of Cells for Quantitatively Describing Responses to Electric Fields. Proceedings of the IEEE, 101(2):505–517, feb 2013.

[297] F. Brezzi, G. Manzini, D. Marini, P. Pietra, and A. Russo. Discontinuous Galerkin Approximations for Elliptic Problems. Numerical Methods for Partial Differential Equations, 16(4):365–378, 2000.

[298] Gregory Guyomarc'h, Chang-Ock Lee, and Kiwan Jeon. A discontinuous Galerkin method for elliptic interface problems with application to electroporation. Communications in Numerical Methods in Engineering, 25:991–1008, 2009.

[299] Andrea Cangiani, Emmanuil H. Georgoulis, and Max Jensen. Discontinuous Galerkin Methods for Mass Transfer through Semi-Permeable Membranes. arxiv preprint arxiv:1209.2316v3, pages 1–23, 2012.

[300] M Burger, B Schlake, and M-T Wolfram. Nonlinear Poisson Nernst Planck equations for ion flux through confined geometries Nonlinear Poisson Nernst Planck equations for ion. Nonlinearity, 25:961, 2012.

[301] Dmitry A Cherepanov, Boris A Feniouk, Wolfgang Junge, and Armen Y Mulkidjanian. Low dielectric permittivity of water at the membrane interface: effect on the energy coupling mechanism in biological membranes. Biophysical journal, 85(2):1307–1316, 2003.

[302] P Marszalek, J J Zielinsky, M Fikus, and T Y Tsong. Determination of electric parameters of cell membranes by a dielectrophoresis method. Biophysical journal, 59(5):982–7, 1991.

[303] Yi Zheng, Ehsan Shojaei-Baghini, Chen Wang, and Yu Sun. Rapid measurement of specific membrane capacitance and cytoplasm conductivity on single cells. Proceedings of the IEEE International Conference on Micro Electro Mechanical Systems (MEMS), 42:1105–1108, 2013.

[304] Temple Anne Douglas, Jaka Cemazar, Nikita Balani, Daniel C. Sweeney, Eva M. Schmelz, and Rafael V. Davalos. A feasibility study for enrichment of highly-aggressive cancer subpopulations by their biophysical properties via dielectrophoresis enhanced with synergistic fluid flow. Electrophoresis, pages 1507–1514, 2017.

[305] Adrian Parsegian. Energy of an ion crossing a low dielectric membrane: solutions to four relevant electrostatic problems. Nature, 221(5183):844–846, 1969.

[306] Ephrem Tekle, R. Dean Astumian, and P. Boon Chock. Electro-Permeabilization of Cell Membranes: Effect of the Resting Membrane Potential. Biochemical and Biophysical Research Communications, 172(1):282–287, 1990.

[307] P. T. Vernier, Z. A. Levine, Y. H. Wu, V. Joubert, M. J. Ziegler, L. M. Mir, and D. P. Tieleman. Electroporating fields target oxidatively damaged areas in the cell membrane. PLoS ONE, 4(11), 2009.

[308] M. Yusupov, J. Van der Paal, E.C. Neyts, and A. Bogaerts. Synergistic effect of electric field and lipid oxidation on the permeability of cell membranes. Biochimica et Biophysica Acta (BBA) - General Subjects, 1861:839–847, 2017.

[309] Kristian B Ølgaard, Anders Logg, and Garth N Wells. Automated Code Generation for Discontinuous Galerkin Methods. SIAM Journal on Scientific Computing, 31(2):849–864, 2008.

[310] von H Pauly and HP Schwan. Über die impedanz einer suspension von kugelförmigen teilchen mit einer schale. Zeitschrift für Naturforschung B, 14(2):125–131, 1959.

[311] B. Gabriel and J. Teissie. Generation of reactive-oxygen species induced by electropermeabilization of Chinese hamster ovary cells and their consequence on cell viability. European Journal of Biochemistry, 223(1):25–33, 1994.

[312] M Maccarrone, M R Bladergroen, N Rosato, and Agro Finazzi. Role of lipid peroxidation in electroporation-induced cell permeability. Biochem Biophys Res Commun, 209(2):417–425, 1995.

[313] Yong Zhou, Christina K. Berry, Patrick A. Storer, and Robert M. Raphael. Peroxidation of polyunsaturated phosphatidyl-choline lipids during electroformation. Biomaterials, 28(6):1298–1306, 2007.

[314] PA Garcia, JH Rossmeisl, Robert E II Neal, TL Ellis, and RV Davalos. A Parametric Study Delineating Irreversible Electroporation from Thermal Damage Based on a Minimally Invasive Intracranial Procedure. Biomedical . . . , 34(April), 2011.

[315] Emmanuil H Georgoulis. Discontinuous galerkin methods for linear problems: An introduction. In Approximation Algorithms for Complex Systems, pages 91–126. Springer, 2011.